Universidade do Minho
Escola de Engenharia

Rui Miguel da Silva Carvalho

Development, Manufacture and Full Experimental Validation of an Exhaust Heat Thermoelectrical Generator with Temperature Control

december 2021

Universidade do Minho
Escola de Engenharia

Rui Miguel da Silva Carvalho

Development, Manufacture and Full Experimental Validation of an Exhaust Heat Thermoelectrical Generator with Temperature Control.

Dissertação de Mestrado
Mestrado Integrado em Engenharia Mecânica

Trabalho efetuado sob a orientação do
Professor Doutor Francisco Carrusca Pimenta Brito

e coorientação do:
Professor Doutor Jorge José Gomes Martins

december 2021

ACKNOWLEDGMENTS

Quero neste pequeno capítulo exprimir os meus agradecimentos a todos aqueles que, de alguma forma, me acompanharam e fizeram parte deste trabalho.

Em primeiro lugar e sempre em primeiro, à minha família, em especial aos meus pais e à minha avó, por me terem proporcionado todas as condições possíveis para que todo este percurso fosse alcançado e por me terem dado a educação e as ferramentas que me tornaram quem sou hoje. Como acredito no valor e importância do legado da família, esta conquista é também vossa.

Em segundo lugar gostava de expressar o meu profundo agradecimento ao Professor Francisco Pimenta Brito, que foi muito mais além do que o significado e a responsabilidade que a palavra Orientador carrega. Obrigado pela transmissão de conhecimento, cultura, valores e pela amizade que levo comigo após um ano de convivência quase diária.

Em terceiro lugar aos meus amigos Carlos e o Joaquim, pelas manhãs e tardes passadas no laboratório de motores, pelas risadas, palhaçadas, pelo stress constante e por todas as peças que quebravam diariamente ou falharam durantes os ensaios experimentais, pelo companheirismo e pela constante motivação, valor e confiança que em mim depositaram ao longo deste ano.

Gostava também de deixar uma palavra de agradecimento a todos aqueles que de algum modo ajudaram a que este trabalho fosse concluído. Em especial ao Engenheiro João Carvalho por todo o acompanhamento atento e conselhos incisivos, ao Professor Doutor Jorge Martins pela constante motivação, ao Engenheiro Filipe Marques pelas horas perdidas em reparações de última hora.

Não fica esquecido o agradecimento à Energest® e à BorgWarner® por serem os nossos parceiros na construção destes protótipos inovadores de permutadores de calor.

Por fim, a todos os meus colegas com quem partilhei os últimos cinco anos da minha vida, em especial à amiga Mariana que esteve sempre ao meu lado nos melhores e nos piores momentos, que me acompanhou até à Europa de leste para um semestre peculiar e com quem viajei por esse mundo fora. Entregaste a tese primeiro que eu já viste? Desejo aos nossos filhos e aos filhos deles terem a sorte de poderem encontrar amizades como a nossa.

STATEMENT OF INTEGRITY

I hereby declare having conducted this academic work with integrity. I confirm that I have not used plagiarism or any form of undue use of information or falsification of results along the process leading to its elaboration.

I further declare that I have fully acknowledged the Code of Ethical Conduct of the University of Minho.

Ao meu avô.

ABSTRACT

The automotive industry is pressed with increasingly stringent efficiency and emissions goals. Vehicles are having increasing degrees of hybridization. Therefore, on-board electricity production seems highly attractive. Thermoelectric (TE) generators can directly convert the exhaust heat into electricity with no moving parts and unlike competing technologies, need little to no maintenance if carefully designed. However, they are temperature limited, and their electric output is very sensible to the thermal level. So, it is a challenge to design a system with optimized operation under the wide range of driving conditions.

A novel Temperature-Controlled Thermoelectric Generator (TCTG) concept incorporating thermal control through a phase change heat spreading device incorporated into the exhaust of a vehicle was previously proposed and modelled by the group. It incorporates corrugated pipes for exhaust flow, which are embedded in a cast aluminium matrix along with variable conductance heat pipes (VCHPs) working as excess heat spreaders. This concept is designed to maximize the absorption of exhaust heat under highly variable thermal load applications while still avoiding both thermal dilution at low loads and overheating at high loads. Wherever the temperature limit is exceeded at the hotter upstream regions of the heat exchanger (HX), heat is absorbed by vaporization and spreads to the colder regions of the heat exchanger by condensation. Therefore, in high thermal load events the excess heat is spread along the HX instead of being wasted through by-pass systems, as done in existing systems.

The present work performed the first full experimental validation of this concept and of the corresponding numerical model. Firstly, a previously built proof-of-concept prototype was instrumented and tested at ambient pressure with a resulting heat spreading temperature around 100°C. Subsequently, a new TCTG prototype capable of withstanding the operating pressures needed for optimal heat spreading temperature (~40 bar / 250°C) was built, attached to the exhaust of an Internal Combustion Engine (ICE) and tested. Evidence for the temperature control and heat spreading previously claimed for the concept was thus obtained for the first time. Results indicate that the system is able to maximize heat absorption under highly variable thermal load and achieve TE conversion efficiencies close to the theoretical maximum, with an electrical output level that seems to be a breakthrough for road vehicle TE generators, also showing promising results in terms of fuel consumption and CO_2 emissions reduction.

Key-Words: Thermal control; Thermoelectric generator; Variable conductance heat pipes; Variable thermal load; Waste heat recovery.

RESUMO

A indústria automóvel é pressionada com objetivos de eficiência e emissões cada vez mais rigorosos. Os veículos apresentam graus crescentes de hibridização, sendo que a produção de eletricidade a bordo parece altamente atrativa. Os geradores termoelétricos (TE) podem converter diretamente o calor de escape em eletricidade sem peças móveis se forem cuidadosamente concebidos. Porém, têm limitações de temperatura, e a sua produção elétrica é muito sensível ao nível térmico. Desse modo, é um desafio conceber um sistema com funcionamento otimizado sob a vasta gama de condições de condução. Um novo conceito de gerador termoelétrico com controlo de temperatura (TCTG), incorporando o controlo térmico através de um dispositivo de distribuição de calor por mudança de fase foi anteriormente proposto e modelado pelo grupo. Este, incorpora tubos corrugados para o fluxo de escape numa matriz de alumínio fundido juntamente com os heat pipes de condutância variável (VCHPs) funcionando como espalhadores de calor em excesso. Este conceito maximiza a absorção de calor de escape sob aplicações de carga térmica variável, evitando ao mesmo tempo a diluição térmica com cargas baixas e o sobreaquecimento com cargas altas. Sempre que o limite de temperatura é excedido nas regiões mais quentes a montante do permutador de calor (HX), o calor é absorvido por vaporização e espalha-se para as regiões mais frias do permutador de calor onde condensa. Portanto, em eventos de carga térmica elevada, o excesso de calor é espalhado ao longo do HX em vez de ser desperdiçado através de sistemas de by-pass, como acontece nos sistemas existentes. O presente trabalho efetuou a primeira validação experimental deste conceito e do modelo numérico correspondente. Primeiramente, um protótipo previamente construído foi instrumentado e testado à pressão ambiente, com uma temperatura de espalhamento de calor de cerca de 100°C. De seguida, foi construído um novo protótipo TCTG capaz de suportar as pressões de funcionamento necessárias para uma temperatura ótima de espalhamento de calor (~40 bar / 250°C), ligado ao escape de um Motor de Combustão Interna (ICE) e testado. Foram assim obtidas, pela primeira vez, provas para o controlo da temperatura anteriormente reivindicado para o conceito. Os resultados indicam que o sistema é capaz de maximizar a absorção de calor sob carga térmica variável e alcançar eficiências de conversão próximas do máximo teórico, com um nível de potência elétrica inovador para geradores TE de veículos rodoviários, mostrando também resultados promissores em termos de consumo de combustível e de redução de emissões de CO_2.

Palavras-Chave: Controlo térmico; Gerador Termoelétrico; Heat Pipes de Condutância Variável; Recuperação de calor de escape; TEG.

TABLE OF CONTENTS

Acknowledgments iii
Abstract vi
Resumo vii
Table of contents viii
List of Figures xii
List of Tables xvii
List of Acronyms and Abbreviations 1
List of symbols 3
1. INTRODUCTION 6
1.1 Motivation 6
1.2 Previous Research Group Survey 10
1.3 Thermal control through excess heat spreading 14
1.4 Objectives of the Dissertation 17
1.5 Structure 18
2. FUNDAMENTAL CONCEPTS AND LITERATURE SURVEY 19
2.1 Thermoelectricity 19
2.1.1 The Seebeck, Peltier and Thomson Effect 19
2.1.2 Thermoelectric Modules 22
2.1.3 TEG Electrical Output 25
2.1.4 Maximum Theoretical Power 25
2.1.5 Conversion Efficiency and Figure of Merit 26
2.1.6 Module Maximum Allowed Temperature and Improvements 28
2.2 Thermodynamics 30
2.2.1 Basic Concepts 30
2.2.2 Zero law of Thermodynamics 30
2.2.3 First law of Thermodynamics 30
2.2.4 Second law of Thermodynamics 31
2.2.5 Heat Transfer Concepts 32
2.2.6 Heat Exchanger Basic Concepts 34

2.3 Heat Pipes (HPs) and Variable Conductance Heat Pipes (VCHPs) 36
2.3.1 Historical Development 36
2.3.2 Principle of Operation 37
2.3.3 Working Fluid and Temperature Ranges 39
2.3.4 Types of Heat Pipes 40
2.3.5 Pressure Variation and Influence 43
2.4 State of The Art of Automotive Thermo-Electrical Generators 44
3. EXISTING PROTOTYPE AND MODIFICATIONS 50
3.1 TCTG Prototype Concept 50
3.2 TCTG Prototype Construction 55
3.3 TCTG Modifications 58
3.3.1 Water Supply System 58
3.3.2 Exhaust Gas Collectors 58
3.3.3 Thermocouple Installation 59
3.3.4 Load Resistances 60
3.3.5 Voltage Acquisition System 61
4. EXPERIMENTAL PROCEDURE FOR THE TESTS OF THE EXISTING PROTOTYPE 62
4.1 Experimental System Setup 62
4.1.1 Heat Exchanger and TEG Modules 63
4.1.2 Engine 64
4.1.3 Cooling water system 65
4.1.4 Data Acquisition system 65
4.1.5 Pressure 66
4.1.6 Temperatures 67
4.1.7 Voltage 67
4.1.8 LabVIEW® 68
4.1.9 ECUMaster® 68
4.1.10 MATLAB® 69
4.2 Test Procedure 70
5. RESULTS AND VALIDATION OF THE EXISTING PROTOTYPE 72

5.1 Experimental Results 72
5.1.1 Engine speed and available exhaust power 72
5.1.2 Heat Exchanger Effectiveness 73
5.1.3 Temperature Analysis 75
5.1.4 Electrical output and efficiency 78
5.1.5 Voltage and Power as a function of Temperature 81
5.2 Numerical Model Validation 83
5.2.1 Outline of The Model 83
5.2.2 Numerical model correction for heat capacity 86
5.2.3 Numerical Validation Results 86
5.3 Predictions for a system operating at 250°C 91
5.4 Fuel and CO_2 Savings 94
5.4.1 Compact TCTG Implementation 94
6. NEW PROTOTYPE CONSTRUCTION AND SET UP 97
6.1 New Design 97
6.1.1 New Heat pipes 98
6.1.2 Corrugated Pipes 98
6.2 New TCTG Construction 100
6.2.1 Casting Process 100
6.2.2 Machining Process 107
6.2.3 Excess Vapour Condenser 109
6.2.4 Relief Valve 110
6.2.5 TEGs and Cooling Plates placement 111
6.3 System Set-up 112
6.3.1 Exhaust Collectors 115
6.4 Brake Dynamometer 116
6.4.1 Calibration 118
7. RESULTS AND VALIDATION OF THE NEW PROTOTYPE 120

7.1 Engine 120
7.1.1 Heat Exchanger Effectiveness 121
7.1.2 Temperature Analyses 122
7.1.3 Electrical output and efficiency 123
7.1.4 Power as a function of Temperature 125
7.2 Fuel and CO_2 Savings 127
8. CONCLUSIONS AND FUTURE WORK 128
8.1 Future Work 131
References 133
Appendices 138
Appendix 1 – Hi-Z 14HV TEG Modules Datasheet 139
Appendix 2 – Security Valve Datasheet 142
Appendix 3 – Scientific Contribution 144
Annex 1 – Dynamometric Brake CALIBRATION CURVE 145
Annex 2 – Fuel and CO2 emission savings spreadsheet 146

LIST OF FIGURES

Figure 1-Divergence between official and real-world CO2 emissions for new passenger cars in the EU, the United States, China, and Japan [2][3]. 6
Figure 2 - Outline of the operation of a Thermosiphons heat exchanger by LaMoTA group [28]. 10
Figure 3 - Schematic representation of the excess heat spreading (a) enabled using VCHPs and (b) heat transfer process across the VCHP with the excess heat being absorbed in the vaporization region and released in the condensation region. 14
Figure 4 - (a) global and (b) cut overview of temperature-controlled thermoelectric generator concept based on corrugated tubes and VCHPs [36] 16
Figure 5 - Current flowing through a junction between 2 materials [24]. 20
Figure 6 - Detailed thermoelectric module [93]. 22
Figure 7 - Seebeck operating principle [43] 23
Figure 8 - TEG module electrical circuit 23
Figure 9 - SolidWorks illustration of a p-n junction pair [44]. 24
Figure 10 - Figure of merit ZT for common TE materials, as a function of temperature [46] 28
Figure 11 - Increase in the figure of merit of thermoelectric materials over the last years [52] 29
Figure 12 - Heat conduction along a body with thickness Δx and area A. 32
Figure 13 - Conventional heat pipe schematic view [61] 37
Figure 14 – Heat Pipe (a) sections and (b) fluid behaviour inside the pipe [61]. 38
Figure 15 - Outline of a Variable Conductance Heat Pipe operation [63]. 41
Figure 16 - Variable Conduction Heat Pipes Working Principle [38] 42
Figure 17 - 1 kW Generator Mounted on Cummins NTC350 Engine [70]. 45
Figure 18 - TEG power output as a function of the engine load and engine speed in tests with a) NTC335 engine and b) NTC350 engine [73][74]. 45
Figure 19 – (a), (b) 1kw Thermoelectric generator installed in a 550hp diesel engine [71]. 46
Figure 20 - Nissan´s 1998 TEG Prototype [76]. 46
Figure 21 - a) 180 W thermoelectric generator for Hybrid SUV and b) 330 W for Jeep Sierra Pickup from General Motors [94]. 47
Figure 22 – (a), (b) TEG Installed in a BMW 530i [82] [83]. 47
Figure 23 - Exhaust TEG system presented by WV in 2008 [81]. 48
Figure 24 - GMZ's 1KW Exhaust Heat TEG [74]. 48

Figure 25 - TCTG Prototype concept. 50
Figure 26 - a) Full TEG generator concept; (b) Section View of the corrugated tubes and VCHPs embedded in an aluminum matrix, along with the TEGs (red) and cooling plates. 51
Figure 27 - Corrugated Pipes CAD Drawing. 53
Figure 28 - a) HPs and corrugated pipes placement planning; (b) Corrugated pipes casting tests and (c) 3D printed Positioners prototypes. 55
Figure 29 - (a) Corrugated pipes and (b) HPs arrangement before casting; (c) Corrugated Pipes and HPs inside de moulding box ready for casting. 55
Figure 30 – (a) Interior finned surface of a cooling plate and (b) Final cooling plate. 56
Figure 31 – (a) HE after the aluminium cast, (b) HPs outside path construction and (c) TCTG after installation of TEGs, cooling plates, expansion vessels and pressure sensor. 57
Figure 32 – (a) inlet and (b) outlet water supply collectors and (c) fully built prototype with water supply system 58
Figure 33 - (a) inlet and (b) outlet exhaust gas collectors 59
Figure 34 - (a) Thermal grease and thin grooves drilled in the (a) cooling plates and (b) HX to install the thermocouples 59
Figure 35 - (a) Load resistances, (b) connected in series 60
Figure 36 – (a) NI-9025 D-SUB voltage card; (b) D-Sub 36 pin connector built and (c)Full voltage acquisition system 61
Figure 37 - Schematic representation of the facility. 62
Figure 38 - TCTG TEG modules upper-half. 63
Figure 39 - TU5JP4 Engine. 64
Figure 40 - Water Flow meter. 65
Figure 41 - (a) Data acquisition system table and (b) NI CompactDAQ modular system in blue. 66
Figure 42 - (a) Jumo Midas® differential pressure sensor; (b) GEMS® 3500 pressure sensor. 66
Figure 43 - LabView® software used to monitor and record TCTG data acquisition parameters during the test cycle. 68
Figure 44 - a) Engine Management Unit and b) ECUMaster software used to change and record engine parameters during the test cycle. 69
Figure 45 - Ready to test prototype. 70
Figure 46 - Engine Speed and exhaust power throughout the test cycle. 72
Figure 47 - Exhaust inlet and outlet gas temperature and HX Effectiveness. 74

Figure 48 - (a) Hot face temperature at each row of TEGs (upper-half) and total electric power; (b)..... 75
Figure 49 - TEG hot face evolution compared by (a) left and (b) right side. 77
Figure 50 - a) Row 1 TEG Voltage Output and b) Row 1 TEG Power Output. 78
Figure 51 - TEGs Power by Row and TEGs Total Power Output. 79
Figure 52 - TEGs efficiency during Test Cycle. 80
Figure 53 - TEG a) voltage and b) power as a function of temperature differential. 81
Figure 54 - (a) CFD simulation of a corrugated pipe; (b) 2D heat conduction simulation of the exhaust heat exchanger [39]. 84
Figure 55 - 1D Thermal resistance scheme extracted from the 2D heat transfer simulation of a section of the HX under active and inactive HP condition. 85
Figure 56 - Electrical Power output (a) experimental vs (b) predicted for the downsized proof-of-concept TEG operating with an excess heat spreading temperature of 100°C. 87
Figure 57 - TEG module's simulation results. 88
Figure 58 - Electrical output in function of the available exhaust power 88
Figure 59 - Steady State representation of Hot face Temperatures and Total Power 90
Figure 60 - Electrical power production by each TEG row of simulation for the same test cycle with the working fluid vaporization temperature of 250°C 91
Figure 61 - Electrical Power and Available Exhaust Power results for simulation with working fluid vaporization temperature of 250°C for the same test cycle of the eperimental results 92
Figure 62 - WTLC Cycle Electrical Power output vs Available exhaust heat simulation results 92
Figure 63 - New prototype design. 97
Figure 64 - (a) CAD model and (b) built stainless-steel Heat Pipes. 98
Figure 65 - Corrugated Pipes. 99
Figure 66 - CAD drawing of the moulding box. 100
Figure 67 - (a) Moulding Box and (b) Heat Pipe positioning inside the moulding box. 100
Figure 68 - (a) high temperature silicone and (b) after application on positioners. 101
Figure 69 - Moulding Box (a) before and (b) after the sand application and (c) close up of the discontinuity zone 101
Figure 70 - (a) Muffle Furnace and (b) digital display. 102
Figure 71 - (a) Melting Furnace, (b) de-gasification of the alloy using (c) Argon. 103
Figure 72 - Moulding box exiting the Muffle Furnace. 103
Figure 73 - Moulding Box placement for aluminium cast. 104

Figure 74 - (a), (c) side-view and (b) top-view of the moulding box after alluminium casting 104
Figure 75 - Problems found after the casting. 105
Figure 76 - (a) Moulding Box extraction and cooling (b) inside and (c) outside. 105
Figure 77 - (a) HX being cleaned and (b) sand being removed. 106
Figure 78 - Verification of the integrity of the end of the corrugated tubes and screws 106
Figure 79 - Weighted TCTG after casting 107
Figure 80 - (a) 6 pad milling cutter tool, (b) milling machine manufacture spindle rotation speeds and (c) machining process of the HX 107
Figure 81 - Preliminary Models of the final prototype. 108
Figure 82 - Final design of the Prototype. 108
Figure 83 - Prototype delivered by ENERGEST. 109
Figure 84 - (a) Excess condensers positioning and (b) close up view. 110
Figure 85 - Expansion Valve. 110
Figure 86 - (a) TEG preparation and (b) cooling plate cleaning. 111
Figure 87 - (a) TEG placement on the HX and (b) alumina sheets covering. 111
Figure 88 - Prototype after the assembly of the TEGs and the Cooling Plates 112
Figure 89 - Prototype after load resistance connected to the TEGs 112
Figure 90 - (a) Exhaust Gas Collector and (b) possible leakage sealing. 113
Figure 91 - Water supply system connections. 113
Figure 92 - (a) Exhaust gas collector connected to exhaust pipe and (b) coated with glass wool. 114
Figure 93 - (a)Exhaust Gas Collectors position in TCT;(b) Exhaust Collectors Sheet Metal Drawing, (b) MIG Welding on exhaust collectors and (c) junctions to connect the exhaust pipe. 115
Figure 94 - Dynamometric brake Scheme [92]. 116
Figure 95 - Brake Dynamometer system. 117
Figure 96 - Dynamometer Brake Controller. 117
Figure 97 - Dynamometric Brake Calibration Procedure. 118
Figure 98 - Calibration Sheet for the Brake Dynamometer. 119
Figure 99 - (a) Engine RPMs and Available Exhaust Thermal Power throughout the final test cycle and (b) Engine/dynamometer brake parameters. 120
Figure 100 - Exhaust inlet and outlet gas temperature and HE Effectiveness (Final Test). 121
Figure 101 - a) Hot face temperature at each row of TEGs (top) and (b) Heat Pipe inner pressure Evolution. 122

Figure 102 - (a) TEG Power Level by row and (b) Total Power vs Theoretical Max Power..... 123
Figure 103 - TEG efficiency during the final Test Cycle..... 124
Figure 104 - TEG (a) voltage and (b) power as a function of temperature differential. 125

LIST OF TABLES

Table 1 -Working fluids and temperature ranges of heat pipes [61] 39
Table 2 - Hi-Z 14HV TEG module datasheet [87] 64
Table 3 - Engine Properties 64
Table 4 - Pressure Sensors datasheet from manufacture 67
Table 5 - Mean Values of Test in Full Operation 81
Table 6 - Simulation Results for Numerical Validation of the Experimental Test 89
Table 7 - Simulation results for Full Sized prototype 93
Table 8 - Alternator and TEG output chain of conversion 95
Table 9 - Vehicle and Alternator Fuel Power savings using TEGs 95
Table 10 - Fuel Power Savings implementing TCTG 95
Table 11 - Savings from using TCTG (Using TEGs GM250-12) [36] 96
Table 12 - Mean Values of Test in Full Operation (New Prototype) 125
Table 13 - Vehicle and Alternator Fuel Power savings using new TCTG 127

List of Acronyms and Abbreviations

1D	One-Dimensional
2D	Two-Dimensional
AFR	Air-Fuel Ratio
BEV	Battery Electric Vehicle
CC	Constant Conductance
CFD	Computer Fluid Dynamics
CLT	Coolant Temperature Sensor
CNG	Compressed Natural Gas
CO_2	Carbon Dioxide
EGR	Exhaust Gas Recirculation
emf	Electromotive Force
EMU	Engine Management Unit
GHG	Greenhouse-Gas
GUI	Graphical User Interface
HP	Heat Pipes
HW	High Way
HX	Heat Exchanger
IAT	Intake Air Temperature
ICE	Internal Combustion Engines
NCG	Non-Condensable Gas
ORC	Organic Rankine Cycle
RPM	Revolutions Per Minute
TCTG	Temperature Controlled Thermoelectric Generator
TE	Thermoelectric

TEG	Thermoelectric Generator
TPS	Throttle Position Sensor
VC	Variable Conductance
VCHP	Variable Conductance Heat Pipes
VCHP	Variable Conductance Heat Pipes
VCTS	Variable Conductance Thermosiphons
WHR	Waste Heat Recovery
WLTC	Worldwide Harmonized Light Vehicles Test Cycle
ZT	Thermoelectric Figure of Merit

LIST OF SYMBOLS

Latin variables

A	Surface Area	m^2
C	Electric Conductance	S
C_p	Specific heat capacity at constant pressure	J/kg·K
D	Diameter	m
E	Energy	J
h	Convection heat transfer coefficient	$W/m^2 \cdot K$
I	Electric Current	A
l	Length	m
$\dot{m}$	Mass flow rate	kg/s
N	Number of Pairs	-
N	Engine Speed	RPM
P	Power	W
$\dot{Q}$	Thermal Power	W
$\dot{Q}_h$	Thermal Power Absorbed by the TEG module	W
$\dot{Q}_c$	Thermal Power Released by the TEG module	W
R	Resistance	Ω
T	Temperature	°C or K
T	Torque	N.m
t	Time	s
U	Internal Energy	J
V	Voltage	V
$\dot{V}$	Volumetric Flow rate	m^3/s

V_c	Cut Speed	m/s
W	Work	J

Greek variables

Δx	Thickness	m
α	Seebeck Coefficient	V/K
η	Efficiency	%
λ	Thermal Conductivity	W/(m·K)
π	Peltier Coefficient	J/C^{-1}
ρ	Electric Resistivity; Density	Ω/m; kg/m^3

Subscripts

amb	Ambient
c	Cold-side
ext	Exterior
h	Hot-side
I	Inlet
i	Internal
L	Load
m	Material
max	Maximum
o	Outlet
t	Total
vap	Vaporization
x	Thickness

1. INTRODUCTION

1.1 Motivation

The discovery in 2015 of an illegal exploit on 590 000 Volkswagen diesel engine vehicles led to the manufacturer acknowledging that more than 8 million passenger cars were equipped with a device that would cause the strong under-estimation of emissions to enable the vehicle to comply with the challenging emissions standards [1]. Following the event, several independent European organizations conducted emissions testing under the Euro 5 and Euro 6 in standard passenger cars. This event awakened public concern on whether road vehicles, which in recent years had shown a very promising reduction in greenhouse gas and pollutant emissions and fuel consumption [2], were in fact complying with these targets. Previous research has found that there was a gap between official type-approval and real-world CO_2 emission. Some authors [3] stated that the gap has grown from less than 9% in 2001 to around 40% in 2015 (see Figure 1). In terms of fuel consumption, [4] when analysing real-world fuel consumption data from German car manufactures company cars (that represent almost half of new cars registrations in Europe [2]) found that the average divergence between on-road and official values increased from approximately 10% to 50% from 2004 to 2014.

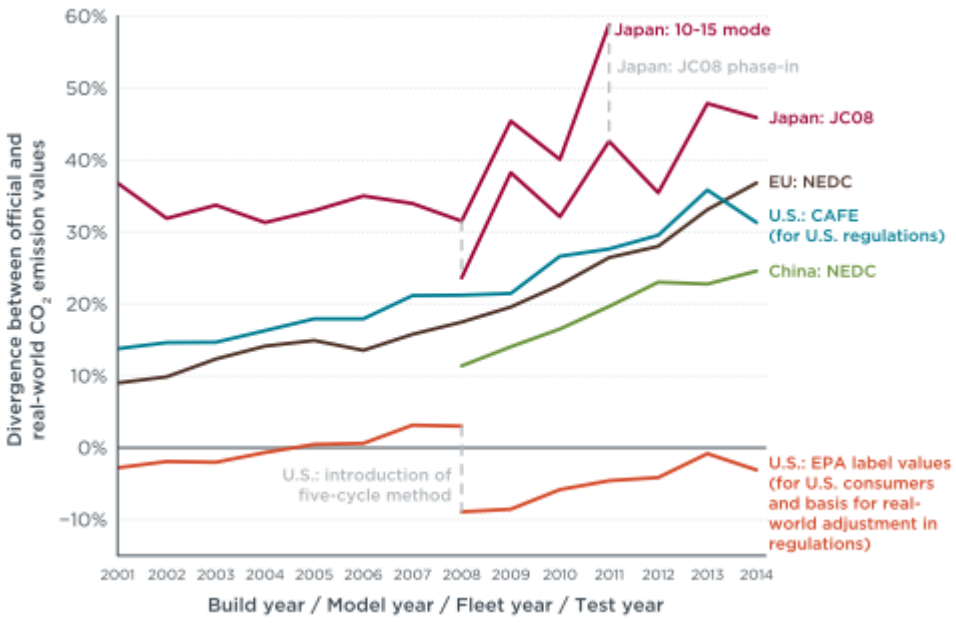

Figure 1-Divergence between official and real-world CO2 emissions for new passenger cars in the EU, the United States, China, and Japan [2][3].

The above-mentioned data suggests that car manufacturers are struggling to keep up with targets for fuel consumption and emissions as they are forced to comply with very challenging sustainability goals. The research and development for upcoming years will be looking towards implementing technologies allowing to accomplish targets in energy consumption as well as lower pollutant and greenhouse-gas (GHG) emissions [5]. The EU has recently reviewed their GHG emissions emission cuts goal for 2030 increasing it to 55% in relatively to 1990 levels [6]. Regarding heavy duty vehicles, in 2025 and 2030 these need to achieve a 15% and a 30% reduction, respectively, when compared to 2019/20 levels [7].

These targets are very challenging. Full vehicle electrification is perceived as a very promising approach as GHG emissions during vehicle driving are eliminated. There has been a push by several policy makers to favour exclusively this type of transportation while sometimes pushing for the outright ban of the ICE-based vehicle in the long-term. A notable motivation behind these radical approaches seems to be the ill-perceived notions of BEVs (Battery Electric Vehicles) as being "emissions-free" vehicles and of ICE-based vehicles as being "emissions-bound" vehicles. Neither notion is accurate, denoting a lack of familiarity with life cycle analysis of emission footprint: The assessment of emissions footprint of BEVs is often reduced to the driving phase, with no acknowledgement to the fact that there are emerging technologies and fuels that can render the ICE an emissions-neutral machine [8], [9]. This reductionist approach risks eliminating valid solutions for the challenge of GHG emission reductions in the medium- and the long-term future. BEVs still have their own sustainability challenges, although these are not always present in policy discussion. The indirect emissions associated with electricity production and the Life Cycle impact at the beginning/end of life of components such as energy storage are issues that still need to be properly addressed [10]. Also, several technical challenges, mostly related to energy storage, still prevent their quicker and wider adoption. Still, light duty BEVs are being increasingly adopted, especially in urban transportation, where there are most advantageous [5], [11]. Their selling share increased from 3.5% in 2019 to 11% in 2020 in the EU [12]. Regarding heavy-duty long-distance transportation, it is expected that the rate of adoption of full electrified powertrains will be much slower, with several decades still needed to pass before mass adoption of full electrical powertrains takes place [5].

A lot of progress has also been made regarding fuels that are low on fossil emissions, such as compressed natural gas (CNG), or achieving a neutral carbon footprint, as the case of synthetic fuels made from renewable sources and waste-derived fuels, in which the CO_2 emissions in the tailpipe are neutralized by the CO_2 sequestrated during their sustainable production [13], [14].

While the use of ICE-based vehicles is expected to decline steadily over the next decades, they still account for most of the transportation sector nowadays [5]. To neglect the research effort towards solutions that

may improve their current and future sustainability seems not to be a wise decision. Meanwhile, vehicle manufacturers are urgently in need of reducing their carbon footprint to reduce the penalty they are presently experiencing when failing to meet the current emissions limits. For instance, manufacturers of passenger cars are paying 95 € for each g/km exceeding the 95 g/km target per vehicle. In 2020 the average EU emissions were 107.8 gCO_2/km, which is almost 13 g/km in excess of the target, meaning an average fine per car exceeding 1.2 k€ [12]. Therefore, measures are needed to tackle this issue.

It seems obvious that the transition towards fully sustainable transportation requires the use of more readily available solutions in the short to medium term. Hybridization and partial powertrain electrification can play a huge part in reducing substantially GHG emissions, as they allow for the recovery of braking energy and allow the engine to work at regimes closer to their top efficiency conditions [15], [16]. Besides vehicle hybridization, a significant increase in vehicle efficiency can be achieved both in ICE improvement and by recovering a portion of the high-amount of energy not converted by the engine. On average, only up to one third of the fuel energy burned in an petrol engine (up to 40% on diesel engines) is converted to work at the transmission shaft, with the engine coolant and the exhaust dissipating roughly another third of that energy each [17].

It is important to note that the energy wasted by the ICE through the exhaust has a higher recovery potential than the energy lost through engine cooling since exhaust gas temperatures are much higher than engine cooling circuit temperatures, overcoming 700 °C or more [18]. Chammas and Clodic [19], when analysing characteristics of a common light duty 4-cylinder spark ignition engine stated that, depending on regime conditions, exhaust waste thermal power would mostly range from 4.6 to 120 kW while the cooling water thermal power would mostly range from 9 to 48 kW only. Parallel to the increasingly tight targets in terms of fuel consumption and emissions it is noteworthy the increased demand of electricity for on-board applications in light and heavy duty vehicles [20]. Therefore, the conversion of a portion of the exhaust heat into electric energy could be translated into a substantial saving in GHG emissions. Some researchers have studied the potential of Organic Rankine Cycle (ORC) as it reconverts a part of the available exhaust enthalpy into mechanical work, then reconverting to electrical power. Theoretically, the efficiency gains can be expected to be in the order of 3 to 8% [21]–[23]. Other solution to harvest this energy is to transform the thermal energy directly into electrical energy without the need for an intermediate conversion into mechanical energy as in the case of ORC. This is possible using thermoelectric generators (TEGs). These produce electricity if there is a temperature difference across the module faces because of the Seebeck effect. The exhaust heats the hot face, and a coolant flow keeps the opposite face at a minimum temperature [24].

TEGs have been assessed as a possible nearly maintenance free Waste Heat Recovery (WHR) solution for long. However, viable market solutions are still not a reality. While material costs are steadily being overcome with novel affordable TE materials, such as those developed by the Lab [25], there is still the issue of low average conversion efficiency under realistic driving conditions. This is caused by the fact that the average efficiency of TEGs is heavily deprecated when the thermal level of the modules is not close to their optimum, which coincides with their operating temperature limit. In practice, it is a nearly impossible challenge to thermally optimize the TEGs under highly variable conditions of exhaust flow rate and exhaust temperature during real-world driving. This thermal optimization mainly means that the hot side temperature should be as close as possible to the maximum allowable temperature of the modules, but not higher, at the risk of damaging the module. In low and medium thermal level events it is desirable to have an exhaust heat exchanger with very low thermal resistance, to induce a very high effectiveness. However, in high thermal level events, the exhaust gases temperature can achieve more than 700 °C and the low thermal resistance of the HX may induce overheating. Given that affordable, commercially available TE materials are temperature limited, it seems that to enable viable, efficient automotive TEGs it would be necessary to develop a HX with a low thermal resistance in combination with some kind of thermal control to provide an optimal thermal level to the modules irrespective of the thermal load.

1.2 Previous Research Group Survey

In previous work, the LaMoTA Research Group has proposed to solve the challenge of thermal control through two alternative concepts, both based on liquid to vapour phase change at a controlled temperature range. The original concept was based on the absorption of all the exhaust heat through variable conductance thermosiphons (VCTS) that would deliver this heat to the TEGs at a fairly uniform temperature irrespective of exhaust thermal load [26],[27]. A later concept was slightly different. Instead of using VCTS to transfer all the heat to the modules, it implemented variable conductance heat pipes (VCHP) embedded along an otherwise conventional exhaust HX to spread solely the excess heat from hot spots to cold spots of the HX. The VCHPs would basically operate as spreaders of excess heat.

The VCTS incorporates an evaporator at the exhaust, a condenser to which the TEG modules are attached and an expansion tank for pressure stabilization (see the schematic figure of the concept in Figure 2). The evaporator absorbs the exhaust heat through vaporization of a fluid (water) at a controlled boiling temperature (~260 °C) and releases this heat to the condenser, along which the hot faces of TEG modules are attached. Therefore, these modules do not receive the exhaust heat directly from an exhaust heat exchanger but indirectly through the condensation of vapour that was generated with the exhaust heat.

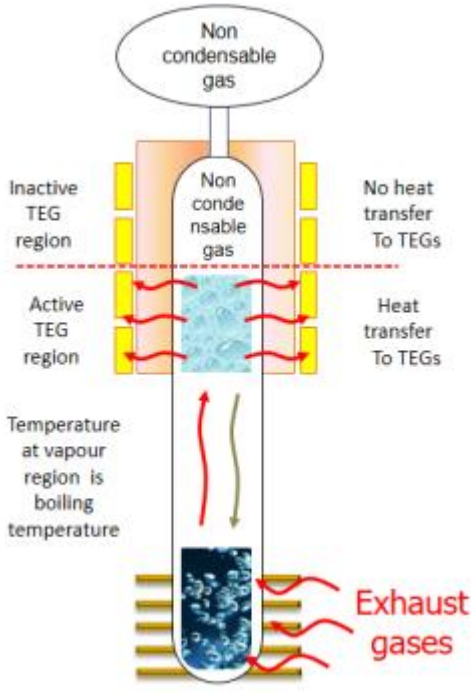

Figure 2 - Outline of the operation of a Thermosiphons heat exchanger by LaMoTA group [28].

By pre-regulating the pressure of the system with a non-condensable gas (NCG), it was possible to regulate the boiling temperature of the vapour, and thus the heat transfer temperature. Additionally, the

implementation of an expansion tank allows to maintain a relatively stable inner pressure and thus a stable boiling temperature irrespective of the engine regime. At rest, the VCTS is filled with the NCG at a given pre-load pressure. Once vapour starts to be generated at the evaporator, it will gradually expand and fill the system, eventually reaching the condenser, where modules are attached. Once the vapour condenses, it releases its latent heat, with the condensates returning to the evaporator by gravity (VCTS) or by capillary force (VCHP). This heat will then reach the hot face of the modules attached to the condenser. The cold faces of these modules are attached to liquid-cooled heat sinks. The temperature difference generated between the hot a cold face of the modules will cause a voltage through the Seebeck effect. Because the non-condensable gas is present and there is some stratification between the vapour and the NCG (see Figure 2), there will be a lower or a higher fraction of the condenser that will be filled with vapour (active heat transfer area). The remainder area will be filled with the NCG (non-active heat transfer area). The active heat transfer area will be proportional to the thermal load at the exhaust.

Therefore, the variation of the engine load along the driving cycle will affect mostly the number of active modules (modules located at the vapour region of the condenser) and not so much the temperature of the modules, which will be fairly stable with the help of the expansion tank. The vapour temperature was regulated some degrees above the maximum TEG module temperature, T_{max}, so that the hot face of these modules would be around T_{max} (250 °C). This way, it was possible to protect the system against over-heating without wasting heat with a bypass system, while absorbing a substantial portion of the heat from a highly variable heat source. Moreover, due to the accumulation of vapour in the system it is possible to have excess heat accumulation

Initially, simplified proof-of-concept prototypes were built and tested with a blowtorch as heat source to confirm the effects [29]. It was confirmed that indeed it is possible to stabilize the heat transfer temperature irrespective of the heat input, with this temperature being only a function of the inner pressure of the system.

Systems with growing size and complexity were subsequently implemented and tested [30]. For instance, the influence of the VCHP operating temperature on the exhaust heat recovery was assessed both theoretically and experimentally [31]. For this purpose, a small capacity Proof-of-Concept thermoelectric generator with 3 blocks of 4 thermoelectric modules each was built and tested for a range of operating temperatures (100-160 °C). The predictions and the tests showed that although the efficiency of the modules increases with the operating temperature, the increasing of Heat Pipe (HP) temperature beyond a certain limit eventually causes the degradation of the electric generation due to the reduction of the

usable exhaust energy. This study was complemented by another one incorporating a more detailed model of the system and a validation with the exhaust of a small diesel engine [32].

In parallel, a theoretical study [33] on the effects of TEG thickness in performance of this modules energy production output was also carried out, highlighting the importance of minimizing aspects such as contact resistances in order to use high thermal power modules that theoretically could maximize electrical input of TEGs.

A larger vertical full-size prototype was designed and built by the research group to fully explore the temperature control concept with the system being connected to a spark ignition engine. The mathematical model proposed in [32] was much improved in [34] in order to predict the behaviour of a temperature controlled TEG based on the design of this larger VCTS-based prototype under realistic driving cycles. This numerical approach modelled the heat transfer at the evaporator using an unsteady implicit heat transfer model, implementing empirical correlations and calculating the rate of vapour production along the cycle. The rate of vapour condensation at the condenser and the resulting active condenser/module region was also calculated along the time, considering a constant inner pressure. This allowed to estimate the output power and efficiency of the system along the driving cycle. It was possible to observe the optimized operation of the system, with the thermal-control maintaining the optimal thermal level of the active modules (meaning top efficiency) under broadly variable engine loads without the risk of overheating or thermal dilution. This was assessed under the Worldwide Harmonized Light Vehicles Test Cycle (WLTC) and a higher thermal load custom Highway (HW) cycle.

More recently [35], the previous model was updated to allow for the prediction of the pressure and boiling temperature evolution along the same driving cycles, including unsteady heat transfer calculations and a warm-up period in which only sensible heat is present. It was found that the pressure has a variation which is inversely proportional to the volume of the system. It was also found that allowing for some variation of the inner pressure and the corresponding boiling point (by using smaller expansion tanks) the performance of the system could be improved, as the system would start generating vapour earlier in the driving cycle. Maximum/average power outputs of 874 W/ 283 W were estimated for the WLTC cycle, respectively. Regarding the higher power HW cycle these values were 1.04 kW for the maximum output and 563 W for the average. These seem to be highly attractive figures for such a light vehicle as the one simulated (1.4L S.I. engine hatchback). It was found that the implementation of the TEG system as an alternator substitute could result in 6% fuel savings and CO_2 reductions.

All the aforementioned studies were made with gravity-based (VCTS-based) TE generators, in which all the heat was supplied to the TEG via the phase-change fluid. Although the predictions were promising for

automotive TEGs compared to the state-of-the-art, the concept had some challenges for implementation. The most notorious one was its vertical configuration, which is not convenient for light duty vehicles. Another downside from the design was that it is not possible to extract all the heat from the exhaust gases. That is, exhaust gases would never exit the system at a temperature below the phase change temperature. This created the need for a new design that would be capable of overcoming the aforementioned limitations, which is described in continuation.

1.3 Thermal control through excess heat spreading

In the previous design, thermal control was achieved by delivering all the exhaust heat to the TEG modules through phase change process which, for a given pressure is nearly isothermal. One alternative of performing thermal control with phase change is the one proposed by the authors in [36], which is outlined in Figure 3. It consists of performing the bulk of the heat transfer in a conventional way (absorption of the exhaust heat by convection at the HX, followed by transmission of this heat to the modules by conduction across the HX body). Only a small part of the heat transfer, if any, will be processed through the phase change process. It will only be present in regions where there is excess heat, that is, in regions where the temperature would otherwise exceed the limit if no phase change fluid would be present.

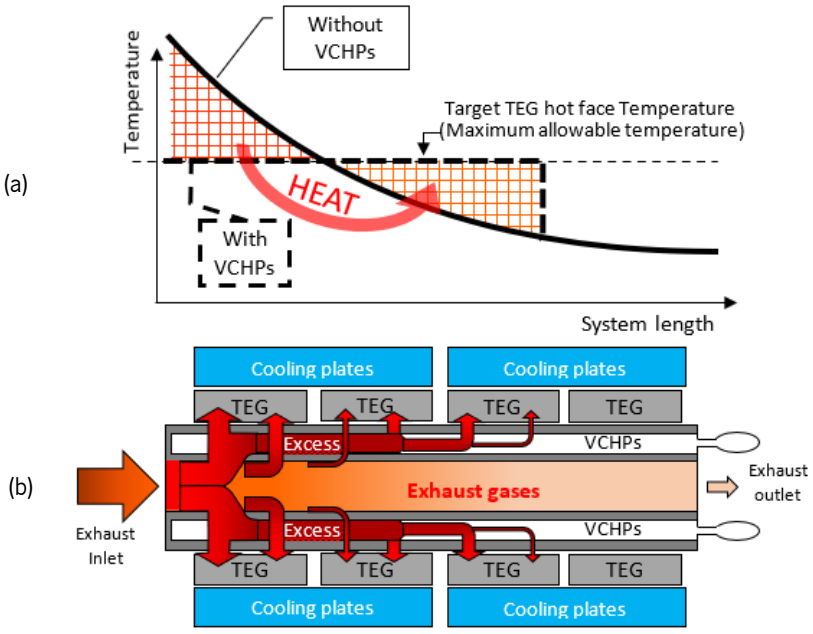

Figure 3 - Schematic representation of the excess heat spreading (a) enabled using VCHPs and (b) heat transfer process across the VCHP with the excess heat being absorbed in the vaporization region and released in the condensation region.

The idea is to embed chambers along the HX that contain the phase change fluid. Boiling will occur within these chambers wherever the boiling temperature is achieved. Similarly, to previous concepts, this temperature is regulated to be close to the maximum allowable operating temperature of the TEG modules. This is done, again, by regulating the pressure inside the system, using a non-condensable gas (NCG). This boiling will provide two advantages: locally, it will prevent further temperature increase above that limit temperature. But at the same time, the excess energy absorbed by boiling in hotter, upstream regions of the HX, will spread along the HX and will be used to heat up colder regions located downstream

in the HX by condensation. That is, the vapour generated at these excess heat regions will spread along the HX chambers and fill them until it condenses at under-heated regions of the HX, heating them up to the optimal temperature.

Therefore, a similar effect to the previously described concept is obtained, but in a different way: Similarly to previous concepts, the heat absorbed by the HX will be distributed along an area of TEG modules proportional to the thermal load, with these modules displaying an optimal temperature level. However, in this new concept only the excess heat needs to be transported by the phase change fluid, not the whole heat, as in the case of the previous concept. Also, the system can now absorb a higher fraction of the exhaust heat and, unlike the previous system, exhaust heat will still be absorbed even when its temperature drops below the phase change temperature. Thus, this seems to be a solution able to passively avoid TEG overheating at high thermal load while efficiently using the available heat, because local excess heat is not wasted but spread to under-heated regions. At low thermal loads efficient operation will also be possible because it is possible to minimize the thermal resistance of the HX (maximize HX effectiveness) without the fear of overheating under high loads.

This could be achieved using Heat Pipes (HPs) with adjustable boiling temperature, such as the Variable Conductance Heat Pipes (VCHP). A concept of a compact system based on VCHPs which does not requires gravity to operate has been designed and submitted for patenting [37]. One of the advantages of this system is that it can display a very low thermal resistance without the fear of overheating at high thermal loads. This solution allows maximizing the HX effectiveness for variable thermal load conditions. One design incorporating this concept was assessed in a publication of the group [36]. It incorporated corrugated pipes identical to those used in exhaust Gas Recirculation coolers from BorgWarner® that were embedded, along with the VCHPs in a cast aluminium body. The hot face of the modules was attached to the aluminium block, while the cold face of the modules was attached to liquid cooling plates. The concept was modelled and optimized geometrically and it can be seen in Figure 4.

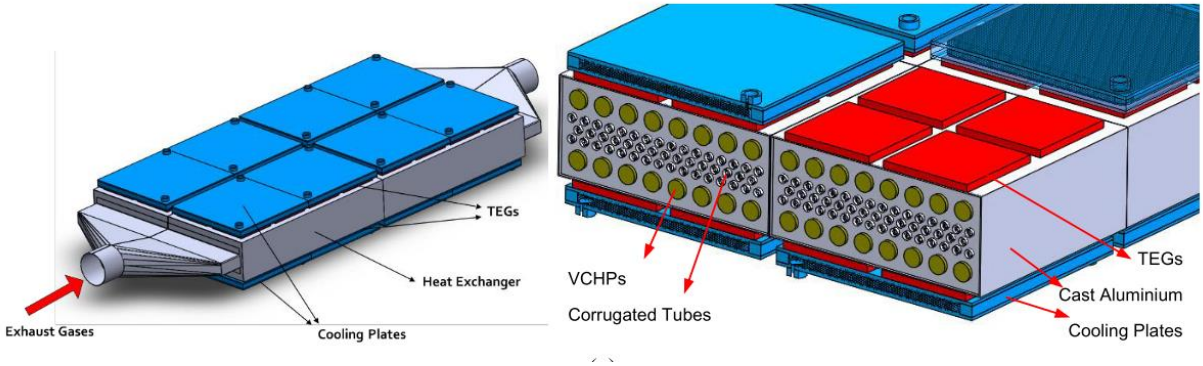

(a) (b)

Figure 4 - (a) global and (b) cut overview of temperature-controlled thermoelectric generator concept based on corrugated tubes and VCHPs [36] .

The results were very promising even when discounting for the backpressure losses induced by the system as it was predicted to be capable of delivering as much as 572 W and 1538 W of average and maximum electric powers during a driving cycle, respectively, and showing a quite promising reduction of 5.4% in fuel consumption and CO_2 emissions [36].

Some CFD simulations were included in the publication validating partly the model. However, a full experimental validation was still missing to confirm the excess heat spreading feature and in general the thermal control capability of the concept. The present work aims to address this issue.

1.4 Objectives of the Dissertation

The main objective of this work is to perform the experimental and mathematical validation of the novel compact Temperature controlled Thermoelectric Generator (TCTG). It embodies corrugated pipes embedded in aluminium matrix working along with variable conductance heat pipes (VCHPs) working as excess heat spreaders for temperature control to be used in highly variable thermal load applications such as driving. This concept, that has been introduced in 1.3 an will be described in detail in 3.1, was patented recently [40]. An embodiment of his concept incorporating embedded corrugated pipes (exhaust flow) and VCHPs in a cast aluminium matrix, was assessed theoretically in recent publications by the LaMoTA team but had not been validated experimentally until now.

Therefore, the present dissertation had as a main goal to perform the experimental validation of this concept and of the code that has been proposed to model it. For that, two similar downsized proof-of-concept prototypes of the generator proposed in [36] have been configured and tested. A first one, that was built within a previous project, was instrumented and tested at gauge pressures close to atmospheric, yielding excess heat spreading temperatures around 100 °C. A second one was designed and built within the dissertation and relied on stainless steel VCHPs able to withstand the pressures needed to achieve excess heat spreading temperatures around 250°C. Both prototypes were suitably instrumented and tested after being attached common light duty 1.6L 4-cylinder spark ignition engine in an engine dynamometer. The experimental results were then used to confirm the principle of operation of the concepts conjectured in previous analyses and validate the mathematical models proposed in those analyses.

1.5 Structure

This dissertation is divided into seven chapters. The first chapter "Introduction," provides a general outline of the objectives and motivation of the work, as well as some previous research aligned with the already studied concept of excess heat spreading through phase change.

Secondly, there is a chapter on the "Fundamental Concepts and Literature Survey" where the central concepts essential to understand the design of prototype tested are described. It includes the basics of thermoelectricity, thermodynamics, heat transfer fundamentals, heat pipes and their principles of operation, a state of the art of exhaust heat recovery systems and compact heat exchanger solutions.

Chapter three "Previous Prototype and Modifications" assesses the prototype in which this work started, stating it´s concept of operation and how it was built, as well as the modifications that were made in order to perform the experimental tests.

In chapter four, "Experimental Procedure on Existing Prototype," the experimental system setup and its components are explained. In addition, the experimental test procedure is described.

The results of the experimental test and the numerical validation are presented and analysed in chapter five "Results and Validation of the Existing Prototype".

Chapter six "New Prototype Construction and Set Up" presents the new design for a final TCTG prototype, explaining in detail the novel components as well as the construction of this new TCTG.

Finally, chapter seven "Results and Validation of the New Prototype," summarizes the results of the experimental tests performed to the new TCTG along with the main achievements and contributions of the dissertation to the field of study.

2. FUNDAMENTAL CONCEPTS AND LITERATURE SURVEY

In this chapter the fundamentals concepts and literature survey necessary to understand the covered thematic are summarized. Starting with thermoelectricity, where de concept of Seebeck effect and thermoelectric modules is presented as well as one of its most prominent characteristics: temperature limitations. Followed by a brief summary on thermodynamics and heat transfer concepts. The present chapter also contains a detailed analysis on Heat Pipes technology and its functioning, ending with a state of the art of waste heat recovering thermoelectrical solutions.

2.1 Thermoelectricity

Thermoelectricity is a phenomenon dealing with the direct conversion of thermal to electric energy, or the reverse [24]. In parallel with environmental concerns, the use of Thermoelectric technology is of interest for the automotive industry. Thermoelectric generators can transform the exhaust heat directly into electrical energy and therefore decrease the fuel consumption in vehicle. In terms of vehicle application, vibrations, accessibility and maintenance are obstacles to be taken into account. Therefore, the opportunity to design a robust, maintenance-free Thermoelectrical Generator with no moving parts aiming to recover exhaust heat seems a reliable solution.

2.1.1 The Seebeck, Peltier and Thomson Effect

In 1821 Thomas Johann Seebeck discovered what is known today as The Seebeck Effect (SE). It is described when an electrical potential (voltage) is generated within any isolated conducting material that is subjected to a temperature difference across its junctions [24]. The ordinary example where this phenomenon is applied is to form a thermocouple composed of two dissimilar current-carrier junctions. The application of a temperature difference across the junctions of the pair of materials will produce a voltage that is approximately proportional to this difference. This Seebeck voltage, also known as thermoelectric electromotive force (emf) is defined as follows:

$$V_o = \alpha \cdot \Delta T \tag{1}$$

The V_o is the Seebeck voltage generated for the condition of an open circuit, ΔT is the temperature differential between the junctions. The magnitude of the emf generated is proportional to the temperature

difference, and the Seebeck Coefficient (α) of the specific material or pair of materials. The Seebeck Coefficient (α) corresponds to the gradient of the Seebeck Voltage relatively to temperature, as it follows:

$$\alpha = \left[\frac{d(V_o)}{dT}\right]_T \tag{2}$$

Later in 1983 Peltier observed that when an electrical current passes through two different conductors connected in a loop, one of the junctions between the conductors absorbed heat while the other one released heat [41]. The heat liberation or absorption depended on the direction of the current. Figure 5 displays a current *I* flowing through a junction formed between two different materials *A* and *B* held at a constant temperature *T*.

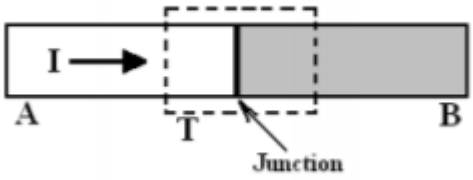

Figure 5 - Current flowing through a junction between 2 materials [24].

The Electrical current will generate a heat fux and its magnitude and direction depends on the Peltier Coefficient (π) of each material *A* and *B*. If the Peltier Coefficient are different, the thermal energy will leave the junction at a different rate that it is entering [41]. Thus, heat is absorbed or liberated at the junction. The Peltier effect (PE) can be defined as:

$$q_\pi = \pi \cdot I = \alpha \cdot T \cdot I \tag{3}$$

q_π is defined as the rate of heat liberation or absorption, π is the Peltier coefficient and I is the flowing current. It can also be seen from above that in reality, the Peltier coefficient is related to the Seebeck Coefficient, being the latter multiplied by the absolute temperature, *T*.

In 1851, William Thomson postulated the existence of an additional reversible heat generation when a temperature differential is applied on a current carrying material [42]. Therefore, the Thomson heat it is

reversible and heat is either generated or liberated when the direction of the current or the temperature different is reversed. It is proportional to the current and the temperature gradient. It is defined as:

$$q_\mu = \mu \cdot I \cdot \Delta T \tag{4}$$

q_μ is the rate of heat absorption per unit volume, μ is the Thomson coefficient to the applied current and temperature gradient, I is the current and ΔT is the temperature differential. The Thomson coefficient can also be obtained from the Seebeck Coefficient, as it is a function of its gradient with temperature. For a Seebeck coefficient that would be constant with temperature, a zero Thomson coefficient would result. In reality, the Thomson effect in a conductor results from the variation of the heat transport due to the variation of Peltier effect along the electricity path, due to the variation of temperature. If the capacity to transport heat by the charge carriers reduces along the current path, then heat must be released to the material along the way (Thomson heat source). On the contrary, if the capacity to transport heat by the charge carriers increases along the current path, then heat is absorbed by the charge carriers along the current path (Thomson heat sink).

The above-mentioned effects are of practical importance since TE power generation results from the existence of a temperature gradient across a material attached to hot source and a heat sink. In power generation the Seebeck effect is the most important, but the Peltier and Thomson effects are also present due to the current induced by the Seebeck electromotive force. The Thomson effect can be neglected in most applications, but the Peltier effect will have an effect on the heat flow and on the effective temperature difference across the hot and cold junctions, deprecating it.

The maximum electrical power generated by a Seebeck effect working device is obtained when the load resistance coincides with the internal resistance, R_i, of the pairs:

$$P = (n\alpha\Delta T)^2/4R_i \tag{5}$$

The formal deduction of this equation is performed in 2.1.4. It is a function of the electrical resistance of the module R_i, Seebeck coefficient of the pair of materials and the number of element pairs n.

2.1.2 Thermoelectric Modules

When aiming to generate electrical power using temperature differential, Thermoelectric Generators (TEGs) generators can be a possible solution. The TEG functioning principle translates into multiply the number of thermocouples to also multiply the voltage generated. The main components of a TEG are represented in Figure 6.

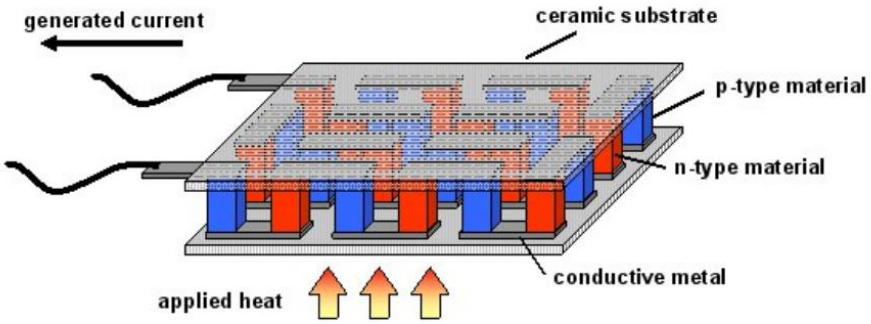

Figure 6 - Detailed thermoelectric module [93].

The temperature differential between hot and cold face causes charge carriers of each element to flow from the hotter to the colder regions of the element. The particularity of these two different materials is that in the n-type materials the charge carriers are electrons, which flow from the hot to the cold junction. therefore, the conventional direction of the current (from positive to negative) will be from the cold to the hot junction. On the other hand, in the p-type materials the charge carriers are electron holes (in practice, positive charge carriers), which also flow from the hot to the cold junction. Therefore, the conventional direction of the current (from positive to negative) will be from the hot to the cold junction. Since the p-n pairs are arranged in zig-zag series through the electric connectors (see Figure 6), a current is created along the TEG.

Numerous pairs are electrically connected in series and thermally in parallel. Each pair has two different elements, p-type with a positive α and a n-type with negative α [42] [43]. In Figure 7 it is possible to understand the working principle of the TEG.

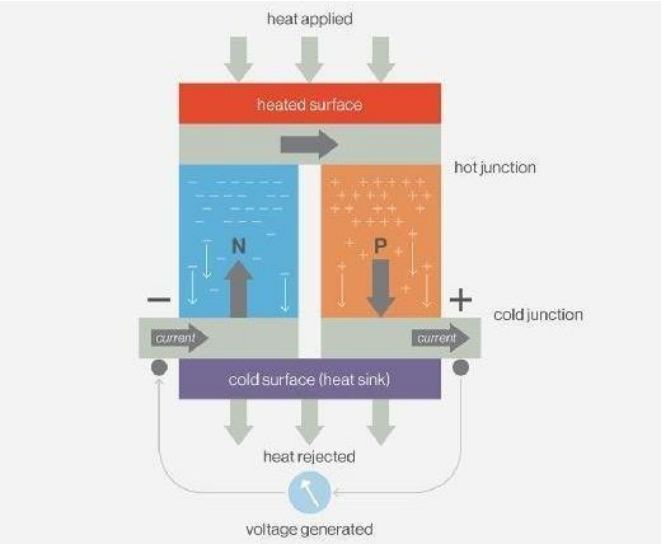

Figure 7 - Seebeck operating principle [43]

Under open circuit conditions, the voltage generated by the converter is proportional to the number of p-n pair junctions multiplied by the difference of Seebeck coefficients between the p-type and n-type thermoelectric elements and the temperature difference between the faces as follows: (Note that α_n is negative, so in practice, both Seebeck coefficients will be summed in module).

$$V_o = N \cdot (\alpha_p - \alpha_n) \cdot \Delta T \tag{6}$$

The module also has an internal resistance R_i. Therefore, it can be represented in a simplified way as consisting of a voltage source with voltage V_o calculated according to eq. (6), and an internal resistance R_i. To produce power, the module must be connected to a load, that is, the device that will consume the electric power produced by the module. This load can also be represented as a load resistance, R_L. Figure 8 represents a module attached to a load resistance. A switch that can be turned on or off is also represented.

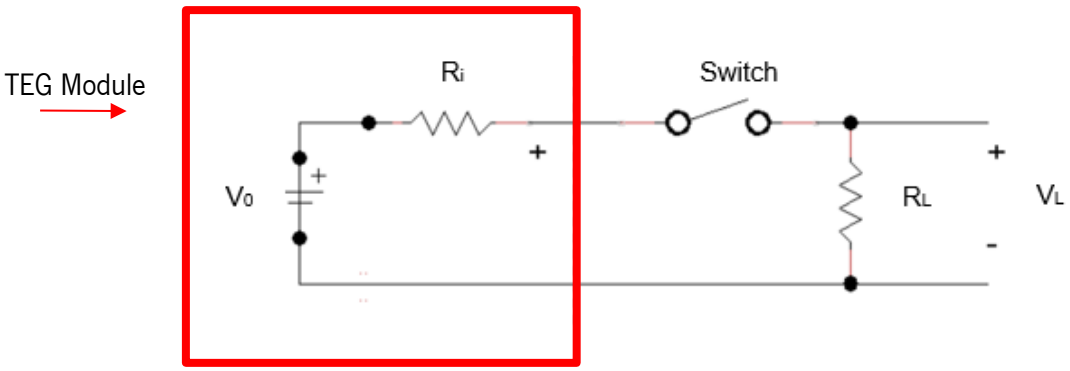

Figure 8 - TEG module electrical circuit

The internal electrical resistance of the module is the product of the number of p-n junction pairs, N, the sum of the resistance of the n-type (R_n) and p-type (R_p) thermoelectric elements, the contact resistance between the thermoelectric elements and the junction metal ($R_{contact}$) and the internal resistance of the junction metal (R_{metal}). These concepts are represented in Figure 9 and eq.(7).

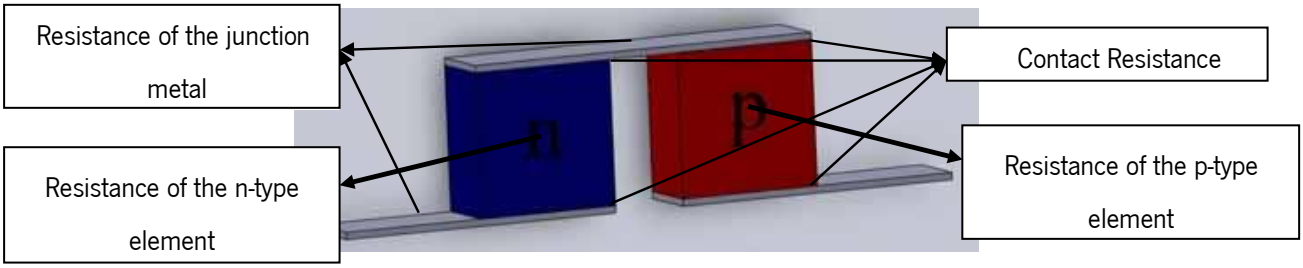

Figure 9 - SolidWorks illustration of a p-n junction pair [44].

$$R_i = N \cdot \left(R_n + R_p + 2 \cdot R_{metal} + 4 \cdot R_{contact}\right) \tag{7}$$

The internal resistance of p-type and n-type thermoelectric modules depends on the electric resistivity of the material (ρ), the length (l) and the section of the thermoelectric element (S) as follows:

$$R_n = \rho_n \cdot \frac{l}{S} \; ; \; R_p = \rho_p \cdot \frac{l}{S} \tag{8}$$

The metal resistance of the junctions is normally negligible. The contact resistance depends on the contact resistivity (ρ_{cnt}) and can be negligible if the contact cross section is large. The contact resistance (R_{cnt}) expression is as follows:

$$R_{cnt} = \frac{\rho_{cnt}}{S} \tag{9}$$

Using the law of meshes in the circuit shown in Figure 8, with the switch closed:

$$V_{Ri} + V_{Load} - V_i = 0 \tag{10}$$

Using Ohm's law:

$$V_{Ri} = R_i \cdot I \; ; \; I = \frac{V_{Load}}{R_{load}} \tag{11}$$

being the internal resistance:

$$R_i = \frac{R_{load}(V_0 - V_{Load})}{V_{Load}} \tag{12}$$

2.1.3 TEG Electrical Output

The Electrical power, *P*, in [W], is defined as the rate at which electrical energy flows, is absorbed or is released within a circuit or a system. Such relation can be found in Joule´s Law:

$$P = I^2 \cdot R_L \tag{13}$$

When the above-mentioned expression is combined with eq.(11), the expression for the TEG electrical power output results as follows:

$$P = \frac{V_L^2}{R_L} \tag{14}$$

2.1.4 Maximum Theoretical Power

The maximum theoretical power of a TEG would be obtained if the load resistance, R_L, would be equal to the internal resistance, R_i, of the TEG. Under these conditions, the voltage generated through the Seebeck effect would be dissipated internally and externally in equal parts, that is, the load voltage would be approximately equal to half of the open circuit voltage.

The Voltage inside the TEG module (V_o), has to be equal to the sum of the Voltages measured on the internal resistance (R_i) and the load resistance (R_L). Applying:

$$V_o = (R_i + R_L) \cdot I \tag{15}$$

Applying this equation to the max power formula (eq 5) one can get:

$$P_{max} = \frac{{V_o}^2}{4 \cdot R_i} = \frac{(R_i + R_L)^2 \cdot I^2}{4 \cdot R_i} \tag{16}$$

It is possible to simplify even more the expression using eq. (1). For that, given:

$$P_{max} = (R_i + R_L)^2 \cdot \frac{{V_L}^2}{4 \cdot R_i \cdot {R_L}^2} \tag{17}$$

So, applying eq. (14), It´s possible to reach a final expression to calculate the theoretical max power, given the power measured on the load resistance (P_L):

$$Pmax = \frac{(R_i + R_L)^2}{4 \cdot R_i \cdot R_L} \cdot P_L \tag{18}$$

2.1.5 Conversion Efficiency and Figure of Merit

One of the limitation of TEG modules has to do with their relatively low conversion efficiency from heat to electrical power, typically below 5%, for the temperatures ranges of exhaust heat recovery applications, although some positive evolution is being seen with the use of nanostructured materials and quantum confinement technologies [35][45]. The efficiency of a thermoelectric device for electric power production is stated as the relation between the electrical energy supplied to the load and the heat energy absorbed at the hot junction. It can be defined more precisely as the ratio between the generated electrical power (P_{TEG}) and the thermal power absorbed by the module Q_h. However, the thermal power released by the module to the cooling water circuit, Q_c, is easier to measure. Due to the conservation of energy principle, the difference between Q_h and Q_c will be equal to the electric power produced by the TEG, P_{TEG}:

$$\eta = \frac{P_{TEG}}{Q_h} = \frac{P_{TEG}}{Q_c + P_{TEG}} \tag{19}$$

To evaluate the thermal conversion efficiency to electric power in TEG material a dimensionless property defined as figure of merit (ZT), is used:

$$ZT = \frac{\alpha^2 kT}{\lambda_m} \tag{20}$$

where α is the Seebeck coefficient, k the electrical conductivity, λ_m the thermal conductivity of the material and T is the absolute temperature of the material.

The figure of merit is proportional to electrical power production. The higher the figure of merit of a TE material, the higher will be the electricity generation of a TE device. The maximum power efficiency (η_{max}) of a TEG module is given by eq. (21) [24]:

$$\eta_{max} = \frac{(1 - \frac{T_c}{T_h})}{2 - \frac{1}{2}(1 - \frac{T_c}{T_h}) + \frac{4\frac{T_c}{T_h}}{ZT\ T_c}} \tag{21}$$

where T_h and T_c refer to hot and cold face temperature respectively and ZT to the figure of merit. Figure 10 displays the values of ZT for common and emerging TE materials. Regarding commercially available materials, for lower temperatures (200 to 400 K) bismuth telluride (Bi_2Te_3) is recommended while for temperatures between 600 and 800 K the material lead telluride ($PbTe$) has the best figure of merit, although this material is slowly being abandoned for having the hazardous material lead. At higher temperatures (from 800 to 1300 K) silicon germanium ($SiGe$) is used, although its cost is fairly high, being an obstacle for widespread adoption [46] [47]. For all these materials and temperature ranges it holds that the maximum ZT is around 1.

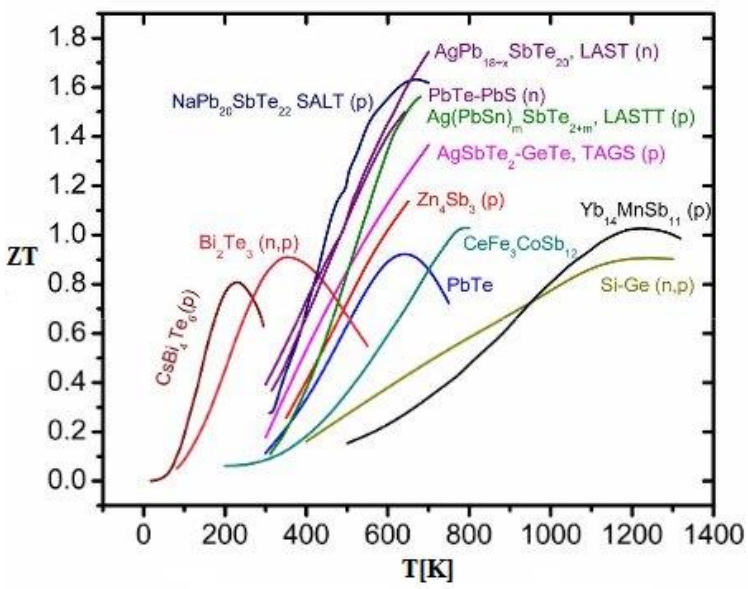

Figure 10 - Figure of merit ZT for common TE materials, as a function of temperature [46]

Furthermore, the contact thermal resistance between the hot and cold side of the TEG, can strongly influence the efficiency of TE module merit [48][49]. The conventional materials used in TEG applications, including Bi_2Te_3(bismuth telluride), $PbTe$ (lead telluride alloys) and $SI_{80}Ge_{20}$ (Silicon-Germanium alloys), have a maximum operation temperature around 320ºC, 630ºC, and 1020ºC, respectively [50] [51].

2.1.6 Module Maximum Allowed Temperature and Improvements

TEG module's output is very sensible to the thermal level. This happens because the module electrical power output is proportional to the square of the load voltage, V_L, (recall eq.(14)), which is itself proportional to the temperature, T, (recall eq.(1)). Therefore, the TE module's output is proportional to the square of the temperature difference across the thermoelectric elements [16]. It is justified to state that the best way to increase the Power output of the TEG modules is to maximize the temperature difference between the hot and cold face.

Ideally, the cold face temperature should be as close to ambient as possible, because of thermal efficiency. It would be beneficial to have a cold face as cold as possible with no energy expenditure to do so, if only it were possible. If the cooling system supplying the cold face works at ambient temperature, that temperature can never be reached, since:

$$Q = h \cdot A \cdot \Delta T \tag{22}$$

In order to have $\Delta T = 0$, the specific heat must be an Infinite value. Working on ambient temperatures a lower temperature on the cold side cannot be achieved.

On the other hand, the hot face, in direct contact with the exhaust heat in vehicle applications should be the highest possible and, simultaneously not surpass the TEG temperature limit. Unfortunately, most high temperature TE materials have high cost of manufacture or reliability challenges [32]. The evolution of the TE material innovations is shown in Figure 11.

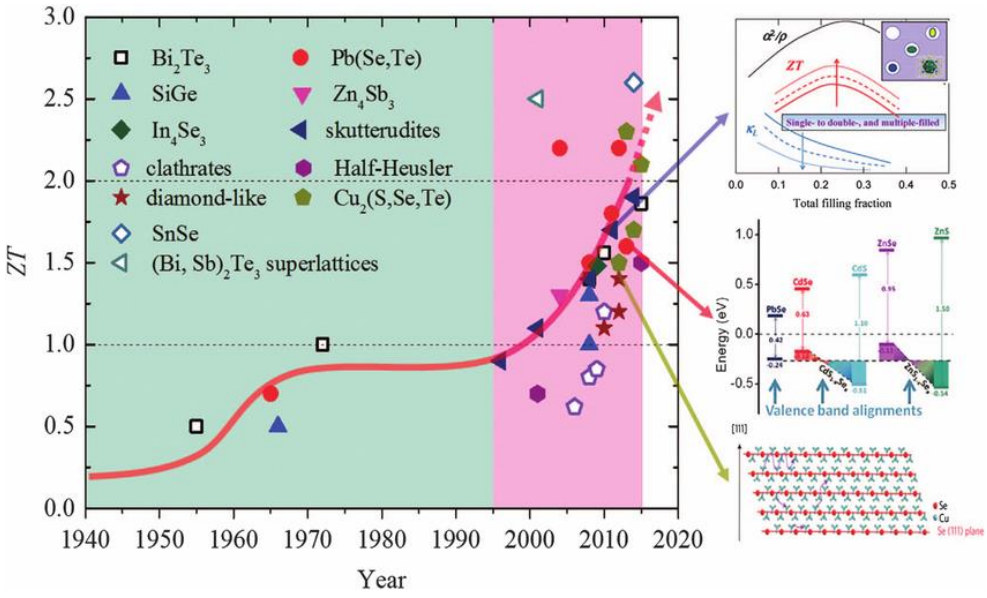

Figure 11 - Increase in the figure of merit of thermoelectric materials over the last years [52]

Commercial TEGs, despite having the capacity to hold, for short periods of time, spikes of 400°C, their maximum steady state temperature is typically 250°C. This value has more to do with the frailty of the soldering's rather than with the melting point of the alloy itself [30].

Juxtaposing, TE generators need to work close to their temperature limit and with a temperature as uniform as possible to be efficient [24]. On the other hand, if that temperature is exceeded, seizure ensues.

2.2 Thermodynamics

Thermodynamics is given as the science that studies the relationship between of heat and other forms of energy, encompassing electrical, potential and kinetic energy and their respective transformations [53]. Engineering thermodynamics traditionally covers the study of applications as diverse as the processes of refrigeration and air conditioning, expansion and compression of fluids and vehicle engines, expanding nowadays to the production of renewable energy and the use of temperature differentials for self-consumption of energy.

2.2.1 Basic Concepts

It is possible to understand thermodynamic phenomena using two different methods. The first one, called classical thermodynamics, is carried out without referring to the nature of the individual particles which constitute the substance, nor to their interactions. It is a macroscopic approach to thermodynamic phenomena. The second method, called statistical thermodynamics, is based on the behaviour of groups of individual particles. The latter has proved to be of great importance in new methods of energy conversion, such as Thermoelectrics [54]. There are 5 laws that describe thermodynamic phenomena, the first and the second one being the most relevant for studying engineering solutions for energy conversion and use and the zero law being related to thermodynamic properties. These three laws will be addressed in the following subchapters.

2.2.2 Zero law of Thermodynamics

Law zero of thermodynamics dictates that if a first body and a second body are in thermal equilibrium with a third body separately, then the first and second body are in thermal equilibrium with each other. This basic principle allowed temperature scales such as *Celsius* and *Fahrenheit* to be defined.

2.2.3 First law of Thermodynamics

The first law of thermodynamics introduces the concept of conservation of energy, which leads to the concept of internal energy of a substance.

According to the principle of conservation of energy, energy cannot be created or eliminated, only transformed. This principle makes the creation of a perpetual motion machine impossible. Thus a change in the energy of a body or system is equal to the difference between the final and initial instants [53]. It can be expressed:

$$E_{Final} - E_{Initial} = \Delta E \tag{23}$$

In addition, this law establishes a relationship between work (W) and heat (Q) exchanged between the system and its external environment. Given an isolated system in which a certain quantity of heat (Q) crosses the boundary and considering that the boundary moves, implying energy exchanged in the form of work, the variation of the internal energy ΔU is expressed as follows [54]:

$$\Delta U = Q - W \tag{24}$$

It should be noted that if Q is positive the system is receiving heat and when Q is negative the system is giving off heat to the outside. The opposite happens with work: when W is positive, it is performing work, so the energy is being supplied from the system to its surroundings. If W is negative the reverse applies.

2.2.4 Second law of Thermodynamics

In the analysis of real case studies, the first rule of Thermodynamics is not enough to determine the direction of processes as for example the heat transfer in which the heat always flows from the hottest body to the coldest. That is why it is necessary that real processes satisfy the second law of thermodynamics. Work can be more valuable than heat transfer when it comes to energy transfer. Work can be transformed 100% into heat whereas the opposite is not possible. The second law of thermodynamics also shows that the higher the temperature in the medium where the heat transfer takes place, the more heat transferred can be converted into useful work. It should be noted that systems with lower temperatures have "degraded" energy.

This law also expresses that the entropy of an isolated system tends to increase with time until it reaches a maximum value [55]. That is, when a closed system interacts with another system, the energy is divided equally, until the system reaches thermal equilibrium [54]. Since no useful work can be extracted from a system in thermal equilibrium, a thermal machine can only function if there is a temperature difference.

2.2.5 Heat Transfer Concepts

Heat transfer mainly studies energy in heat form since it is the energy that can be transferred from one system to another through a temperature differential.

Conduction, convection and radiation (the last not being considered in this dissertation), are the three basic mechanisms of heat transfer. Both require a temperature difference and occur from the highest temperature level to the lowest. Heat transfer ceases when both systems reach the same temperature (thermal equilibrium).

Conduction is the transfer of energy, which occurs by diffusion of the kinetic energy of particles within a medium. The particles atoms interact with each other but tend to remain roughly in the same physical position, except for gases, where molecular diffusion also plays a part in conductive heat transfer. The expression of conduction expresses as follows:

$$\dot{Q}_{conduction} = \lambda \cdot A \cdot \frac{T_1 - T_2}{\Delta x} \tag{25}$$

$\dot{Q}_{conduction} - \ heat\ conduction\ rate\ [W]$

$\lambda - \ thermal\ conductivity\ [W/m \cdot k]$

$A - \ area\ [m^2]$

$\Delta x - \ thickness\ [m]$

The heat conduction rate, $\dot{Q}_{conduction}$, across a plane wall with area, A and thickness Δ_x, depends on the thermal conductivity of the material, λ [W/m·K], the transfer area, A [m²], the temperature differential between two outer surfaces and the thickness, $\frac{T_1 - T_2}{\Delta x}$ (see Figure 12).

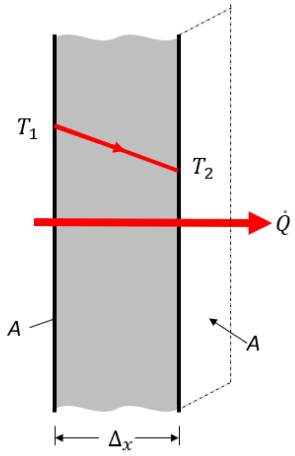

Figure 12 - Heat conduction along a body with thickness Δx and area A.

Convection is the heat transfer between a wall and a fluid flow. It occurs in liquids and gases and combines conduction and fluid motion. In this particular case, heat transfer occurs by conduction, that is, by microscopic interactions between contiguous molecules (molecular diffusion) but also by the macroscopic movement and mixing of the fluid that induces the transport of heat. The faster the movement of the fluid relatively to the wall, the greater will be the heat transfer by convection. The convective heat transfer rate is calculated through the convective heat transfer coefficient of the flow, *h* [$W/m^2 \cdot K$] (which is normally obtained from empirical correlations suitable for the specific case), the heat transfer area, and in this case on the temperature difference between the bulk temperature of the flow and the wall, T_f and T_w.

$$Q_{convection} = \mathrm{h} \cdot A_c \cdot (T_f - T_w) \tag{26}$$

Radiation heat transfer is related to the energy that is emitted by matter in the form of photons or electromagnetic waves. This heat transfer mechanism will not be further explored in this work.

Thermal Inertia

Thermal inertia is a property of materials, related to the ability of materials to maintain stored thermal energy over time. It can be defined as the property of a material that expresses the degree of slowness with which its temperature reaches that of the environment [56].

Thus, a material with high thermal inertia will take longer to reach an equilibrium state but is also able to store the accumulated thermal energy for a longer time. It can be defined as follows [57]:

$$I = \sqrt{\lambda \rho C} \tag{27}$$

Where:

$I - Thermal\ Inertia\ [J \cdot m^{-2} \cdot K^{-1} \cdot s^{-1/2}]$

$\lambda - thermal\ conductivity\ [W/m \cdot K]$

$\rho - density\ [kg \cdot m^{-3}]$

$c - specific\ heat\ capacity\ [J \cdot kg^{-1} \cdot K^{-1}]$

2.2.6 Heat Exchanger Basic Concepts

Absorbed Thermal Power

The general equation for describing thermal energy transfer in the absence of phase change is:

$$Q = m \cdot c_p \cdot \Delta T \tag{28}$$

Where:

Q – thermal energy [J]

m – mass of a substance [kg]

c_p – specific heat [J/kg · K]

ΔT – temperature diferential (^{0}C)

It expresses the heat necessary to raise the temperature of a body of mass m by a certain ΔT over a period of time. It is a relevant parameter in transient heat transfer. In the present study, this is relevant in order to quantify the portion of the heat absorbed by the TCTG and not transmitted to the TEG modules. This expression can be adapted for energy flows. The heat transfer rate, $\dot{Q}$, from/to the exhaust/cooling stream to/from the TCTG will be proportional to the temperature decrease/increase between the inlet and the outlet. It is expressed in terms of Power [W]:

$$\dot{Q} = \dot{V} \cdot \rho \cdot c_p \cdot \Delta T \tag{29}$$

Where:

$\dot{Q}$ – heat transfer rate [W]

$\dot{V}$ – volumetric flow rate [m^3/s]

ρ – density [kg/m^3]

c_p – specific heat [J/kg · K]

ΔT – temperature diferential [^{0}C]

Heat Exchanger Effectiveness:

The effectiveness of a heat exchanger is a concept that is slightly different from thermal efficiency. It represents the ratio between the heat effectively absorbed by the HX and the available heat, that is, the maximum heat that could be absorbed in an ideal scenario. From eq. (29) this yields:

$$\in = \frac{\dot{Q}_{exh\ absorbed}}{\dot{Q}_{\text{exh available}}} = \frac{T_{exh\ in} - T_{exh\ out}}{T_{exh\ in} - T_{water\ in}} \quad (30)$$

2.3 Heat Pipes (HPs) and Variable Conductance Heat Pipes (VCHPs)

As mentioned before, to produce as much energy output as possible TEGs need to maximize the temperature differential, but the modules should have a hot face with a temperature close to the maximum operating temperature, 250°C.

A solution for passively avoid TEG overheating at high thermal load while simultaneously providing efficient operation even at low loads could stand on a system capable of maintaining the desired operating temperature regardless of the exhaust gas regime, by automatically adjusting the heat flow reaching the TEGs. This could be achieved using Heat Pipes (HPs) with adjustable saturation temperature, such as the Variable Conductance Heat Pipes (VCHP). This solution allows constant phase change temperature (saturation temperature) which can be manipulated through pressure. This solution allows maximizing the thermal efficiency for variable thermal load conditions because the temperature will be prevented from going beyond the maximum allowable value.

2.3.1 Historical Development

The principle of the heat pipe was first put forward in 1942 by Richard S. Gaugler of the General Motors Corporation in the U.S. Patent No. 2350348 [58]. The advantage of using heat pipe over other conventional methods is that large quantities of heat can be transported through a small cross-sectional area over a considerable distance with no additional power input to the system [59]. Gaugler designed a device that consisted of a closed tube in which a liquid would absorb heat and evaporate, travelling to other end where it would condensate releasing its latent heat and then travel back due to capillary pressure, restarting the cycle. The capillary phenomena seen in the HP working principle allows them to work on microgravitational environments with any external form. This led to its development being firstly aligned with space applications. Eventually energy cost problems and energy saving policies in Europe and Asian countries led to overwhelming development of HP technology in the last two decades. As today, there are HP applications all over the world, in the most diverse areas, from micro and miniature heat pipes, loop heat pipes over to pulsating heat pipes [59]. Likewise, a significant amount of based and applied research and development has been made by the scientific community with a large number of publications, reports and books being published since the 1990´s [60] [61].

2.3.2 Principle of Operation

Whereas HPs can be of any shape and size, the cylindrical geometry of the heat pipe is the one best suited to understand how they work. A schematic representation of a conventional cylindrical heat pipe is presented in Figure 13. The three main components of a heat pipe, as described in [59], are a sealed tube (container), a wick structure and a working fluid that is in equilibrium with its own steam.

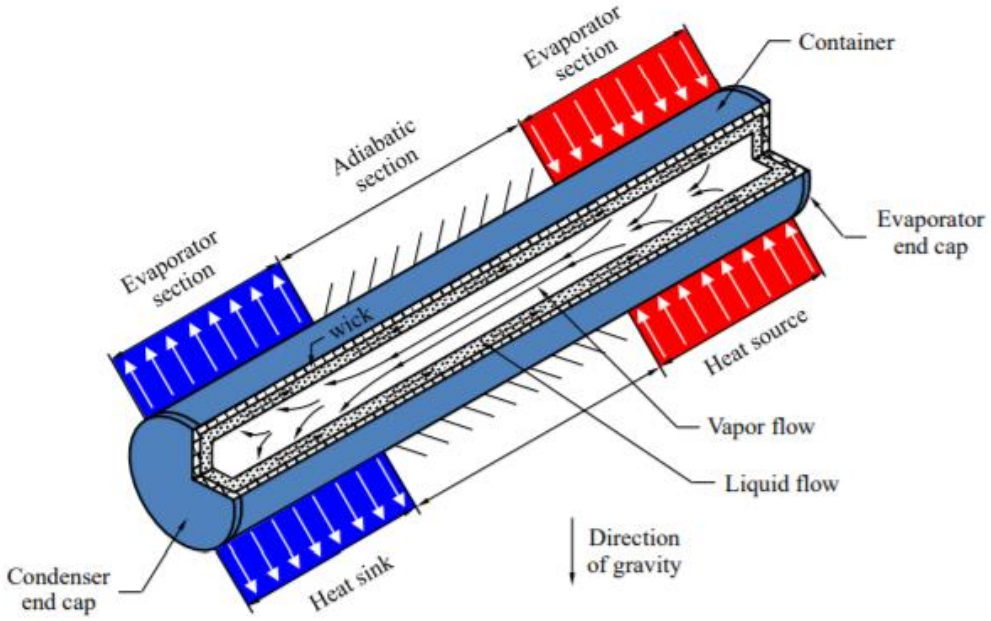

Figure 13 - Conventional heat pipe schematic view [61]

The working fluid can vary, depending on the saturation temperature range of use to which they are designed sized, ranging from acetone, ammonia, and sodium, the most commonly used being water.
The conventional heat pipe is essentially divided into three operating sections: the evaporator section, adiabatic (transport) section and condenser section. It should be noted that depending on the type and application of the heat pipe, the number of heat sources may vary as well as the existence or not of an adiabatic transport zone.
The principle of operation of the HP is as follows: An external heat source is applied to one end of the pipe and heat is transferred by conduction through the pipe wall and the wick structure (metallic porous medium that absorbs liquids due to capillary forces similarly to a sponge) to the working fluid. The fluid vaporizes causing the pressure inside the pipe to drive it through the adiabatic section to the opposite end (condenser section). The different regions of the HP can be seen in Figure 14.

(a)

(b)

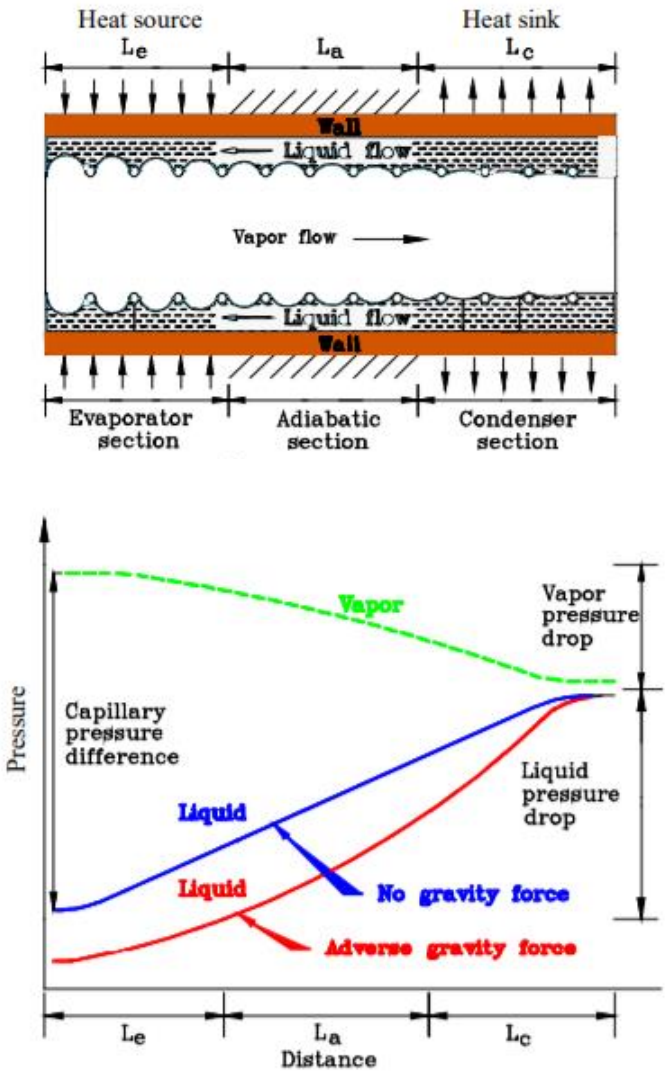

Figure 14 – Heat Pipe (a) sections and (b) fluid behaviour inside the pipe [61].

In the condenser section, due to a lower temperature on the outside related to the absence of a hot source, the steam condenses releasing the latent heat of condensation.

To understand the phenomenon of fluid return through the Wick capillary it is necessary to understand that the menisci that translate the liquid-vapour boundary have a curved shape in the evaporator area and are flatter in the condenser area (see Figure 14). A capillary pressure resulting from the surface tension of the working fluid and the curved structure of the interface exists and varies in different sections of the heat pipe due to differences in the curved geometry of the menisci. This capillary pressure causes the fluid to circulate in the opposite direction to the pressure losses of the liquid and vapour and against the adverse forces of gravity.

This process will continue if there is sufficient capillary pressure to move the working fluid back to the evaporator zone. Although gravity tend have a preponderant role in the mechanism, it is not strictly

necessary as, due to capillary action, heat pipes can operate in microgravitational fields without any external force field or pump. Also, horizontal applications can be found with significant efficiency [61].

2.3.3 Working Fluid and Temperature Ranges

The function of the working fluid within the heat pipe is to absorb the heat energy received at the evaporator section, transport it through the pipe and release this energy at the condenser end. Nevertheless, the HP only starts to transfer heat from the hot source to the heat sink once the boiling temperature of the fluid has been achieved (with the exception of the conventional heat pipe (see 2.3.4)) [27].

There is a range of fluids that can be used as condensable fluids and the choice will always rest on their specific application. A good working fluid will require a high thermal conductivity, high latent heat, and surface tension. The design of the HP must consider the temperature range in which it will work and its corresponding pressure range, specifying which fluid should be used, considering that it will be expected to vaporise and condense during the operation of the HP. Table 1 lists some of the vaporization and condensing temperatures of commonly used working fluids.

Table 1 -Working fluids and temperature ranges of heat pipes [61]

Working Fluid	Melting Point @ °C at 1atm	Boiling Point @ °C at 1atm	Useful Range @ °C at 1atm	
Helium	-272	-268	-271	-269
Hydrogen	-259	-268	-259	-242
Nitrogen	-210	-246	-246	-236
Argon	-189	-185	-203	-170
Oxygen	-218	-218	-189	-157
Ammonia	-77.6	-182	-200	-154
Ethanol	-114	78	-60	100
Water	0	100	30	232
Dowtherm-A	12	253	30	277
Cesium	28	669	150	395
Lithium	180	1341	450	900
Silver	960	2211	1000	1800

The use of water as a working fluid seems to be the most appropriate, being the ideal heat transfer fluid, since no other has such good thermal properties in this temperature range (0-232 °C). However, the useful range of temperature reported in this table does not reach the TEG modules hot-face temperature of interest (250 °C). In reality, it is possible to use water with vaporization temperatures of around 260°C if a system that can withstand the corresponding pressure (~50 bar) is available, which is the case of one of the prototypes described in this work. Dowtherm-A also seems to be a good alternative for lower pressure systems (at atmospheric pressure).

2.3.4 Types of Heat Pipes

There are several types of heat pipes, varying in shape, function, and dimensions. Since their creation until the date of writing this document, HPs have been constructed from 19 mm to 100 metres in length. Varying also in diameter, with some having a diameter as small as 80 μm [59]. Despite their outstanding differences, the common characteristic of these devices is to have an evaporator and a condenser, where the condensable fluid vaporises and condenses, respectively. The number of evaporators and condensers can vary as well as the force used to return the liquid from the condenser back to the evaporator, which is usually the capillary force but can also be centrifugal, gravitational, or electrostatic force. For construction reasons the most common shape in the market is the cylindrical shape HPs, however other shapes such as rectangular (flat heat pipes or vapor chambers), conical (rotating heat pipes, corrugated flexible heat pipes and nosecap (leading edge heat pipes) geometries have been used [62].

The type of heat pipe described next in detail is the Variable Conductance Heat Pipe (VCHP) since it is the one used by the research group in the construction of the heat exchanger prototype for exhaust gas recovery.

Variable Conductance Heat Pipe (VCHP)

In a conventional heat pipe, the working fluid is always under saturation conditions, therefore, vaporization temperature of the working fluid varies according to the heat source and the characteristics of the working fluid employed. For the latter, although the conductance value is fairly high, it is almost a constant parameter. However, in some applications it may be necessary to maintain a stable vaporization temperature with a variable heat source.

In a VCHP, as it incorporates a NCG, it is possible to regulate the temperature at which the working fluid starts changing phase. The variable conductance then is present in the sense that the condenser heat

transfer area will vary according to the thermal load, as shown in Figure 15. If it is low, only a portion of the condenser will be filled with vapour, with the rest being filled with NCG and thus being inactive. As thermal load increases, a higher fraction of the condenser will be occupied by vapour and thus the heat transfer will increase (higher heat transfer area). In a constant conductance (CC) device the variation of the thermal load causes a variation of the temperature of the HP with the heat transfer area being constant. In a Variable Conductance (VC) device the opposite occurs: the HP temperature is fairly constant, but the active heat transfer area varies.

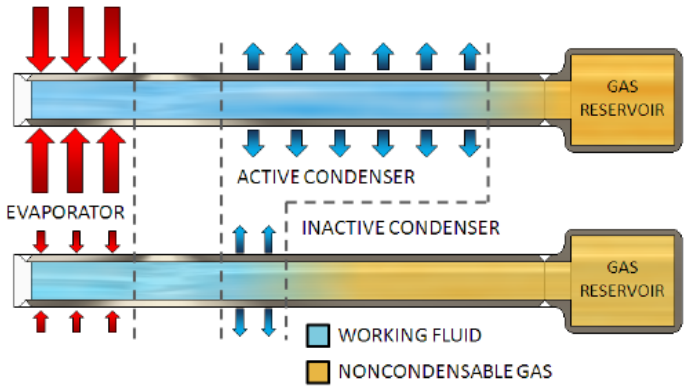

Figure 15 - Outline of a Variable Conductance Heat Pipe operation [63].

To understand this phenomenon, eq. (31) presents the simplified model of heat transfer in a HP, where the thermal resistance between the heat source and the vapor is represented by R_e, the total axial resistance along the heat pipe is R_v and the total thermal resistance from the vapor in the condenser to the heat sink is R_c. The overall resistance of the heat pipe, R_t, can be written as:

$$R_t = R_e + R_v + R_c \tag{31}$$

and the total value of conductance in a heat pipe is:

$$C_t = \frac{1}{R_t} \tag{32}$$

The conductance value can be altered by changing any of these parameters. Variable Conductance Heat Pipe, or Gas-Loaded heat pipe have a condensable fluid and non-condensable fluid which results in two distinct operating regions the VCHP's (Figure 16).

The active region is the isothermal region where there is vaporization and condensation of the condensable fluid, and the passive region is adiabatic region filled with non-condensable fluid. The mixture between the condensable and non-condensable fluid is rather small on behalf of occupying different parts of the VCHP. The greater the thermal power transmitted by the heat source, the bigger the volume of VCHP occupied by steam. The ideal scenario translates on one in that the VCHP is filled with steam, as this means the largest region active as possible. The VCHP also includes an expansion tank that has the purpose of accumulating the non-condensable fluid that is pushed by the vaporization of the condensable fluid. This expansion helps maintain constant pressure inside the tube.

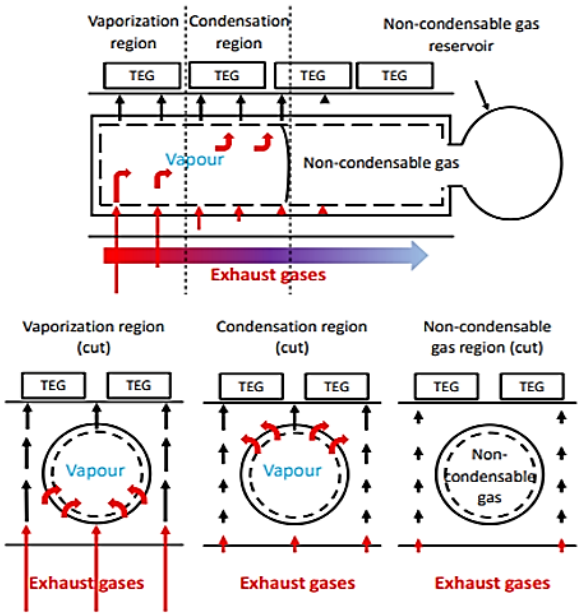

Figure 16 - Variable Conduction Heat Pipes Working Principle [38]

The expression translating the heat transfer from the condenser of an conventional HP can be written as follows, resulting from eq. (26) [61]:

$$Q = h \cdot S \cdot (T_w - T_\infty) \tag{33}$$

Where Q is the total heat transfer, h is convective heat transfer, S is the outside surface area of the condenser, T_w is the average wall temperature in the condenser section and T_∞ is the ambient temperature. If, in a conventional HP, the temperature of the heat source increases with a constant T_∞, S and h the wall temperature, T_w, must increase correspondingly. However, in a VCHP the cross-

sectional area of the condenser varies with the compression of the non-condensable gas so that if the heat source increases the wall temperature can remain relatively constant [59].

2.3.5 Pressure Variation and Influence

The boiling temperature of the working fluid inside the VCHP will be a function of the saturation conditions inside the pipe, mainly the inner pressure. If the inner pressure of this device can be controlled, then the heat transfer temperature can also be controlled [34]. This will allow a precise temperature control of the heat source for most of the heat source load range. The preloading pressure of the non-condensable gas will determine the operating pressure of the VCHP.

As the heat input increases, the total pressure increases. However, because the total pressure is comprised of both the partial vapor and partial gas pressures, the increase in total pressure is accounted for by an increase in the partial gas pressure, maintaining a constant vapor pressure, and thus a constant vapor temperature [61].

However, if the vapour production in the evaporator is such that the HP is completely active, pressing the non-condensable gas to the condenser end, then it will work at constant volume (typical operation of a conventional HP). In this situation the temperature and pressure inside the heat pipe will increase, so that the thermal control expected at the beginning is not achieved.

One of the solutions used by the LaMoTA research group to this problem is the implementation of an expansion vessel after the condenser section that implements a significant increase in the VCHP volume. This allows the process to occur at a fairly constant pressure irrespective of the exhaust temperature and flow rate [34]. The expansion tank will allow the inner pressure (and thus the boiling temperature point) to remain nearly the same, irrespective of the exhaust temperature and flow rate.

2.4 State of The Art of Automotive Thermo-Electrical Generators

In this chapter the main developments made in vehicle-oriented TEG's implementations technologies for exhaust gas heat recovery are described. Also, the research carried out by the LaMoTA research group in this area is presented up to its latest achievements.

After the second world war thermoelectricity was widely studied for various technological applications, such as cooling and power generation. World interest on thermoelectric lead the research to grow rapidly in universities and research laboratories [64]–[66].

The first tests of thermoelectric generation applied to vehicle waste heat recovery were reported in the 1960s with Neild [67]. Other works used modified car engines aimed to test TEG applications on road vehicles, e.g. in 1988 [68] published the results of a collaboration with Porsche, applying TEGs technology to exhaust heat recovery in a Porsche 944, using a carbon steel hot side and aluminium cold side heat exchanger was able to produce 58 W under peak conditions with $FeSi_2$ elements.

Hi-Z Technology Inc. started a program to build and test a 1 kW thermo-electric generator for Diesel engines in 1987 as part of the U.S. Department of Energy's (DOE). This program began to design and build a 200 W thermoelectric for Diesel engines which was reported [69] at the 1991 Conference in Cardiff, Wales. In a second phase of this programme, aiming to achieve 1 kW of electrical power produced, a thermoelectric generator was implemented for testing in a MACK truck engine [70] [71]. This generator consisted of 8 faces with 9 TEGs each. However, in initial tests using a *14 Litre Cummins NTC275* engine, only 400 W were generated. The low power output results were due to the inexistence of a turbulent flow in the exhaust gas [70]. The solution was found by using a heat exchanger with a conic shape and a second test using a *14 litre Cummins NTC335 engine* had the highest electric power output from the TEG of over 900 W (recorded at engine load of 290 hp). The 1 kW goal was achieved after a series of optimizations using a *14 litre Cummins NTC350* engine at 1700 rpm and producing 300 hp (Figure 17).

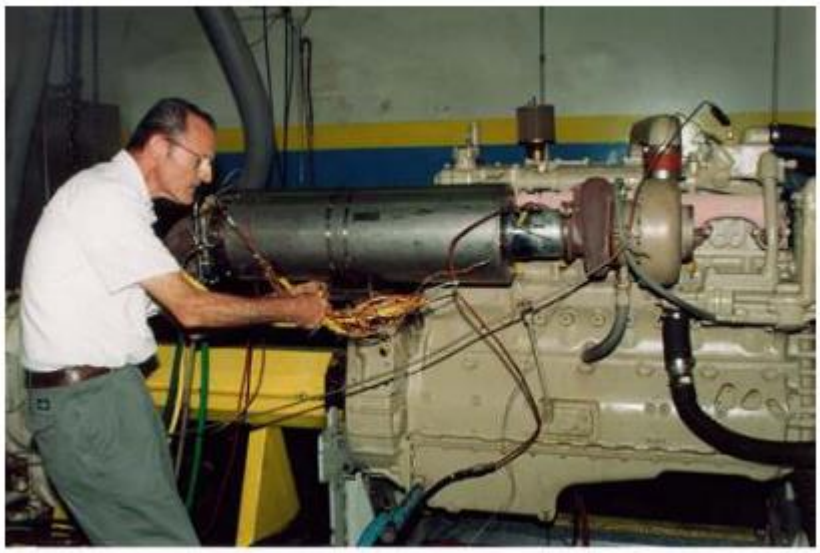

Figure 17 - 1 kW Generator Mounted on Cummins NTC350 Engine [70].

TEG power was found to be strongly dependent on engine load and less so on engine speed, as illustrated in Figure 18 and in line with the data reported in [72]. The test engine and the power bench did not allow the nominal load to be reached that limited power production by TEG. The results with with the *NTC335* and the *NTC350* are presented in Figure 18.

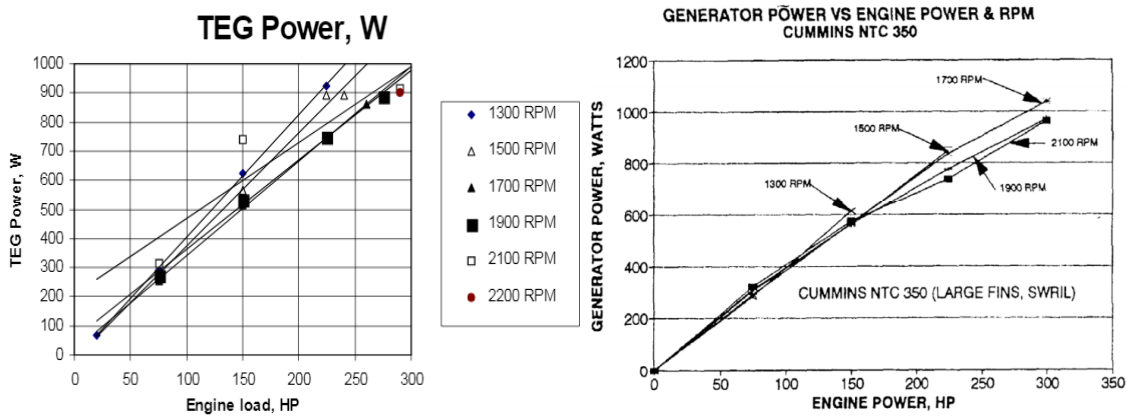

(a) (b)

Figure 18 - TEG power output as a function of the engine load and engine speed in tests with a) NTC335 engine and b) NTC350 engine [73][74].

Some mechanical problems were detected during the vehicle performance testing phase and new experimental procedures were carried out with new TEGs modules (HZ-14) applied on a 550 hp diesel engine (see Figure 19) with the intention of completing durability tests, where 873000 km were complete successfully [73].

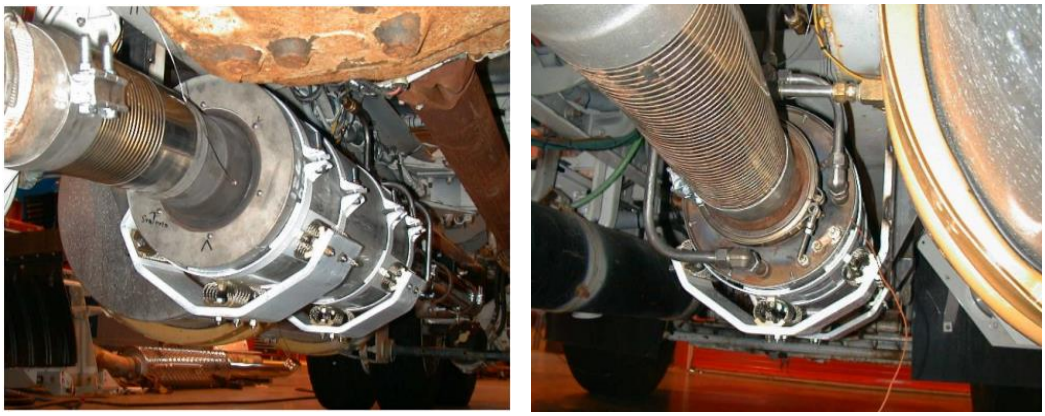

(a) (b)

Figure 19 – (a), (b) 1kw Thermoelectric generator installed in a 550hp diesel engine [71].

In the following years, the thermoelectric generator was modified to adapt a Hybrid SUV to generate 180W of electricity and with the capacity to charge 300V batteries (Figure 21a).

In 1998, the Nissan Research Centre from Japan [75] developed a TE generator with a rectangular cross-section of 72 modules (see Figure 20). Each one of these modules contained eight pairs of Si-Ge elements with a ZT of 0.6 to be applied in gasoline-powered vehicles. Cold water was used for the cold plates to provide a heat sink for the TEGs to generate electric power. The electrical power supplied by the generator was 35.6 W using a 3000 cc petrol engine under a 60 km/h in a hill climb. The power output ratio to the total volume of the TEG was 5.6 W/m^3, and the ratio of the total electric power to area of the hot sides of all modules was 1.2 kW/m^2 [76][77].

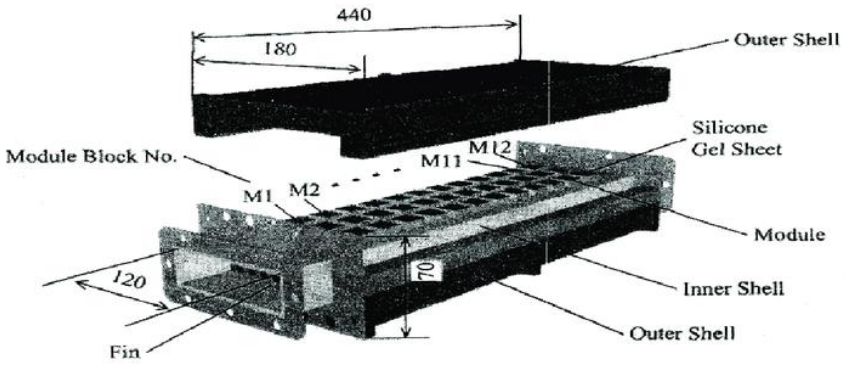

Figure 20 - Nissan´s 1998 TEG Prototype [76].

Again in 1999, *Hi-Z Technology* in collaboration with the *Clarkson University, General Motors* and *Delphi Corporation* began the study to build and test a thermoelectric generator to generate 300W with a system capable of charging 12 and 24 V batteries to power the lights and other on-board devices on a *GM Sierra Pickup* with a V8 220 hp diesel engine [78][79].

The HE and TEGs are shown in Figure 21b and the results presented a power output of 255W (of the expect 300 W) with an average coolant temperature of 25°C.

(a) (b)

Figure 21 - a) 180 W thermoelectric generator for Hybrid SUV and b) 330 W for Jeep Sierra Pickup from General Motors [94].

In 2005 BMW and other organisations published at the DEER Conference (Directions in Engine-Efficiency and Emissions Research) the results of a study to implement a thermoelectric exhaust gas generator on a BMW 5 Series (petrol, Inline 6 cylinder, 3.0 L and 254 hp) capable of producing 500 W with a temperature difference between 250°C and 390°C [60][70][80] (see Figure 22). One of the goals of this project was to achieve a 10% improvement in fuel economy but no reports were found stating the final conclusions of the project.

(a) (b)

Figure 22 – (a), (b) TEG Installed in a BMW 530i [82] [83].

In 2008 Volkswagen presented the results of its first implementation of a heat exchanger with thermoelectric generators at the *Thermoelektrik-Eine Chance Fur Die Atomobillindustrie* with an output of about 600W, announcing a filling of the electric needs of the car by 30% and a saving of 5% in fuel through the load relief of the alternator [81].

Figure 23 - Exhaust TEG system presented by WV in 2008 [81].

In 2014 GMZ presented the results of the study of its 1 kW heat exchanger connected to a 15 L V8 diesel engine [82], [83]. This exchanger consists of a junction of five TEGs of 200 W each, incorporating *GMZ's TG8-1.0* TE modules, capable of operating at temperatures of up to 600°C.

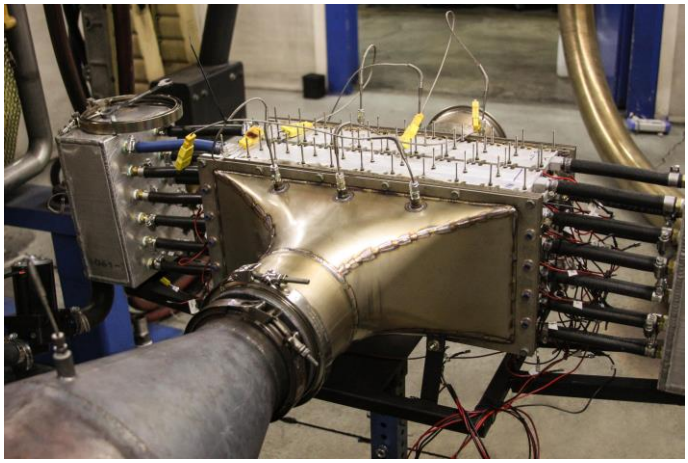

Figure 24 - GMZ's 1KW Exhaust Heat TEG [74].

Despite the constant innovations in the area of heat exchangers and materials of thermoelectric modules, the figure of merit of the materials, ZT, is still a barrier to overcome in order to enhance applications of this type of technology in the automotive industry. Some theoretical predictions were made and later experimentally validated [84] of the increased performance of thermoelectric modules using nanostructured materials.

In summary, new prototypes of thermoelectric modules have been studied and have considerable advances in this area. However, the non-implementation of these technologies in vehicle exhaust gas recovery today can be blamed on the thermal stability that these materials require, design of heat exchangers with low effectiveness, production costs and development [24]. Currently one of the biggest constraints for these systems is the difficulty to achieve average efficiencies that may be closer to their theoretical maximum efficiency. This is due to the difficulty of achieving an optimal temperature level in the modules that operate under the highly variable thermal loads that are present in realistic driving cycles. Having a thermal control strategy enabling the modules to operate always near their optimal temperature (which is their maximum temperature) without the risk of overheating and with a high HX effectiveness could finally enable the viability of automotive TEGs. The concept assessed in the present study aims at these objectives.

3. EXISTING PROTOTYPE AND MODIFICATIONS

For this work, a concept prototype modelled and numerically simulated by LaMoTA group was used as a base to build a downsized proof-of-concept prototype within Project Exhaust2Energy to be tested with an engine. The design and numerical assessment performed on this concept are described in [36].

This chapter describes the initial construction of the prototype presented in Figure 25, carried out by the LaMoTA research group, as well as the problems arising from this construction process that influence the types of tests performed and the finalization phase of this construction that was part of the work performed in the scope of this thesis.

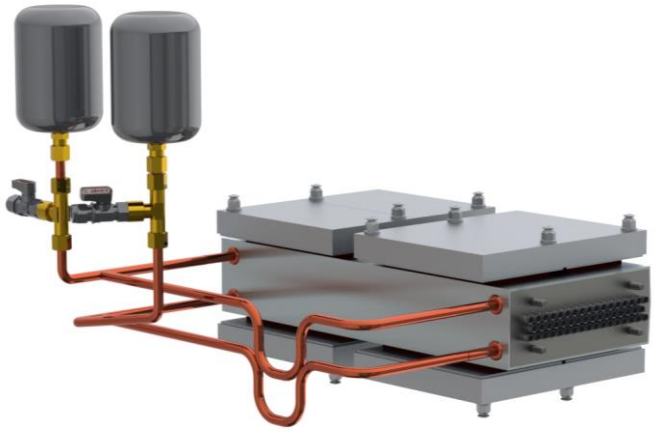

Figure 25 - TCTG Prototype concept.

3.1 TCTG Prototype Concept

Based on the operating principles explained in chapter 2 regarding TEGs, excess heat spreading and VCHPs, a novel conceptual prototype design was proposed, as seen in Figure 26. Figure 26a displays the built and tested TEG generator concept design. The prototype tested is a partial version of the proposed final system, being one quarter of the full system (recall Figure 4).

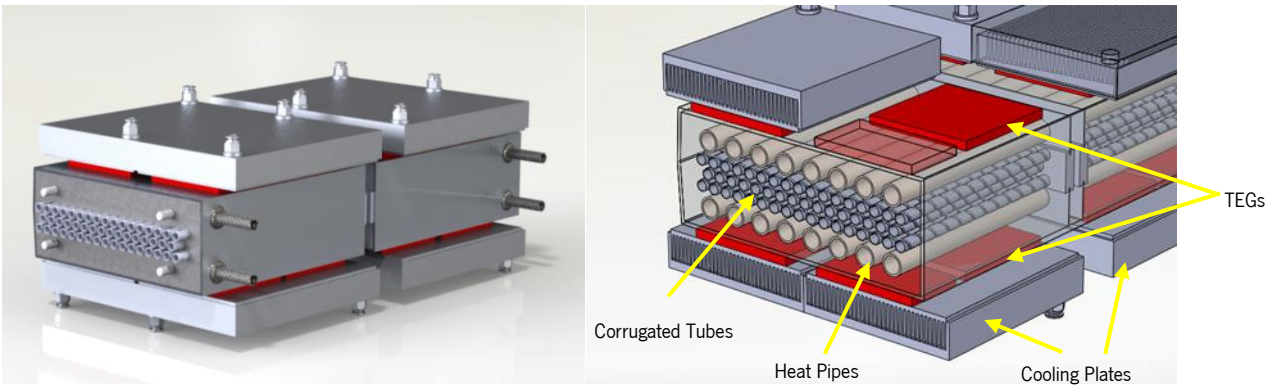

(a) (b)

Figure 26 - a) Full TEG generator concept; (b) Section View of the corrugated tubes and VCHPs embedded in an aluminum matrix, along with the TEGs (red) and cooling plates.

Figure 26b shows a cross section view of the prototype in which it is possible to distinguish the corrugated tubes at the center, within which the exhaust gases flow. Two horizontally disposed batteries of VCHPs are positioned parallel to the exhaust flow, between the corrugated pipes and the upper and lower sets of TEG modules. These VCHPs are made of copper, incorporating an inner wick of porous copper aimed at promoting capillary pumping of the condensed fluid returning to the vaporization region. Both the corrugated pipes and the VCHPs are embedded in within a die-cast aluminum matrix that ensures a low thermal resistance heat path from the exhaust gases to the modules and allows structural stability during operation. The hot faces of the TEGs are in direct contact with the top and bottom surfaces of the cast aluminum matrix, while the cold faces of the TEGs are attached to the cooling plates, through which water flows as coolant in a controlled water circulating circuit. The CAD drawing represented in Figure 26a represents the size of the experimental prototype built and tested in the present study, that is presented later in this work. It comprises a total of 16 TEGs (8 below + 8 above).

The working principle of this novel TCTG (recall Figure 3) is as follows: the HPs inner pressure is set to value that the condensable fluid only starts to vaporize on a controlled temperature set to optimize the system efficiency. In this case, the optimal temperature will be the TEG's modules maximum working temperature (250°C), in which case they only start to vaporize and transfer heat to next upstream thermo-exchange zone whenever reaches the temperature limit of the modules. Then, when engine is running the exhaust gases dissipate heat while running through the corrugated pipes to transfer heat to the TEG's hot face as desired. The heat dissipated by exhaust gases at an early stage, arrives by conduction to the TEG's, however when the point of saturation of the fluid inside the VCHP is reached (dependent to the pressure set initially), condensable fluid starts to evaporate and subsequent condensation allowing the

phenomenon of heat dissipation along the exchanger. Based on this description, it is possible to identify 3 operating regimes:

Low thermal power operation: the temperature is lower than the fluid saturation temperature inside the VCHPs, so they are inactive throughout their length. In this scenario heat travels by conduction through the aluminum matrix to the TEG's. Under these conditions, the VCHPs are filled only with the NCG and are approximately adiabatic.

Average thermal power operation: there is a region in the vicinity of VCHPs where there is enough thermal power to raise the temperature above saturation conditions. This causes local fluid vaporization inside the VCHP, which absorbs heat from the aluminium matrix. A portion of the VCHP will thus be filled with vapour. This vapour will condense at the colder regions reached by vapour (recall Figure 3). However, there is not enough thermal power to fill the VCHP with vapour, so it works in a mixed state and VCHP are only partially active. In zones where it is active, there is still a component of the heat that is transmitted by conduction, but VCHPs absorb energy by vaporization (hotter regions) and release energy by condensation (colder regions). In the regions where it is inactive (with NCG only) energy is transmitted exclusively by conduction through of the aluminium matrix.

High thermal power operation: the thermal power is such that the VCHP is filled by vapour along its entire length - the VCHP is fully active. In this case, the non-condensable gas is pushed out of the module region and into the expansion tanks.

It is important to remember that maximum energy production is achieved when all TEG modules are active at maximum operating temperature, 250°C. For this reason, the increase in thermal power source only causes to have more active modules and not increase the TEG's hot face temperature. Meaningfully for electric energy production in TEG's is the differential of temperature between the cold face and the hot face so it is vitally important to cool down effectively the opposite face of the TEG's. For this purpose, at the opposite side there are the cooling plates, through which a coolant (in this case water) flows driven by a pump. In a real-life application this fluid would have to be cooled through a radiator, and use a fluid such as antifreeze engine cooling fluid, to prevent system incapacitation during cold scenarios.

Regarding the location of the TCTG, it should be placed directly after the catalyst aiming to minimize energy losses due to heat dissipation. Another interesting way to reduce heat dissipation losses would be the exhaust pipe insulation.

Regarding the use of stainless-steel corrugated exhaust pipes (see Figure 27), these seem quite convenient as they are used extensively in exhaust applications such as Exhaust Gas Recirculation (EGR) coolers. They can be easily embedded within cast aluminium with good thermal continuity. Moreover,

their geometry is able to provide a good degree of mixing and boundary layer renewal while still providing a comparatively low pressure drop [85].

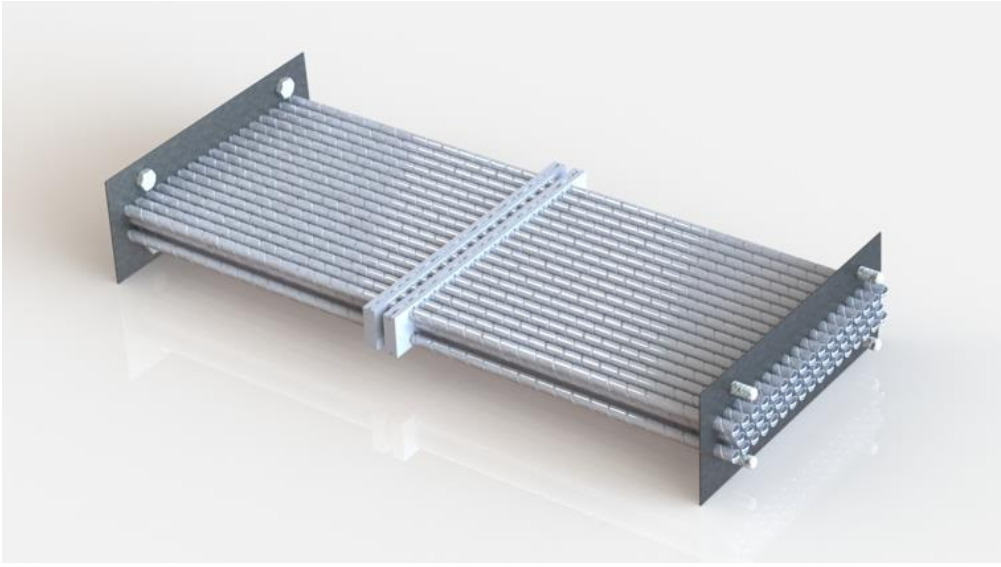

Figure 27 - Corrugated Pipes CAD Drawing.

Besides the specific corrugated pipe geometry choice, the main variable to consider is the spacing between them. It should be as small as possible so that the largest volume of exhaust gases can flow with a sufficiently low pressure drop so that it would not negatively affect the engine performance. Another advantage of having a high number of corrugated tubes is the increase in the heat transfer area which maximizes exhaust heat absorption. A greater number of corrugated pipes also reduces the molten aluminum mass needed and therefore the overall weight of the generator. Of course, the configuration presented in Figure 26 has still not been optimized for this purpose. A lighter configuration would be possible to design. In the case of this specific prototype, due to the aluminum melting process the minimum allowable spacing was 2 mm.

When working at their maximum temperature, the thermoelectric generator modules absorb their peak thermal power, so it is advantageous in these situations of high thermal power to have a by-pass system that offers a path of escape from excess exhaust gases, which will allow to reduce the back pressure phenomenon at the exhaust. This system is triggered whenever the TEG limit temperature is reached, and the exhaust gases are diverted so as not to damage the TEG modules. Unlike by-pass systems of existing concepts, this by-pass system does not waste otherwise useful heat because it will only activate once all the modules are operating at maximum power.

The condensable fluid used in VCHP's could be water, which boils at 250°C (maximum allowable temperature of the modules) at a pressure of around 40 bar. Alternatively, another fluid that has a saturation point around the same temperature of a much milder pressure would be also attractive. Using such fluid would substantially reduce the pressure inside the VCHPs as compared to water, thus decreasing the required level of robustness, complexity and precision of construction. As an example, a condensable fluid such as DowTherm-A boils at 250°C at a pressure of around 1 bar, making it an interesting alternative for this equipment (recall Table 1). However, as shown in [86], some experiments were made for maximum axial heat transfer. It can be stated that using water as working condensable fluid has a much greater potential than DowTherm-A as the heat transfer was double of that using the latter.

As analysed throughout the work, TEGs are an essential component of the functioning of a TCTG, so the choice of TEG is crucial for the success of the equipment and will always depend on the type of vehicle operating conditions in which it will be implemented. For example, a TEG with a high thermal power transfer such as the Adaptive GM127 should perform better on driving cycles with abundant available exhaust power, such as the custom highway (HW) cycle. TEGs with a lower thermal power transfer such as the Adaptive GM49 TEG will be best suited in driving cycles where the available exhaust power is lower, such as the WLTC3 cycle (Worldwide harmonized Light vehicles Test Cycle), therefore more suitable for light cars used in urban environment. On this prototype, HZ-14HV TEG modules were used. Although their matched load electrical power output values are placed in between the values of the TEGs presented above (17 W against 15 W in GM49 and 28 W in GM127) and the value of the maximum temperature of the hot face of the modules is the same (250°C) they have been chosen given their high robustness compared to the other modules, making it highly suitable for the type of use given the purpose of system implementation in a light duty vehicle.

3.2 TCTG Prototype Construction

After obtaining satisfactory results from the numerical simulation of the prototype [36], the research group started building what would be a downsized model of the final prototype for the heat exchanger designed to be tested and thus validate the concept.

In this phase, the casting components, which, due to their small dimensions, require precision, were planned and designed. Some casting attempts were made in order to perfect the technique and to understand how each material would behave with the aluminium casting at high temperatures. In Figure 28, one can see some of the attempts made by the LaMoTA group. It is possible to verify in Figure 28b that the aluminium has some solidification problems in colder areas of the moulding box, causing non-uniform distributions. The complete and uniform coating of aluminium throughout the prototype is important to ensure an even and planned heat transfer from the corrugated tubes to the TEGs that are placed in contact with the aluminium matrix.

Figure 28 - a) HPs and corrugated pipes placement planning; (b) Corrugated pipes casting tests and (c) 3D printed Positioners prototypes.

The prototype construction process started as follows: with the help of previously designed and tested positioners (displayed in Figure 29a and b), the corrugated pipes were aligned with the heat pipes and placed at a distance that allows them to be placed evenly inside the molding box.

Figure 29 - (a) Corrugated pipes and (b) HPs arrangement before casting; (c) Corrugated Pipes and HPs inside de moulding box ready for casting.

To perform the casting, some of the molding cavities were filled with sand to prevent the aluminum casting from filling unwanted regions. For instance, a separation region was added at the middle in order to obstruct longitudinal heat transfer along the aluminum matrix between the two halves of the system. Under these conditions, heat will only flow through the HPs. It is visible in Figure 29c that at the left-hand side the HPs are inside the desired casting region and, in contrast, at the right-hand side they are at the outside (region filled with sand). This was intended to study the system behavior with both inner and outer HP collectors, changing the flow direction of the exhaust gases. This feature was not explored in the course of the work of this dissertation.

To maintain the cold faces at their lowest possible temperature, a cooling system was designed to extract as much heat as possible from the TEG as evenly as possible. For this, densely finned aluminium cooling plates to maximize the heat extraction were built by machining inlet and outlet collectors into existing commercial extruded profiles and adding a cover. The covers were welded to the finned plates. In Figure 30 it is visible the inside of the plates, as well as the final model of one cooling plate.

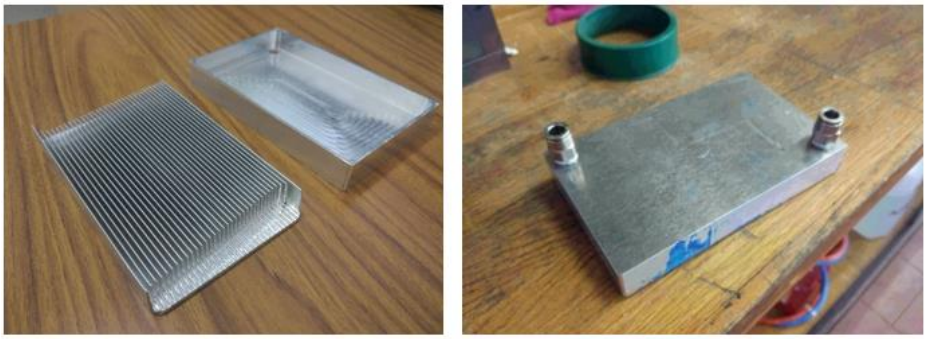

(a) (b)

Figure 30 – (a) Interior finned surface of a cooling plate and (b) Final cooling plate.

These plates were configured to work in countercurrent, meaning that the direction of the water flowing inside them is opposite to the direction of the exhaust gases. Each cooling plate was mounted to cool 2 TEGs. Two basic piping plug-in connectors were installed so that the piping system that feeds the cooling water can be easily connected.

After the casting was completed (see Figure 31a), the outer path of the heat pipes was mounted. In Figure 31b it is possible to see this component constructed of copper. Valves and basic piping connectors were used to attach all the components. Thin grooves were drilled in both the aluminum and the Colling Plates for implementation of the thermocouples to measure the temperature at the hot and cold faces of the TEGs.

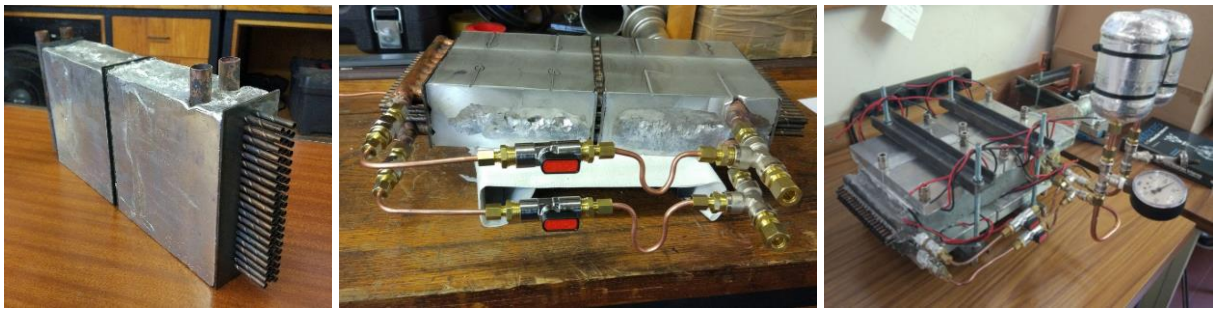

a) b) c)

Figure 31 – (a) HE after the aluminium cast, (b) HPs outside path construction and (c) TCTG after installation of TEGs, cooling plates, expansion vessels and pressure sensor.

Finally, it is possible to see in Figure 31c the almost complete system. The TEGs and the Cooling plates were installed and fixed through a system of beams, screws and nuts that guarantees a good contact pressure, thus minimizing contact resistances between the components. Likewise, the TEGs were wired to matched load resistances. At this stage the implemented expansion tanks and pressurization plugs are visible. It is through these components that the system is to be pressurized to the desirable 40 bar pressure to allow the vaporization of water at 250°C. However, leaks in the HPs system were discovered, resulting from problems related to the casting of the aluminum and the material of the HPs. For this reason, the present system was only tested near atmospheric pressure resulting in excess heat spreading temperatures around 100°C.

3.3 TCTG Modifications

In this subchapter, the modifications made to the existing prototype in order to test it experimentally and to evaluate its performance under predetermined test conditions are described.

3.3.1 Water Supply System

The circuit built for the cooling plates is visible in Figure 32. Collectors were built with 40 mm diameter PVC pipe that connected the laboratory water supply to the 8 cooling plates of the system. For that the tube was drilled and connectors were placed for smaller tubes supplying the water to the plates. Also thermocouples were placed to study the system behaviour in regards to cooling plates absorbed power.

(a) (b) (c)

Figure 32 – (a) inlet and (b) outlet water supply collectors and (c) fully built prototype with water supply system

The same process was repeated, for the pipe that receives the water from the cooling plates and redirects it to the laboratory's sewer.

3.3.2 Exhaust Gas Collectors

Two exhaust gas collectors were incorporated to direct the exhaust gases to and out of the HX (Figure 33). These components were drilled to later implement the thermocouples that would measure the exhaust gas at the inlet and exit of the prototype.

(a) (b)

Figure 33 - (a) inlet and (b) outlet exhaust gas collectors

3.3.3 Thermocouple Installation

To study the operation of the heat exchanger, since it is associated with heat transfer, temperatures were measured at various points in the HX. The temperatures measured at the HX were the hot and cold face temperatures of the TEGs and the inlet and outlet exhaust temperatures. The water temperature of the cooling system was also measured at the inlet and the outlet of the cooling plates. The measurement was made at the junction of all the water tubes coming to and from the cooling plates.

Details of the type of thermocouples used and measurement errors associated with these are described in detail in the chapter 0.

The thermocouples used were placed in pre-drilled thin grooves on the hot side (aluminium matrix) and the cold side (cooling plates). In the middle of these two components the TEG modules were placed. As these are in contact with metal, an insulating thermal grease was placed to coat and fixate the components (see Figure 34).

(a) (b) (c)

Figure 34 - (a) Thermal grease and thin grooves drilled in the (a) cooling plates and (b) HX to install the thermocouples

3.3.4 Load Resistances

The electrical power output is a result of the combination of voltage and current through the Joule's law (recall eq. (13)). The voltage generated by the modules is then dissipated by the load resistances attached to them.

The load resistances used in the prototype are the ARCOL HS50 0.47 Ω displayed in Figure 35. The load resistances were selected to be as close as possible to the internal resistances of the modules (varying from 0.55 Ω to 0.65 Ω according to the manufacture's datasheet) to attain the so-called matched load condition, where the power output of the modules is maximized (recall eq. (15)).

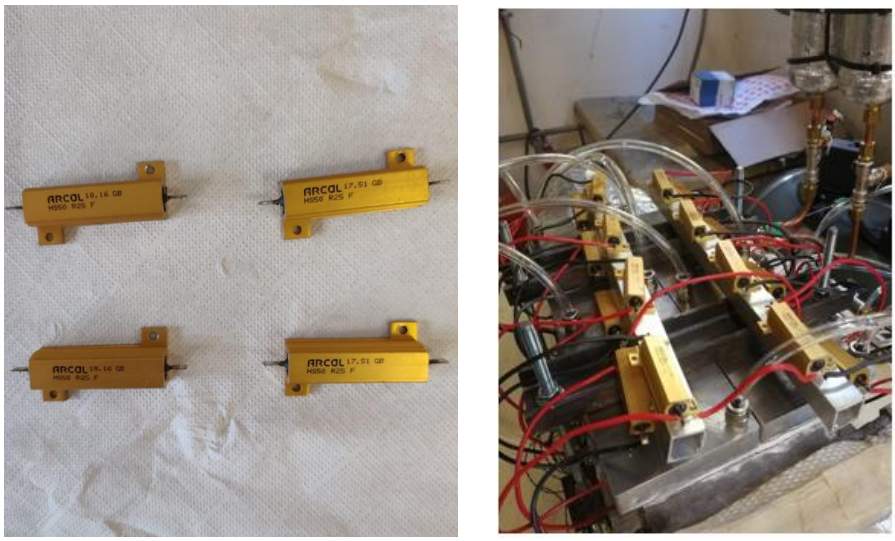

(a) (b)

Figure 35 - (a) Load resistances, (b) connected in series

Figure 35b shows the load resistor connections for each module of the prototype. Due to implications derived from the fact that there was a limitation with the number of inputs for the data acquisition system (detailed in the subchapter 4.1), the load resistances were connected two by two in series in a way that the voltage readings of these two resistances is equal to the sum of the voltage production of two TEG modules of the same row. This way it was possible to decrease to half the number of inputs, however is not possible to study the electric production of each side of the prototype but yes and only as rows of modules, from one until level four, in the upper and lower part of the TCTG. Note that that the final results of the electrical production of each TEG row must take into account that it represents the production of two TEG modules

3.3.5 Voltage Acquisition System

To ensure the load resistances compatibility with the data acquisition systems, specific connections were built. In the tested prototype, the voltage data acquisition system is a NI-9205 D-SUB voltage card, which is described in more detail in the subchapter 4.1.4.

Since this board has a 36 pin D-Sub connector, a connector to interconnect the load resistance voltage readings with the interface of the board was built as seen in Figure 36b and Figure 36c.

(a) (b) (c)

Figure 36 – (a) NI-9025 D-SUB voltage card; (b) D-Sub 36 pin connector built and (c)Full voltage acquisition system

Due to the sensitivity of the acquisition system, along with the high electrical noise region where it was located, a “custom box” was designed and built to provide a better insulation to the connector and the connections made. This box, presented in Figure 36c, improved the reliability of the voltage measurements.

4. EXPERIMENTAL PROCEDURE FOR THE TESTS OF THE EXISTING PROTOTYPE

A test rig for the TCTG and an experimental procedure were configured to verify experimentally the excess heat spreading phenomena, that hitherto had only been hypothesized theoretically [39], and to evaluate the system performance when attached to a light vehicle engine.

4.1 Experimental System Setup

To evaluate the energy conversion and electric power production, the TCTG was integrated into the experimental system. This experimental system consists of the TCTG, which is attached to the exhaust line of a light-duty spark ignition 1.6L engine connected to a brake dynamometer and to an open water-cooling circuit. Electrically, it is connected to a data acquisition system (see Figure 37).

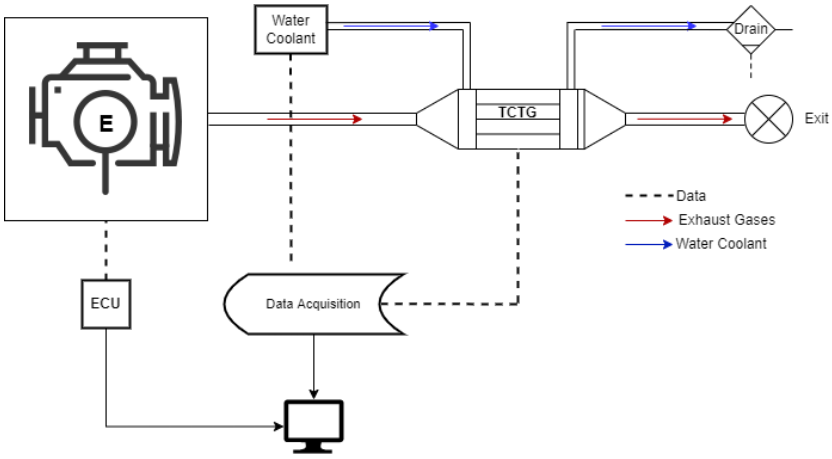

Figure 37 - Schematic representation of the facility.

4.1.1 Heat Exchanger and TEG Modules

The Heat Exchanger was integrated into the experimental system to evaluate the operating performance of energy conversion and electric power production. There are 16 TEG modules displaced and attached to the lower and upper surfaces of the HE, 8 on each surface, as shown in Figure 38. In this figure is possible to see the upper half surface of the HE with its corresponding 8 TEGs, numbered from 1 to 8 (one should recall that the lower half of the HE contains the remaining TEGs numbered from 9 to 16).

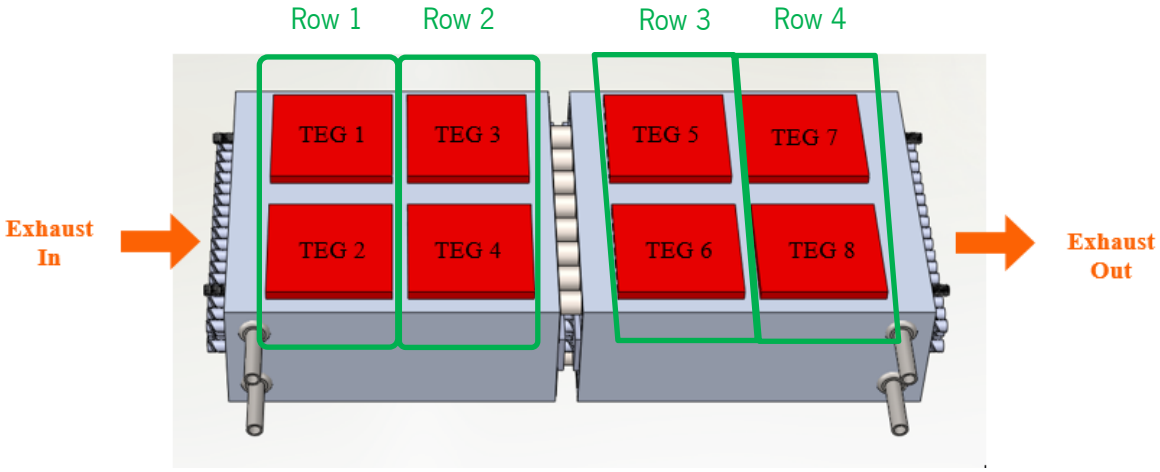

Figure 38 - TCTG TEG modules upper-half.

Since the TEG modules are connected in series in pairs of two (recall chapter 3.3.5), the nomenclature used throughout the work is presented as follows:

-When referring to the upper half of the prototype, **Row 1** consists of TEG 1 and TEG 2 (the first TEG row presented in the exhaust flow direction, see Figure 38), **Row 2** consists of TEG 3 and TEG 4, **Row 3** consists of TEG 5 and TEG 6 and **Row 4** consists of TEG 7 and TEG 8.

-When referring to the lower half of the prototype the same principle applies, being this time **Row 1** the first two TEGs on the exhaust gas flow direction (TEG 9 and TEG 10), and **Row 4** the last TEGs on the prototype (TEG 17 and TEG 18).

The TEG modules used are the *Hi-Z 14HV* optimized for waste heat recovery and their manufacture datasheet properties are described in Table 2.

Table 2 - Hi-Z 14HV TEG module datasheet [87]

Thermal and Electrical Characteristic					
Parameter	**Conditions**	**min**	**typ**	**max**	**units**
Power	Th=250°C, Tc=50°C	14	15.5	17.0	Watts
Open Circuit Voltage	Th=250°C, Tc=50°C	7.6	8.0	8.4	Volts
Matched Load Voltage	Th=250°C, Tc=50°C	3.8	4	4.2	Volts
Internal Resistance	Th=250°C, Tc=50°C	0.9	1.0	1.1	Ω
	T=50°C	0.55	0.6	0.65	Ω
Heat Flux	Th=250°C, Tc=50°C (matched load)	410	430	450	Watts
	Th=250°C, Tc=50°C (open circuit)	200	210	220	Watts

4.1.2 Engine

The engine used in the experimental validation of the concept is a light duty spark ignition engine (presented in Figure 39) and his specifications are displayed in Table 3. The engines that were available in the Lab was this one and also a Diesel one (1.6 HDI from PSA group). This one was chosen because petrol engines display a higher exhaust temperature on average and thus display a higher recovery potential than Diesels.

Figure 39 - TU5JP4 Engine.

Table 3 - Engine Properties

Engine Properties	
Engine Spec.	TU5JP4 from PSA
Engine Capacity	1587 cm^3 atmospheric
Cylinders	4
Volumetric compression ratio	11:1
Maximum Power	88 kW @6000 rpm
Maximum Torque	160 N.m @4250 rpm
Injection System	Multipoint Bosch Spark
ECU	ECUMaster® EMU
Fuel	RON95 Petrol

4.1.3 Cooling water system

The cooling system for the cold sides of the TEGs is composed of water collectors designed to distribute the flow along the several cooling plates, the piping system that connects the assembly and a rotameter water flow meter (see Figure 40). The detailed explanation of most of the water supply system components is outlined in chapter 3.2 and 3.3 with the exception of water flow meter. It was connected to the water supply system of the prototype and the water circuit of the lab. The flowmeter measurements [l/m] were used in thermal absorbed power calculations to evaluate the performance of the cooling plates.

Figure 40 - Water Flow meter.

4.1.4 Data Acquisition system

To assess the TCTG performance, a range of data acquisition techniques aimed at describing the heat exchanger and electric power production capabilities was used (see Figure 41a). The CompactDAQ C Series Multifunction modular system from *NI-National Instruments* that includes analog input, analog output, and 5 V TTL digital I/O channels was used (see Figure 41b). For the temperature readings two NI-9214 were used, for voltages a NI-9205 D-SUB and for pressures a NI-9201.

Figure 41 - (a) Data acquisition system table and (b) NI CompactDAQ modular system in blue.

4.1.5 Pressure

In this experimental system two types of pressure measurements were deployed. The first one was the pressure measurement inside the HP system, which allowed the indirect monitoring and control of the vaporization temperature of the condensable fluid. The second one measured the differential pressure drop of the cooling water flow between the entrance and exit of the cooling plates. The pressure drop of water flow on the cold-side cooling system was measured using a *JUMO® MIDAS* differential pressure sensor. This pressure transmitter acquires the relative pressure between two points of liquid or gaseous media and transforms it into an electrical signal. The two differential pressure acquisition points are highlighted in Figure 42a in the red arrows. The HP pressure sensor consists of a *GEMS® 3500 series* high pressure sensor which aims to measure the evolution of the relative pressure inside the system. This measurement device is presented in Figure 42b. The measurement parameters of each sensor are displayed in Table 4.

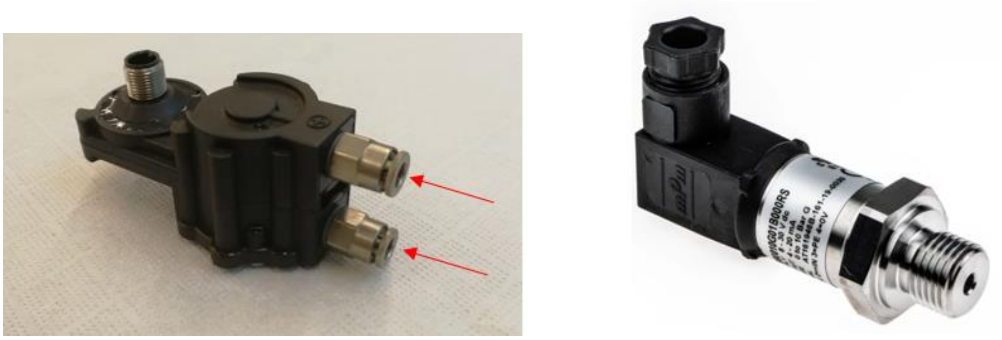

(a) (b)

Figure 42 - (a) Jumo Midas® differential pressure sensor; (b) GEMS® 3500 pressure sensor.

Table 4 - Pressure Sensors datasheet from manufacture

Pressure Sensors					
GEMS® General technical data					
Input	**Max. Overload**	**Bursting Pressure**	**Current Output**	**Temperature range**	**Overall Error**
0.35 +40 bar	80 bar	120 bar	4 to 20 mA	0°C/+ 120°C	0,0025*P and long-term drift of 0,2%
JUMO® MIDAS General technical data					
-1 +5 bar relative pressure	7.5 bar	60 bar	4 to 20 mA two-wire; DC supply 0 to 10V three-wire	-20°C / + 125 °C	0,0025*P

4.1.6 Temperatures

To measure the different temperatures of the system, 2 types of thermocouples were installed at the aforementioned points. The first ones are K-type thermocouples 1.5mm x 150 mm and the second ones are K-type 0.2 mm x 1 m thermocouple. According to the manufacturer datasheet [88], these thermocouples are capable of recording temperatures from a range of -40°C to 1100°C and they are in compliance with IEC584 Standards approval, which states the measurement error for K-type thermocouples is 2.5°C or 0.75% of the measurement temperature.

The temperatures measured at the HX were the hot and cold face temperatures of the TEGs and the inlet and outlet exhaust temperatures. The water temperature of the cooling system was also measured at the inlet and the outlet of the cooling plates. This measurement was made at the junction of all the water tubes coming to and from the cooling plates.

4.1.7 Voltage

The main voltages measured during the test were the ones generated by the modules due to the Seebeck effect (recall chapter 2.1.1). This voltage is then dissipated by the load resistances attached to them. The specific load resistances used in the prototype are described in chapter 3.3.4. This voltage is measured by the NI card, recall subchapter 4.1.4 . Other voltages were measured, such as those from the pressure transducers and thermocouples.

4.1.8 LabVIEW®

The software LabVIEW® was used to control the data acquisition cards, provide a graphical user interface (GUI), and allow the programming of the channels to be acquired and displayed in real time in the computer screen. A custom LabVIEW® program was previously developed to record all main parameters. At the end of a test the software would generate a text file containing the values of the measured parameters such as temperatures, pressures, and TEG voltages. These parameters were then processed and displayed graphically for the later analysis of system performance.

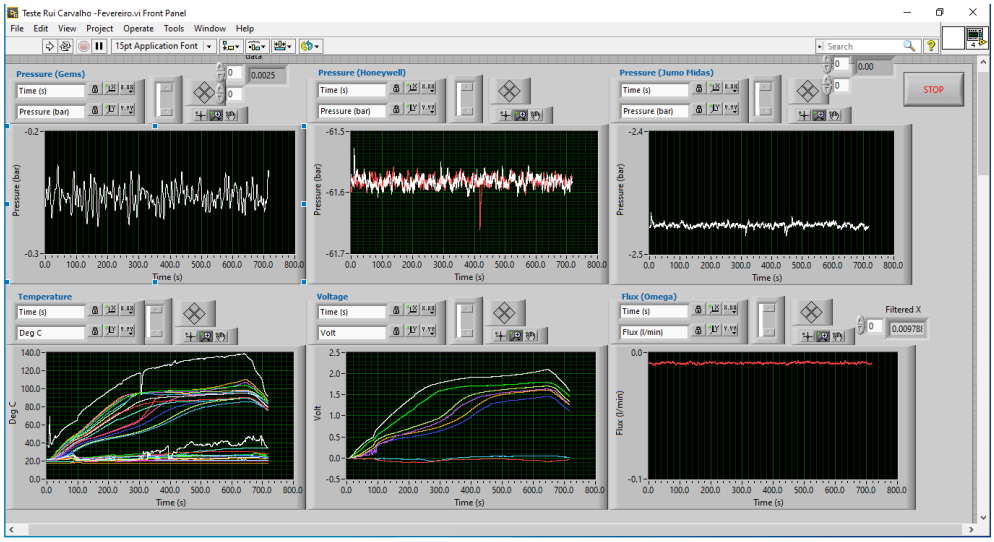

Figure 43 - LabView® software used to monitor and record TCTG data acquisition parameters during the test cycle.

4.1.9 ECUMaster®

To control and record some engine operating parameters, a programmable engine control unit (ECU) was used (see Figure 44a). The engine control hardware and software are from ECU Master®, model EMU® (Engine Management Unit).

This allowed changes in parameters such as ignition advance and air-fuel ratio. It also allowed real-time monitoring and storage of engine operating data during the performed tests (see Figure 44b). After the test, the software would generate a *.csv* file containing the records of predefined parameters. These parameters were the engine RPM, TPS (Throttle Position Sensor), IAT (Intake Air Temperature), CLT (Coolant Temperature), Fuel Usage and Lambda. These parameters were used in the performance study of the prototype.

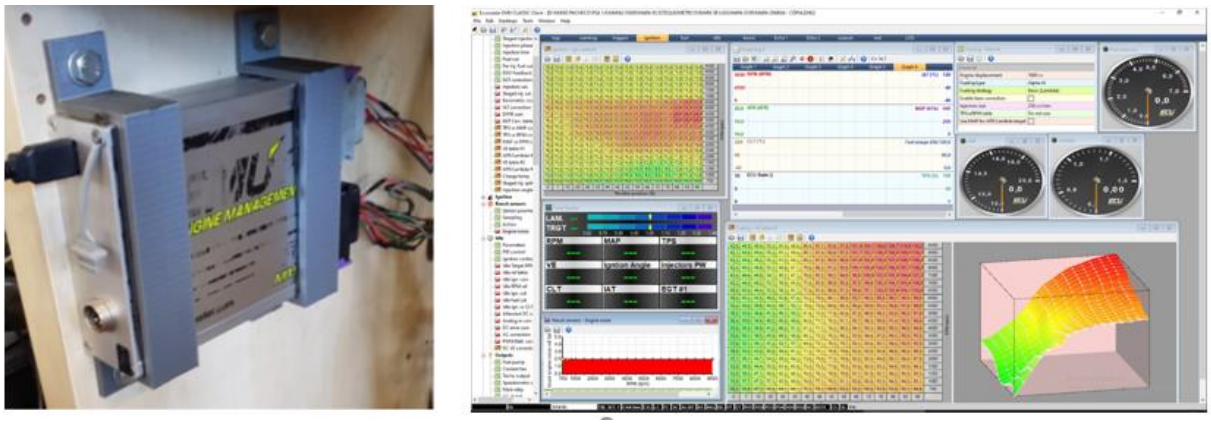

a) b)

Figure 44 - a) Engine Management Unit and b) ECUMaster software used to change and record engine parameters during the test cycle.

4.1.10 MATLAB®

A MATLAB® code was developed to analyse the bulk data acquired during the tests, and to perform calculations related to the performance of the system. This code would read the two files produced by the NI data acquisition system and the ECU software mentioned. Then it would perform some calculations to obtain the performance parameters in numerical and graphical form. These included the instantaneous or time-averaged values for the exhaust mass flow rate, thermal power absorbed by the TCTG and released to the cooling system, real and estimated matched load power produced by the TEGs. Some of the calculations performed by the code to obtain the TEG power output and efficiency, TEG´s maximum theoretical power, absorbed thermal power and Heat Exchanger Effectiveness are presented in sub-chapters 2.1 and 2.2.

4.2 Test Procedure

All sensors such as thermocouples, voltage and pressure sensors were connected to the data acquisition system which was bridged to a computer running LabView®. The ECU was connected to a second computer running the ECUMaster® data acquisition and engine control software (recall Figure 37).

The TCTG heat pipes were previously filled with water (60ml in each HP system). As a result of the casting process both HP batteries had pressure leaks, making it impossible to pressurize the system to achieve the intended boiling temperature of 250°C. Nevertheless, it was deemed that performing the tests at ambient pressure, and thus with a corresponding saturation temperature around 100°C, would still be insightful, as it would still allow to observe the phenomena of temperature control and excess heat spreading and thus validate the concept.

The engine operating conditions were defined based on preliminary tests. It was decided that the engine would work near 3000 rpm and with no load (no braking torque in the dynamometer). This was indeed sufficient to produce enough heat to observe excess heat spreading phenomena and achieve full TCTG operation. The volumetric water flow rate used was 10.3 L/min. The ambient temperature in the lab was roughly 23°C.

Figure 45 - Ready to test prototype.

In this experimental procedure, the following steps were followed during each test

1. Turn on the data acquisition systems;
2. Start the recording of values from LabView and ECU acquisition system simultaneously (facilitating synchronization for later analysis);
3. Start the combustion engine and begin engine warm up conditions (2400 rpm for 100 seconds);
4. Turn on the water flow of the cooling plates, and perform leakage verification;
5. Measure water flow rate;
6. After 100 seconds, change Engine speed to 3000 rpm;
7. Gas and water leakage verification under test-conditions;
8. Thermal image acquisition after system thermal stabilization;
9. After 700 seconds from test beginning, reduce engine speed to idling conditions;
10. Turn off combustion engine;
11. Turn off water flow of the cooling plates;
12. Stop and save the LabView and ECU data, performing this simultaneously;
13. Export recorded data acquisition for further treatment in MATLAB and later analysis.

5. RESULTS AND VALIDATION OF THE EXISTING PROTOTYPE

5.1 Experimental Results

5.1.1 Engine speed and available exhaust power

The operating engine's analyses obtained through the ECUMaster® software provides information about the characteristics of the engine operation over time. In Figure 46, it is possible to see the evolution of engine speed (in RPM) throughout the test, as recorded by the ECUMaster® software. This data is important for the numerical simulation of the system as subjected to an equivalent scenario. Figure 46 also shows the exhaust power delivered by the engine during the teste cycle.

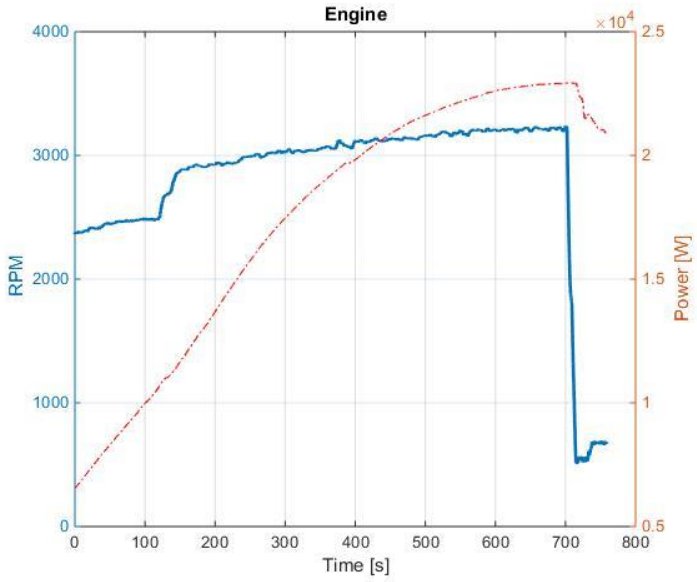

Figure 46 - Engine Speed and exhaust power throughout the test cycle.

It should be recalled that no braking torque was applied to the engine, so the engine load was quite low, only sufficient to overcome engine and brake dynamometer friction losses. Nevertheless, this thermal load was sufficient for the generator to operate at full load, as seen further ahead. This information gives the possibility to evaluate the engine speed during the test and is important in the study of Engine/Heat Exchanger operating in driving cycles.

The test consisted of two engine stages: a first one, in which the engine rpm was set at around 2400-2500 rpm, and a second one in which the engine was accelerated up to around 3000 rpm. This acceleration happened around the instant 150s of the test. The slight rise in engine speed over time for

both conditions is due to the natural warming-up of the engine, as the test started with an engine cold start.

The exhaust power is also seen in Figure 46. It is an important parameter, as the electrical energy produced is a fraction of this heat (recall eq. (29)). It is calculated through eq. (28), by means of the temperature difference between the inlet and outlet exhaust temperature and also the volumetric flow rate of the exhaust gases, calculated from the ECU recorded data. The reason for the steady increase of the exhaust power is the gradual increase of both the engine speed and the exhaust temperature (the latter can be seen in Figure 47).

5.1.2 Heat Exchanger Effectiveness

Figure 47 displays the exhaust gas temperature at the inlet and at the outlet of the system. It can be seen that the exhaust temperature increased from around 200°C to slightly over 500°C at the end of the test, justifying the increase of the exhaust power seen before in Figure 13. There, one can also see that the temperature of the outlet exhaust gases is much lower than the temperature of the inlet exhaust gases. This temperature differential and the exhaust flow rate are the parameters that yield the heat absorbed by the system (recall eq. (29)). The HX effectiveness, $\in$, can also be seen in Figure 47. By recalling that $\in$ is calculated from Eq. (30) , it can be seen that the closer the outlet temperature is from the heat sink temperature (water inlet temperature), the closer from 100% will $\in$ be. It can also be seen that until around 200 s of operation $\in$ is very high, surpassing 90%. After this, the exhaust outlet gas temperature starts rising steadily until almost 600 s. This rise provoked a steady decrease of $\in$ down to a minimum which was slightly below 80%. These effectiveness values seem rather high, nonetheless, indicating a good heat absorbing capacity of the prototype without the risk of overheating.

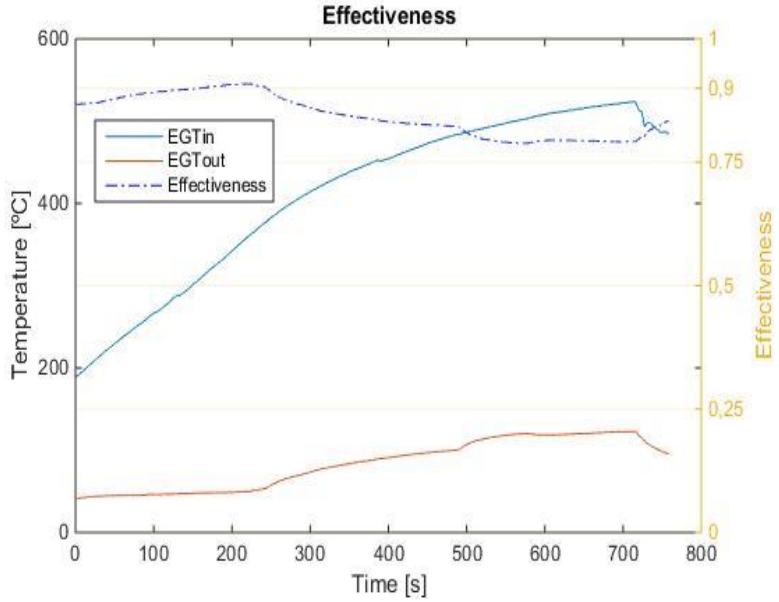

Figure 47 - Exhaust inlet and outlet gas temperature and HX Effectiveness.

One reason for the decrease of ∈ around 200 s is the acceleration of the engine from 2500 to 3000 rpm that starts occurring from 150 s. When the engine is accelerated, more thermal power is available (higher exhaust gas flow rate). Under these conditions, the system will tend to absorb, in absolute terms, a higher thermal power, but the fraction of the total power available that will be absorbed will be slightly lower (thus the lower ∈). But the change in the available thermal power due to engine speed seems not to be the only reason for the changes in ∈. The start of the operation of heat pipes also affects this parameter, but this can only be explained by looking at additional test data, as detailed further ahead.

As for example, if the exhaust gases leaving the system had the same temperature as the flowing cooling water (EGTideal), then the effectiveness would be 100% and the heat absorbed would be as much as theoretically possible. For this reason, at the beginning of the cycle, the highest effectiveness is achieved (90%) as the exhaust gases leave with temperatures close to water cooling ones.

However, as the exhaust gases entering the system increase in temperature and the heat-pipes come into operation, there is no longer as much capacity to absorb the available heat as the temperature of the exhaust gases increases. As a result of this increase as showed in Figure 47, the effectiveness decreases, as the exhaust gases are already hotter than the coolant.

Nevertheless, the lowest effectiveness achieved during the cycle is around 80%. This indicates a good heat absorbing capacity of the prototype.

5.1.3 Temperature Analysis

Figure 48 may be the most insightful figure of the experimental data as it seems to illustrate the temperature limitation and excess heat spreading features, which are the main novelties of the concept proposed previously by the LaMoTA team and to which the present work aims to provide experimental evidence.

This figure displays the hot face temperatures of each row of TEGs, starting with Row 1, the first, more upstream row, and ending with Row 4, the last, more downstream row. It is important to recall that the aluminium block in which both the corrugated pipes and the HPs are embedded has been divided in two separate blocks with an air gap between them (recall Figure 38). Only the corrugated pipes and HPs cross this air gap and are connecting both blocks. This way, Row 1 and 2 are attached to the upstream block, while Row 3 and 4 are attached to the downstream block.

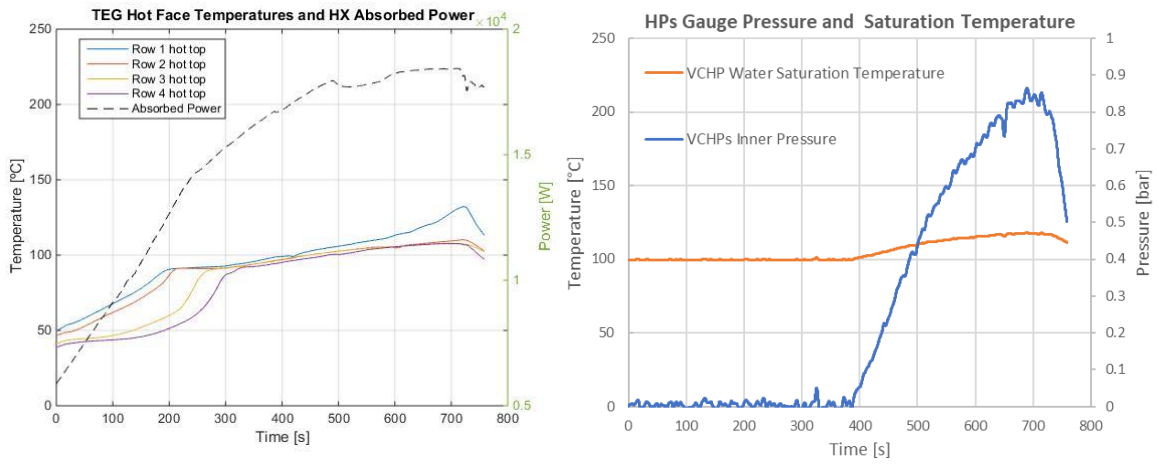

(a) (b)

Figure 48 - (a) Hot face temperature at each row of TEGs (upper-half) and total electric power; (b) Heat Pipes inner pressure evolution (gauge pressure) and water saturation temperature analysis.

In Figure 48 it can be seen that the hot face temperature rises firstly at the TEG rows attached to the upstream aluminium block (Row 1 and Row 2) and only later in the TEG rows attached to the downstream block (Row 3 and Row 4). This makes sense, because the exhaust gases are hotter at the entry of the system and they decrease in temperature along the HX, as they release their heat to it. It may be seen that the TEG rows attached to the same block display similar temperature levels, with the row located more upstream displaying a slightly hotter temperature than the row located more downstream. The temperature uniformity in TEGs attached to the same block is expected, because aluminium has a high thermal conductivity, causing a substantial longitudinal temperature uniformity.

Figure 48 is also highly relevant as it provides evidence of the temperature limitation provided by the HPs. In fact, around 200 s, when the hot face of the TEGs attached to the upstream aluminium block (Row 1 and Row 2) approach the HP saturation temperature (around 100°C), the temperature gradient of these TEG rows starts stagnating. This means that the HPs have started to absorb heat by vaporization in this region and are effectively preventing the TEGs from increasing their temperature beyond the limit set (100°C). This seems to validate the temperature control concept proposed by the authors.

Another important phenomenon that can be observed in Figure 48 is that once the temperature stabilizes, at the TEG rows attached to the upstream aluminium block, around 200 s, the temperature at the TEG rows attached to the downstream aluminium block immediately start increasing, until all TEG rows reach a similar temperature level (around 100°C) shortly after 300 s. Like explained above, the two aluminium blocks have an air gap between them. This means that there is no heat conduction between them and, therefore, the temperature rise that one block seems to cause on the other block should necessarily be caused by the excess heat spreading performed by the HPs, that is, the heat absorbed by phase change at the upstream block is being delivered to the downstream block promoting its quicker heating up and temperature uniformizing to 100°C. Thus, not only the claim of temperature limitation, but also that of excess heat spreading are confirmed by the experimental results.

Now, it must be acknowledged that in reality, and according to Figure 48 the temperature limitation effect is not completely achieved. Beyond 400 seconds of test, it can be seen that the temperature continued to rise slightly, eventually overcoming 100°C. In fact, this is because the present prototype still lacks a component already described above as being necessary for the system to work properly. This missing additional system is an excess vapour condenser, that could also be complemented by an exhaust by-pass that would cut-off the excess exhaust power. If present, the excess condenser, located downstream of the last row of modules, would have the function of condensing the vapour that would otherwise overflow the system and thus prevent pressure build-up. In fact, pressure build-up can be detected in Figure 48b, which displays the evolution of the HP inner pressure (gauge pressure) along the test. It may be seen that the pressure was around ambient pressure (0 bar) until around 400 s of test time, where it started to steadily rise, up to almost 0.9 bar at 700 s. It may be seen that the start of the pressure rise approximately coincides with the instant where the temperature uniformity was achieved in the whole system (~400 s), that is, the HPs started to overflow with vapor, up to the point where the pressure started to increase. The increase in pressure induced an increase of the boiling temperature from 100°C at 0 bar to around 120ª C at 0.9 bar. This is precisely the range of temperatures achieved at the TEG Hot

Faces. Once an excess vapor condenser is installed or a by-pass valve starts diverting excess exhaust power from the system, the temperature will be effectively limited.

Also using the theoretical water saturation temperature values for each given pressure, it was possible to create a water saturation temperature curve for each given gauge pressure value along the experimental test and therefore one for each time step. This way, it is possible to predict what would be the saturation temperature inside de HPs during the test cycle. This analysis is presented in Figure 48b and it is important to understand the TEG hot face temperature rise over time. It can be seen that, apart from the first TEG row, the remaining rows followed this saturation temperature curve, meaning that the system is accordingly to its principle of operation.

Regarding the heat exchanger detailed analyses, it is possible to measure and evaluate various functions of each component of the system layout. In Figure 49a and Figure 49b, the detailed temporal evolution of the hot and cold face temperatures of the TEGs on upper and lower half of Row 1 is presented (Left and Right).

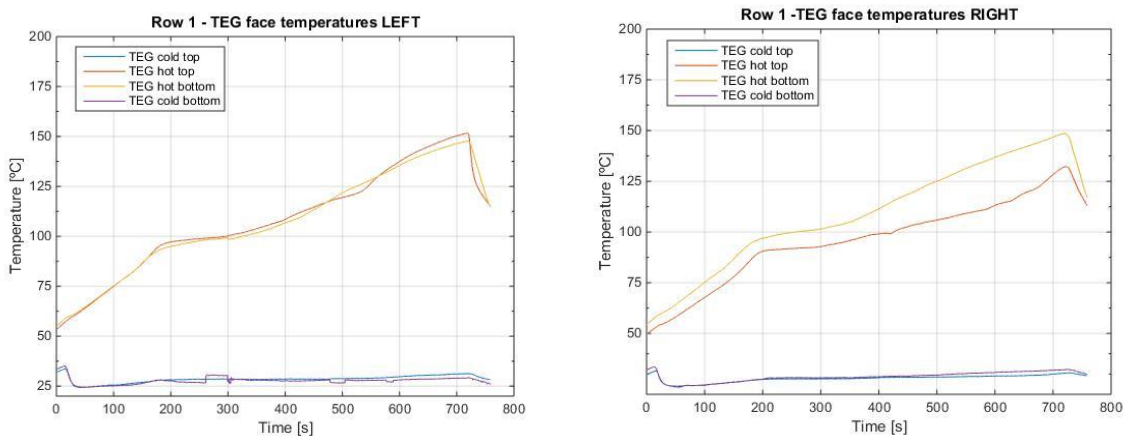

(a) (b)

Figure 49 - TEG hot face evolution compared by (a) left and (b) right side.

Despite in Figure 49b the hot top and hot bottom display some divergence in temperature absolute values (which seems to be more of a measurement error, like thermocouple bad positioning), on both sides of Row 1 the temporal evolution of temperature is quite similar. There is a change in temperature gradient around 200 seconds resulting from the start of heat pipes operation (the temperature is reached at 100 °C and there is evaporation of the water inside HPs), which causes heat distribution and decreases the rate at which the hot face of the TEG increases in temperature. The TEG cold face maintains a stable temperature of around 28°C throughout the test. This factor is important for the prototype success as it

ensures that the temperature differential between the faces of the TEGs increase throughout the cycle which will be directly related to the electrical output of the HE.

5.1.4 Electrical output and efficiency

As the primary goal of this prototype consists on the conversion from thermal to electrical power, the voltage and power produced by the TEGs are among the main indicators to analyse the system performance. Based on eq. (1) the voltage is expected to be proportional to the temperature differential obtained for each TEG. It is possible to verify that this premise is true, and that the curve of the voltage graph seen in Figure 50a, obtained by direct measurement, evolves similarly to the temperature curve (seen in Figure 49).

The limited number of voltage input channels available in the data acquisition system led to the choice of connecting in series the load resistances of the left and right modules of each row. Therefore, the voltages measured and the corresponding obtained powers correspond to the pairs of modules belonging to each row (recall outline of Figure 38).

The electrical power generated is a function of voltage and of load resistance (recall eq. (14)), thus it is possible obtain the electrical power curve through the voltage curve, as seen in Figure 50.

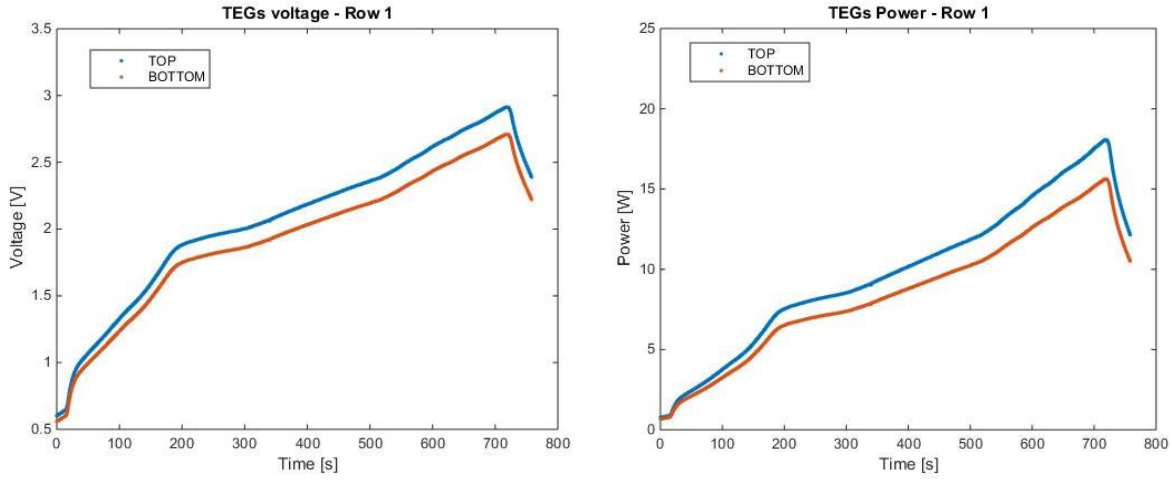

(a) (b)

Figure 50 - a) Row 1 TEG Voltage Output and b) Row 1 TEG Power Output.

To obtain maximum power the load resistance should be equal to the internal resistance of the modules (matched load conditions). The load resistance used was very close to the internal resistance reported

for the modules at ambient temperature. Nevertheless, a correction for estimating the theoretical matched load power was also used (eq. (18)). The differences obtained were negligible.

The electrical power output of each module increases with the square of the voltage (eq. (14)), so it is expected to see a sharper increase than the voltage. In terms of electrical output, it is noteworthy the functioning of the first TEG rows in comparison to the last ones (see Figure 51). The closer the Row is to the exhaust gas inlet, the greater the power generated. This results from the heat absorption from the exhaust gases throughout the system. Thus, the Row 4 is the one that receives the least heat as much of it has already been absorbed by previous rows. By consequence it is the TEG row that produces less electrical power.

In Figure 51 it is also possible to see the system total electrical power production which represents the sum of the electrical power output of the TEG modules. The maximum value achieved during this test was around 90W. Being the steady state point where the heat pipes are filled with steam and the TEG's hot face is the same. For a setpoint of 100°C, if an excess condenser or a by-pass valve were used, the system should stabilize around 350 to 400 seconds, meaning a maximum power output of around 60W. If it was possible to reach 250°C the maximum output should be considerably greater as power increase with increases with the square of the temperature (recall eq.(14)).

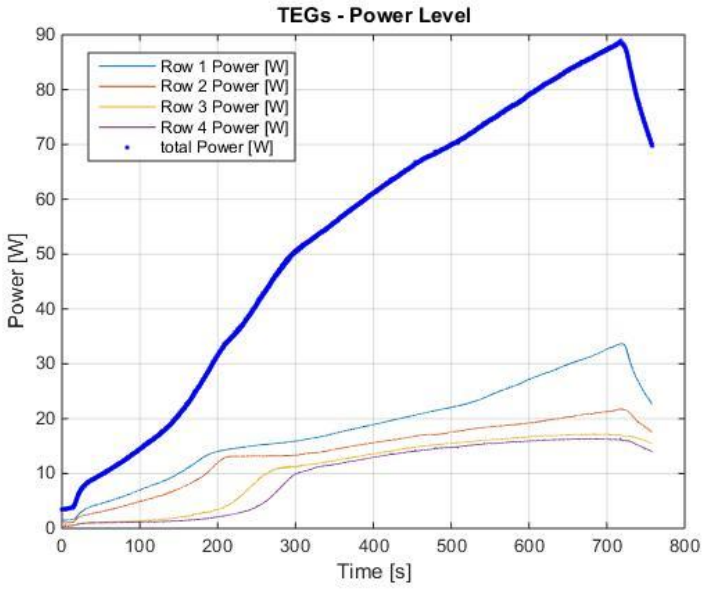

Figure 51 - TEGs Power by Row and TEGs Total Power Output.

The electrical efficiency expresses a ratio between the electric power generated and the thermal power absorbed by the system and by the TEGs (recall eq. (19)). It is as important as the electrical power output, especially in limited thermal power events, such as urban driving with cold engine. The efficiency of the system tested was studied (see Figure 52).

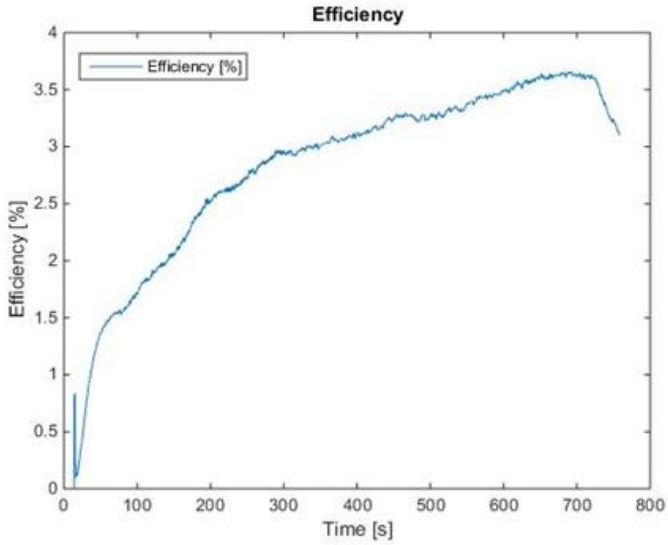

Figure 52 - TEGs efficiency during Test Cycle.

As the cycle progresses, the electrical efficiency increases as a result of the increase in the temperature differential between the TEG's faces throughout the cycle, which is directly related to their efficiency. The maximum efficiency recorded was 3.5%., this efficiency is at the upper spectrum of what could be expected from the *Hi-Z 14HV* TEG. This is surprising because during the cycle under-study, the maximum operating temperature of the TEGs (~120°C) was far from the maximum operating temperature of 250°C, where they are most efficient (~5%). This indicates that factors that normally reduce efficiency, such as thermal contact resistances, here have been minimized (thermal grease was used).

The analyses performed were able to calculate some mean values for a given steady state of choice. For this test, an interval from 300 seconds to 400 seconds was chosen given to be moment when all the HP's system was full and the Heat Exchanger was in full operation. Table 5 shows some of the calculated mean values.

Table 5 - Mean Values of Test in Full Operation

Variable	Mean Value	Units
EGTin	420	[°C]
EGTout	75	[°C]
Cooling water Pressure drop	40	[mbar]
Exhaust mass flow rate	41.1	[g/s]
Fuel consumption	7.44	[l/h]
Power absorbed by exhaust heat exchanger	15.6	[kW]

5.1.5 Voltage and Power as a function of Temperature

TEG's energy production is related to the temperature differential between their hot and cold faces. It is therefore interesting to establish a relationship between the electrical power produced and the temperature differential of the TEGs. Figure 53 displays the Voltage and Power of the TEG´s output for each temperature differential registered throughout the test cycle.

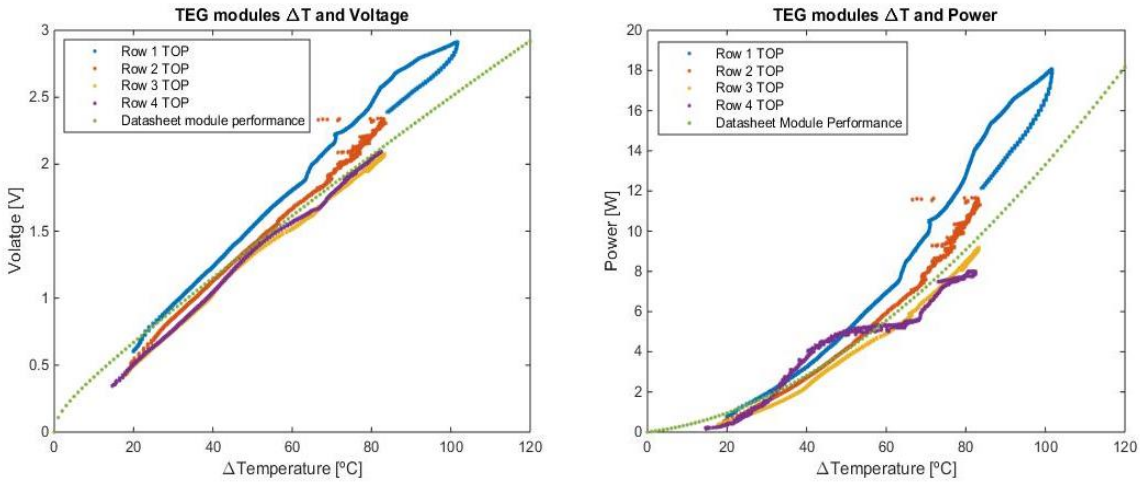

(a) (b)

Figure 53 - TEG a) voltage and b) power as a function of temperature differential.

Under steady state operation, for the same temperature difference the TEGs should all produce the same power output, however, this was not the completely the case. Small differences are visible depending on TEG position at the HX. These results were obtained under transient regime, so that thermal equilibrium has not yet been reached, and there are differences due to thermal inertia. This may mean that the temperature measured by the thermocouples might not be fully representative of the average temperature

of the hot faces. The greater the temperature difference, the greater the power generated (as already been mentioned on the functioning of the TEGs).

The graphics of Figure 53 present some undesirable noise, as well as anomalous behaviours that can be related with the change of the flow regime of the exhaust. For example, when the engine is switched off but the temperature in the prototype remains.

A comparison was made between the performance of the TEG in the experimental test with the performance data provided by the manufacturer. This information data had to be corrected, as the internal resistance of the module was actually substantially lower than that stated in the datasheet. While this does not affect the voltage (matched load voltage is half of the open circuit voltage, which in turn is solely a function of the temperature differential and the Seebeck effect according to eq. (1)), it affects the power (recall eq.(14)). In Figure 53a and Figure 53b it is possible to see the green line that represents the performance of the TEGs based on the corrected manufacturer data. In conclusion, it can be stated that the performance of some modules (more specifically of the ones from Row 1 and 2) is higher than that announced by the manufacturer, especially when the temperature difference between the TEG's hot and cold face is greater than 60°C. The difference seems to be mainly in the internal resistance of the modules, which seems to have been improved over the datasheet information. This yields a similar open circuit voltage but a much higher matched load power output than reported in the datasheet. It is worth noting that the lower internal resistance of the modules purchased was actually provided by the manufacturer when supplying the modules.

5.2 Numerical Model Validation

The experimental results obtained allow the validation of the numerical approach that has been previously used by the group to model the heat spreader concept that was proposed earlier [39]. This subchapter outlines the mathematical model used, presents the simulation results when using the same exhaust input as in the experimental results and compares the simulation results against the experimental results.

5.2.1 Outline of The Model

The LaMoTA research group developed a mathematical model to predict the system behaviour. The main goal of this approach was to predict the electric power output of this prototype during predefined driving cycles. The model was described in [34], while the electrical output of the TEGs, as well as its impact on fuel economy and GHG emissions were assessed under the Worldwide Harmonized Light Vehicle Test Cycle class 3 (WLTC) and a custom highway (HW) cycle. In the present work, a custom cycle which mimics the experimental test conditions (inlet exhaust thermal power as seen in Figure 46 and inlet exhaust temperature according to Figure 47) was simulated as it is described afterwards.

The model's engine and driving cycle energy analysis was developed in earlier work [34] [89]. It predicts the instantaneous engine map position such as speed and torque to complete the driving cycle and the corresponding instantaneous exhaust mas flow rate and inlet temperature.

The heat transfer and thermoelectric model was originally proposed in [38]. It is a model with discretization in the longitudinal direction into 72 sections in which 1D thermal calculations are made, and where the gas/coolant outlet temperature of each section is the inlet temperature of the next section, thus guiding the thermal simulation calculations of the system as a whole.

In each of these sections, heat is transferred from the exhaust gases (corrugated pipes) to the coolant (cooling plates):

- Heat transfer calculations are performed for each section, namely, the thermal resistances between the exhaust flow, the HX body (including HPs if active), the modules and finally the cooling flow. For the convective heat transfer calculations in each section empirical correlations for the convection at the exhaust flow and coolant flow are used. For the heat flow across the HX, 1D conduction equivalent thermal resistances were derived from 2D numerical heat transfer calculations done with commercial packages, as seen in Figure 54b.
- Two different heat transfer calculations are made in each section depending on whether there is excess heat spreading condition (active HPs) or not.

- In each section heat fluxes and temperatures are calculated. vapour production, accumulation and depletion are also calculated in case the HPs are active.
- Once the calculations in one section are completed, energy balances are made to calculate the temperature of the exhaust gases and water at the entry of the next section. Also, depending on the vapour produced, transported or depleted on the preceding section, the vapour accumulated for the next section is obtained.
- Simplified thermoelectric calculations are made based on the resulting temperatures at the hot and cold faces of the modules and the manufacturer datasheet [38] The average Peltier effect is incorporated into an effective thermal conductivity that already accounts for this effect.

All the physical properties of the materials, fluids and components were extracted from the manufacturer datasheets aiming to confirm that the electrical output of the system corresponds to the prototype built in real world.

For simplification reasons, conduction transfer along the length of the HX was not considered. In the built physical prototype, which was described previously, there is a discontinuity/separation of the aluminium matrix for each 2 TEG module rows, so that this longitudinal heat transfer in the real prototype is limited. Under these conditions, this simplification seems acceptable.

The thermal power flowing from the corrugated tubes to the cooling water on each of the 72 sections depends on the heat pipe thermal resistance which varies depending on whether the HP are active or not. For the calculation of the 1D equivalent thermal resistance, either an adiabatic or isothermal wall boundary 2D condition solver was used to represent the conditions where the HPs were inactive or active, respectively, as seen in Figure 54b and Figure 55.

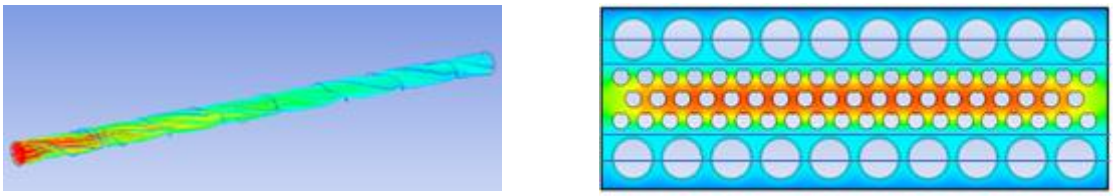

(a) (b)

Figure 54 - (a) CFD simulation of a corrugated pipe; (b) 2D heat conduction simulation of the exhaust heat exchanger [39].

The prototype studied in the present work (depicted in Figure 26) represents one fourth of the total system length of this model. This means that in the input and output of the modelling and simulation process, some adaptations to the model had to be considered.

Figure 55 shows an example of the geometry used in the 2D calculations to extract the 1D thermal resistances of each one of the 72 sections of the HX. One can see the main block which contains the corrugated pipes embedded with aluminium and the HP region divided into upstream and downstream region, R1 and R2, respectively. By performing 2D simulations of the heaty transfer occurring in these complex shapes for a given temperature differential, it was possible to extract an equivalent 1D thermal resistance that would be valid for other operating conditions. In this way, it is possible to adapt this complex shape to a 1D analysis. These thermal resistances are different whether HPs areas active or not. An adiabatic HP surface corresponds to the situation where there is no phase change occurring (temperature has not exceeded the HP saturation temperature). The situation with active HPs corresponds to isothermal HP surface (temperature has achieved saturation temperature). The detailed outline of this model, as well as the condition solver simplifications were presented in [38].

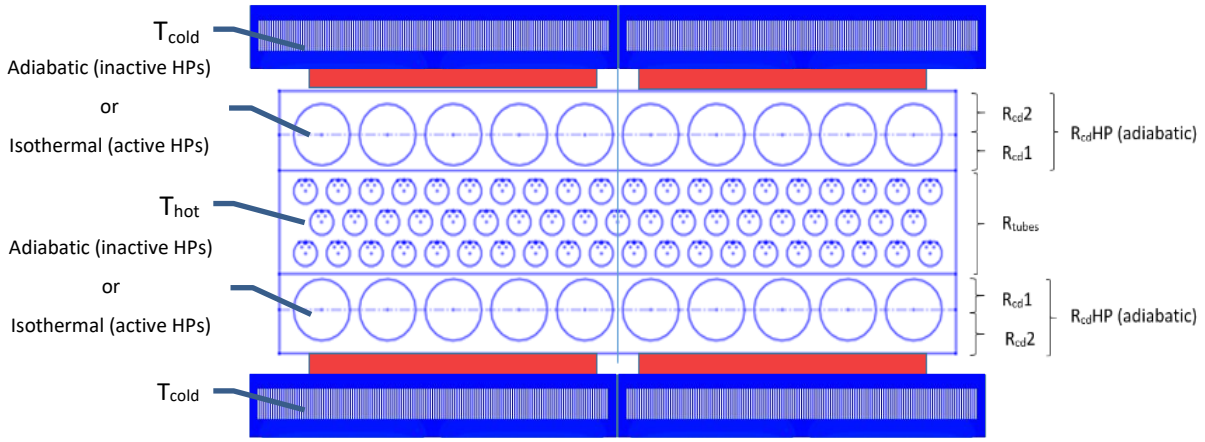

Figure 55 - 1D Thermal resistance scheme extracted from the 2D heat transfer simulation of a section of the HX under active and inactive HP condition.

The numerical model requires two main input parameters: the exhaust mass flow rate or power (Figure 46) and the exhaust gas inlet temperature (Figure 47) as a function of time. Any driving cycle, be it more variable or more stable can be programmed as long as the aforementioned values are extracted for each time step (in this case every second) [27][34], [89]. In the present case, these values were extracted from the engine ECU file (mass flow rate data) and from the data acquisition system (exhaust temperature data).

5.2.2 Numerical model correction for heat capacity

It must be noted that the model is a quasi-steady state model, meaning that it does not incorporate the influence of the heat capacity of the solid and liquid masses. What happened in the tests was that under transient operation (heating over time) a fraction of the heat absorbed by the HX was stored in it due to its heat capacity and was not transmitted to the modules.

In order to overcome this model limitation, a correction of the inlet exhaust power was performed so that the heat stored in the heat exchanger and the working fluid through heat capacity was discounted from the heat absorbed by the HX. This correction brings the mathematical model closer to reality. The heat required to heat the heat exchanger from ambient temperature to the vaporization temperature of the working fluid (100 °C) was calculated. For this calculation the mass of the aluminium matrix and the working fluid (water) were used as follows:

$$Q_{Heat} = \left(m_{al} \cdot c_{p_{al}} + m_{water} \cdot c_{p_{water}}\right) \cdot (T_{vap} - T_{amb}) \tag{34}$$

After calculating the heat value that is necessary to heat the HE from ambient temperature to 100 °C (working fluid vaporization temperature), the next step was to calculate the average heating power. In this way it was noticed that, in the results of the experimental tests, the system needed in average about t=200 seconds to reach the vaporization temperature in the hot faces of the modules. So, for the same engine parameters, the heating power can be calculated as follows:

$$P_{Heat} = \frac{Q_{Heat}}{t} \tag{35}$$

The resulting power due to heat capacity was subtracted at each instant from the exhaust gas power in order to obtain a corrected exhaust power. A corrected exhaust gas temperature for each time step was derived and used in the heat transfer calculations.

With this model adaptation, it was possible to incorporate the influence of thermal inertia in a simplified way and thus enable a valid comparison between theory and experiments.

5.2.3 Numerical Validation Results

Figure 56a and Figure 56b displays the comparison between the experimental and theoretical values of the electrical power output as a function of time, as in total electrical output and electrical output for each

TEG Row. The maximum value of total electrical output predicted is reached at around 260 s (see Figure Figure 53a). By comparison, the full operation of the prototype, identified where all four rows of modules achieve a plateau was attained after 300 s (see Figure 53b). Given the simplifications done, namely regarding the heat capacity, the fact that on the experimental results the prototype is on transient regime, the comparison seems to be acceptable. It has already been said that the reason why the value of the total experimental power then continues to rise has to do with the fact that the existing prototype still does not incorporate an excess vapour condenser and therefore, once the vapour becomes excessive the pressure continues to build-up and so the saturation temperature also continues to grow, inducing a higher excess heat spreading temperature and thus a higher power. However, it may be seen that the maximum total power predicted, around 64 W, is similar to the value achieved experimentally slightly after, at around 400 s.

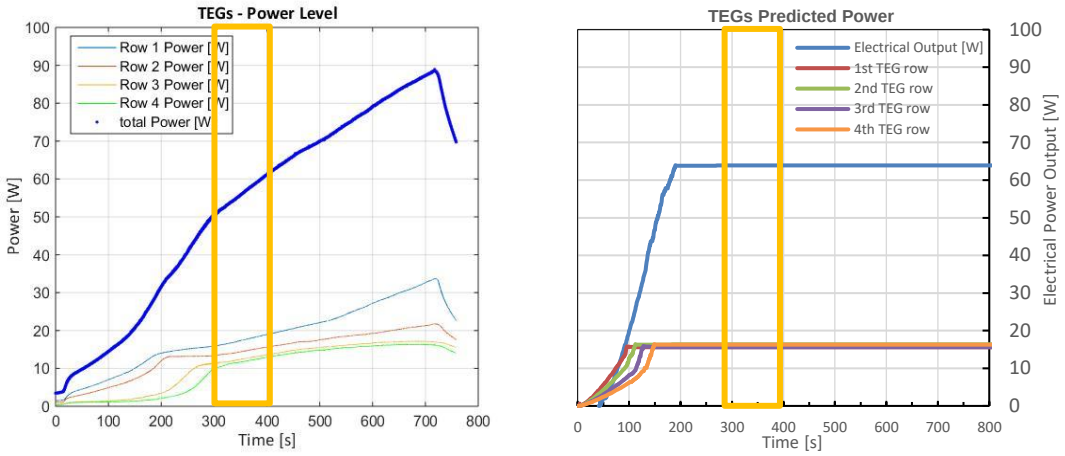

(a) (b)

Figure 56 - Electrical Power output (a) experimental vs (b) predicted for the downsized proof-of-concept TEG operating with an excess heat spreading temperature of 100°C.

Although in the experimental results more time to reach full operation was needed, the heat spreading effect was confirmed for the same TEG Row electrical power values. The results of the electrical power output as well as the efficiency organized as a function of the available exhaust energy or the heat absorbed by TEGs can be seen in Figure 57.

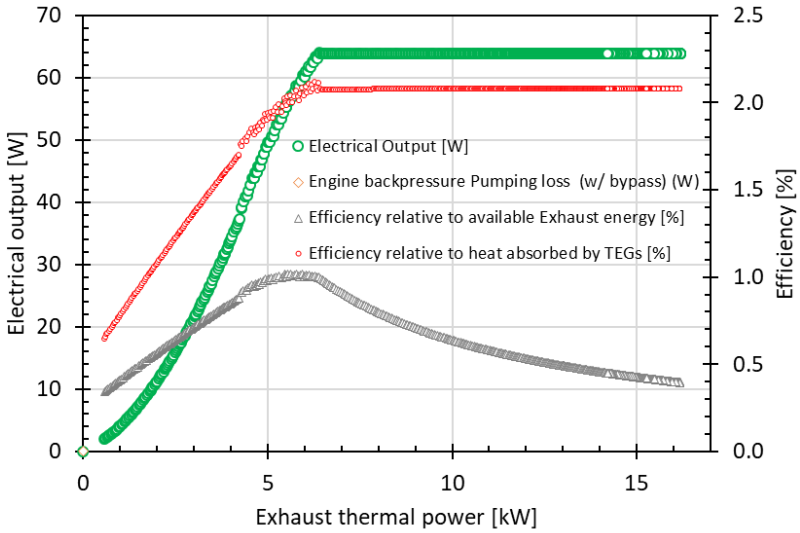

Figure 57 - TEG module's simulation results.

It is possible to see that the maximum value of production for the system is when it reaches the steady-state in which all TEG modules are working with the hot side at the vaporization temperature of the working fluid (which in this case is 100 °C). In this simulation, and for the temperature of 100°C (less than half of the maximum temperature of the modules, 250 °C), the maximum power produced was 64 W. It is also possible to analyse that the maximum efficiency obtained was 2.1%. This value seems reasonable for this low temperature range, in view of the maximum theoretical value being around 5% for T_h=250 °C.

After analysing the power output of the HX as a whole, it is interesting to analyse the behaviour of each row of thermoelectric modules to verify the temperature spread caused by the introduction of heat pipes as a control system for thermal stability along the length of the prototype. In Figure 58, it is possible to see the evolution of the thermoelectric production by each row of modules as a function of the available exhaust power.

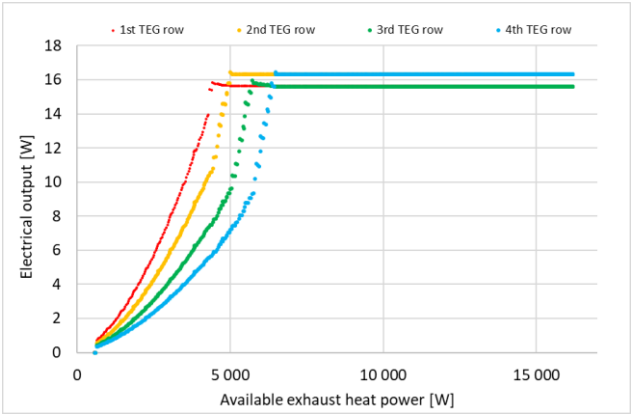

Figure 58 - Electrical output in function of the available exhaust power

It is noteworthy to observe the cascading effect of heat along the length of the HX. As can be seen in Figure 58, when the first row of thermoelectric modules reaches the water vaporization temperature (maximum electric power production), which in this test is 100°C, the working fluid vaporizes and spreads the heat in the form of steam to the following modules (2nd TEG row). The same until the system is completely full and at the maximum possible output for this temperature. Regarding the thermal control once the system is filled with vapour, Figure 58 shows that although the system reaches its maximum production near 6.5kW of available exhaust heat power, beyond that value the power stabilizes, avoiding thermal degradation of the thermoelectric modules as expected.

Table 6 contains some of the values extracted from the thermal simulation performed for the same conditions as obtained in the experimental tests.

Table 6 - Simulation Results for Numerical Validation of the Experimental Test

Parameter	**Value**	**Unit**
Total electrical energy	108.8	kJ
Total Exhaust energy available	23.14	MJ
Total Exhaust energy absorbed by TEGs	5.29	MJ
Total Exhaust energy absorbed by HE	16.65	MJ
Global effectiveness (fraction absorbed by HE)	72%	%
Maximum electric power	**64**	**W**
Average electric power	**60**	**W**
Maximum exhaust thermal power	16.18	kW
Average exhaust thermal power	12.85	kW
Maximum exhaust power absorbed by TEGs	3.01	kW
Maximum exhaust power absorbed by HE	12.27	kW
Electric production	0.11	kWh/100 km
Electric production kJ/km	4.0	kJ/km

It is important to point out that the maximum electrical power obtained in the experimental model corresponds to the moment when the HP is completely filled with water vapour and all TEGs are working at the same temperature, as the electrical power production after that interval should be ignored since this continuous thermal stability feature that was not achieved due to manufacturing problems. This moment can be equated to the maximum power output value obtained in the numerical simulation. In

the experimental test, this moment is registered between 300 and 400 seconds and can be observed in Figure 59.

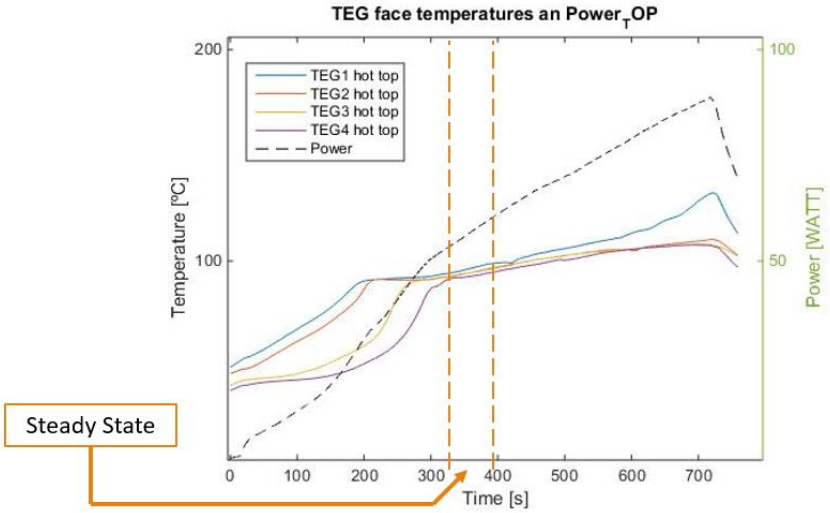

Figure 59 - Steady State representation of Hot face Temperatures and Total Power

For that time interval a maximum power output between 60 and 65 W was registered. These results are in line with those obtained by the mathematical model (see Figure 56) in which the maximum output for these conditions was 64W (see Table 6). Thus, it is possible to state that the mathematical model is validated by the experimental results.

5.3 Predictions for a system operating at 250°C

It is interesting to evaluate what would the performance of the system be if the optimal module temperature (250°C) could be attained. It should be remembered that the prototype built and tested experimentally represents only a quarter of what the final prototype would be. Furthermore, the lack of an excess condenser at the outlet of the heat pipes and the fact that the experimental system had leaks, denote that the results in terms of electrical power production are lower than what could be desired for this novel concept. However, it was possible to validate the mathematical model created and the prototype, making sure that the simulations generated by the software are close to what will be the real electrical power output. Nevertheless, it was not possible to pressurize the system to 40 bar in order to reach 250 °C working fluid vaporization.

For demonstration purposes, a new simulation with the same engine input conditions was made, but this time with the working fluid vaporization temperature of 250 °C. The mathematical model does not require HP's inner pressures inputs, solely the vaporization temperature of the fluid inside the heat pipes is defined. In reality, these would have to be pressurized to a pressure close to ~40 bar considering water as the working fluid. The study of the pressure inside the pipes is only possible by means of an experimental test.

The results of this simulation in the form of the electrical production for each row of TEGs and total electric power output are described in Figure 60 and Figure 61, respectively.

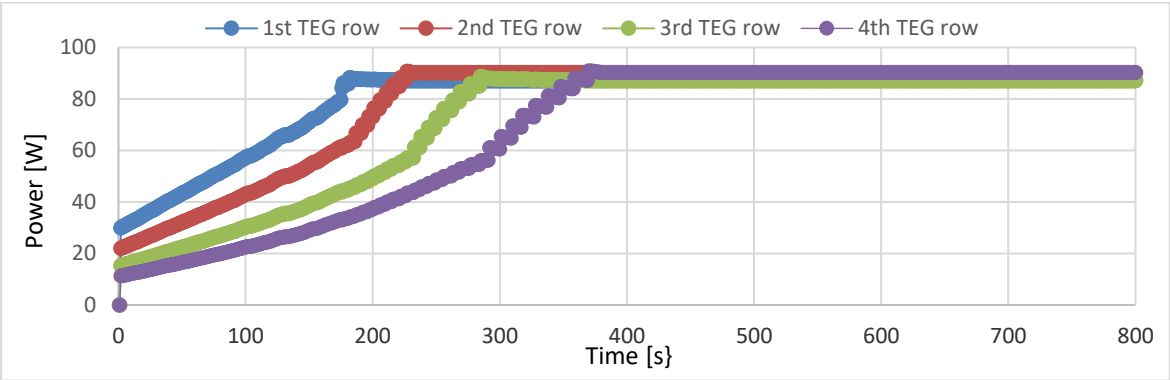

Figure 60 - Electrical power production by each TEG row of simulation for the same test cycle with the working fluid vaporization temperature of 250°C

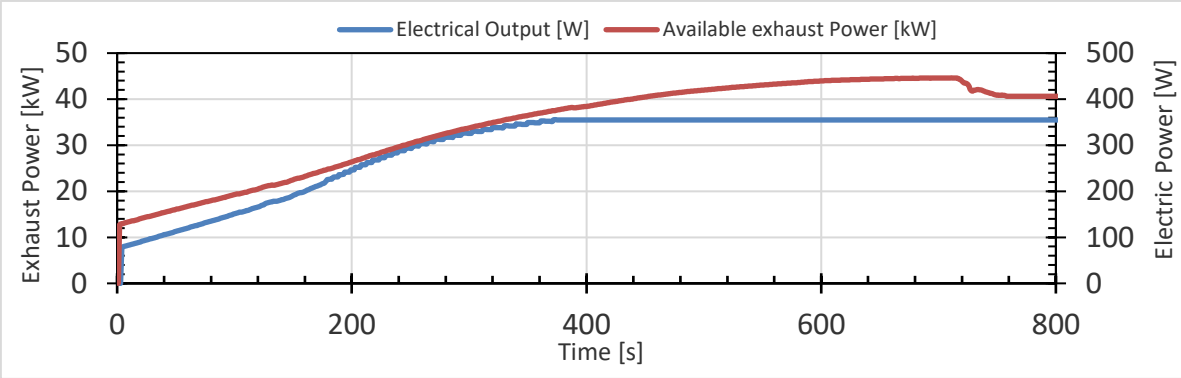

Figure 61 - Electrical Power and Available Exhaust Power results for simulation with working fluid vaporization temperature of 250°C for the same test cycle of the eperimental results

The maximum power output is reached at the thermal stability zone as desired and has a value of around 350 W. As future work will include a prototype that can withstand the pressurization of the heat pipes up to a pressure of 40 bar, which will allow the operating temperature of the modules in thermal stability of 250° C, it is interesting to simulate the operation of this new prototype under high variable thermal loads. For this, some simulations of this new prototype for a standard WTLC cycle are presented in Figure 62.

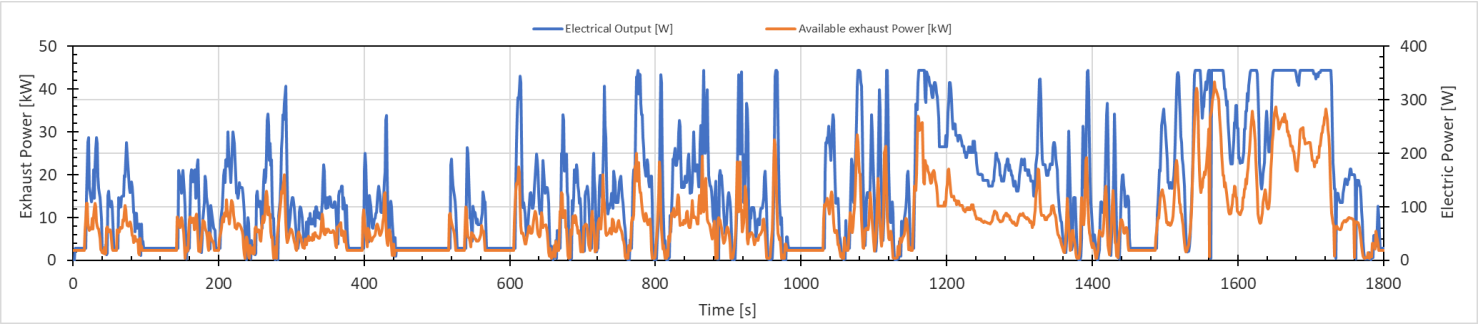

Figure 62 - WTLC Cycle Electrical Power output vs Available exhaust heat simulation results

The maximum achieved electrical power output was once again 350 W and the average value during the cycle was 133 W. Meaning that the system is able to overcome module degradation and maintain thermal stability throughout high variable thermal loads.

If the simulation process is repeated for a final prototype with what would be the final prototype size (four times larger than the concept validation TCTG tested in this work) the following results can be obtained for a WLTC cycle (Table 7).

Table 7 - Simulation results for Full Sized prototype

Parameter	Value	Unit
Total electrical energy	955 146	J
Total Exhaust energy absorbed by TEGs	27 228 617	J
Total Exhaust energy absorbed by HE	28 360 436	J
Maximum electric power	**1,56**	**kW**
Average electric power	**531**	**W**
Maximum exhaust power absorbed by TEGs	34 916	W
Maximum exhaust power absorbed by HE	60 667	W
Electric production kWh/100 km	0,98	kWh/100 km
Electric production kJ/km	35,3	kJ/km

5.4 Fuel and CO_2 Savings

The increasing need for onboard electricity to supply modern vehicle transportation components, such as the air conditioner, digital displays, headlights and tail lights, cockpit ambient lights, sound system are accountable for decreasing the fuel efficiency. This phenomenon results from the fact that onboard electricity comes as a direct result of fuel being consumed within the engine to feed an energy conversion chain [90]. This chain starts with chemical energy stored in the fuel and ends with electrical energy from the alternator. Along the system functioning power losses happen and are associated with every energy conversion process. Even focusing only on the alternator there are several associated losses, such as mechanical losses, electrical losses and magnetic losses. [90] explained that although alternator efficiency varies with speed, load (amps) and electrical power output, commercially available alternator's efficiency range between 50 to 60%. This combined with conversion chain and ICE's efficiency make onboard electricity a significant impact on vehicle fuel consumption.

5.4.1 Compact TCTG Implementation

Although the average electrical power produced by this concept seems to have a relatively low value for light duty vehicles it is important to remember that this is a proof of concept system, with a quarter of the size of the final system and where it was only possible to reach less than half of the hot face temperature of the modules, staging them in underproduction. Using the results obtained in the experimental tests , the fuel consumption and CO_2 emission savings were calculated. In these calculations, the engine power loss due to the back-pressure imposed by the exhaust heat exchanger was not considered.

For this, the bench test ICE's stock alternator specifications were used. All the calculations presented afterwards were made by creating an *Excel* spreadsheet for further prototype studies (see Annex 2). First, with the manufacture's datasheet values for voltage (V) and current (A) the alternator´s power consumption (full-load) was calculated (see Table 8). Then using a mean value for alternator efficiency stated by [90] (55%) and the petrol engine average efficiency of 18% regarding to the average engine efficiency data from the WLTC Driving cycle presented in a recent publication [36], the mechanical power and the fuel power consumption were calculated. It is notable that to produce 1.4 kW of electricity the engine must spent 14.45 kW of fuel power. Also, using the same chain of conversion note that to produce the TEG output (64W) in the alternator it would be necessary to use 646 W of fuel power.

Table 8 - Alternator and TEG output chain of conversion

Parameter	Value	Unit
Alternator Power	1,44	kW
Alternator Mechanical Power (η=55%)	2.62	kW
Alternator Fuel Power (η=18%)	14,45	kW
TEG Output	64	W
TEG Fuel Power (if produced by the Alternator)	646	W

Calculations of the fuel consumption were made using the lower heating value of fuel used (Petrol RON95). The vehicle's mean fuel power during the test performed was calculated using the exhaust mass flow rate of the engine (whose value was previously estimated using MATLAB®). Then it was possible to study the fuel consumption of either the vehicle and the fuel savings of the alternator if the energy was produced by the TCTG (see Table 9).

Table 9 - Vehicle and Alternator Fuel Power savings using TEGs

Parameter	Value	Unit
Vehicle Fuel Power	90	kW
Vehicle Total Fuel Power Consumption	2	g/s
Alternator Total Fuel Power Consumption	0.32	g/s
Alternator Fuel saving Using TEGs	0.014	g/s
Alternator Fuel saving Using TEGs	0.039	l/h

Table 10 presents the fundamental savings obtained by applying the TEG system assuming the mentioned alternator with 55% efficiency for the test conditions performed.

Table 10 - Fuel Power Savings implementing TCTG

Savings	Value	Unit
Alternator Fuel Power Savings using TEGs	4,44%	%
Vehicle Fuel Power Saving using TEGS	0.72	%

In respect to the implementation of this proof-of-concept prototype, the electrical production does not completely replace the alternator specially. This happens because the electrical output of the system is low compared to the alternator full load power, since the maximum achieved TEG module hot face temperature was 100 °C, less than half of the maximum allowed temperature. Also, the size of this system is one quarter of the final proposed system.

Since the results of the mathematical model have been validated with the experimental tests, it is possible to conclude that the simulations performed previously by the research group [36] for a model with final dimensions and hot faces temperature of 250 °C are close to realistic electrical output. The same results pointed out a fuel saving between 4-5% and CO_2 emission savings of around 11-12 g/km depending on the driving cycle conditions (see Table 11).

Table 11 - Savings from using TCTG (Using TEGs GM250-12) [36]

Driving cycle data:	HW	WLTC
Distance [km]	27.1	23.3
Average engine efficiency [%]	25.3%	17.7%
Average required mechanical power [kW]	18.7	8.58
Using TCTG:		
Electric power produced (ave.) [W]	627	267
Energy produced [kJ/km]	26.6	20.7
Average required Mechanical Power [kW]	17.7	7.00
Fuel savings [L/100km / %]	0.50 / 5.4%	0.47 / 4.2%
CO2 emissions savings [g/km]	11.99	11.14

6. NEW PROTOTYPE CONSTRUCTION AND SET UP

At this point, the tests on the existing prototype were completed. The TCTG was tested with the heat pipes working at atmospheric pressure, therefore the working fluid vaporization temperature achieved was 100 °C. Nevertheless, the excess heat spreading feature was confirmed. The construction of a new prototype was planned. This time, overcoming the initial construction difficulties that led to the appearance of leaks in the heat pipes. This chapter reports in detail on the construction work of the final prototype, as well as changes to the design, the methods used and the operation of the system.

6.1 New Design

The new TCTG was based in the existing prototype principle of operation with the addition of some design improvements resulting from the learning made throughout the testing process of the previous prototype. Since the main objective was the construction of a TCTG prototype capable of withstanding high operating pressures (around 40bar), the construction of the part that is associated to this operation was planned and designed in cooperation with a company specialized in industrial boilers and Heat Exchangers, Energest®.

The final design (see Figure 63) was achieved, satisfying the safety concerns of the company as a designer of high-pressure devices and the scientific needs of the research group to have this type of operation specified.

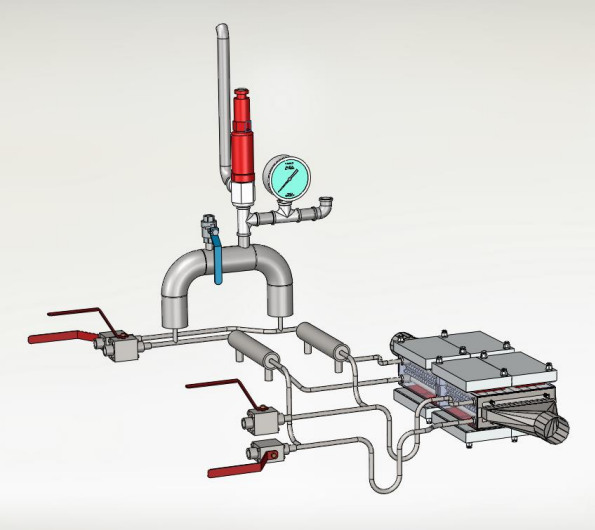

Figure 63 - New prototype design.

6.1.1 New Heat pipes

One of the most relevant changes in this prototype when compared to the previous one was the material of the Heat Pipes. The previous prototype was equipped with copper heat pipes, which were the reason why they did not resisted the aluminium matrix casting process and broke in the most critical areas of their structure.

The new prototype was equipped with stainless steel HPs manufactured specifically for this prototype with welding made by specialised personnel, capable of withstanding both the temperatures of the aluminium matrix casting process and the pressure range of operation. The new HPs can be seen in Figure 64. A copper fabric was added to the interior of the pipes in order to provide the wick structure needed for the capillary pumping effect.

Figure 64 - (a) CAD model and (b) built stainless-steel Heat Pipes.

6.1.2 Corrugated Pipes

The exhaust gases circulate in the Corrugated pipes and exchange heat along their length. This technology can be found also in EGR (Exhaust Gas Recirculation) coolers, in order to rapidly reduce the temperature of the hot exhaust gases [91]. The corrugated pipes were manufactured by BorgWarner® and its configuration was designed specifically for this prototype (see Figure 65).

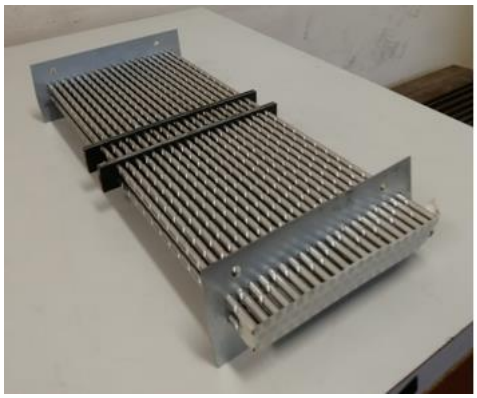

Figure 65 - Corrugated Pipes.

Some positioners were placed in the corrugated pipes to position the heat pipes inside the moulding box for casting the aluminium, but also for the creation of the separation/discontinuity zone of the aluminium matrix, discussed previously in chapter 3.1. The spacing between the tubes was the same used in the existing prototype, which was optimized for minimizing thermal resistance and pressure drop, as published in a paper of the group.

6.2 New TCTG Construction

6.2.1 Casting Process

The moulding box for the aluminium casting was prepared. This box created the aluminium body that promotes the heat transfer between the corrugated tubes, the heat pipes and the hot faces of the TEG modules. The moulding box was designed to position the corrugated pipes and the heat pipes at the desired position in order to properly cast the aluminium. Figure 66 displays the CAD drawing of the set.

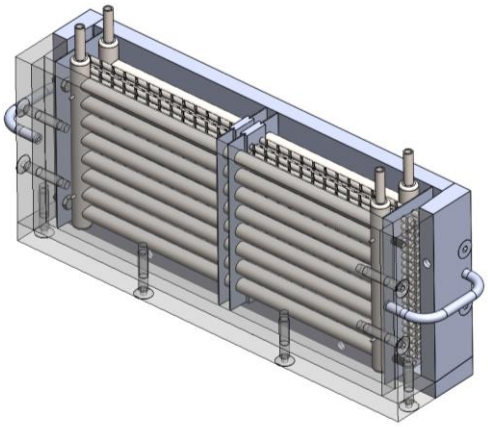

Figure 66 - CAD drawing of the moulding box.

The process of building this new prototype began with the construction of its body. For this, the corrugated tubes and the HPs inside the moulding box were positioned for subsequent casting of the aluminium. In Figure 67 it is possible to see the positioning of the corrugated tubes and their centring with the moulding box.

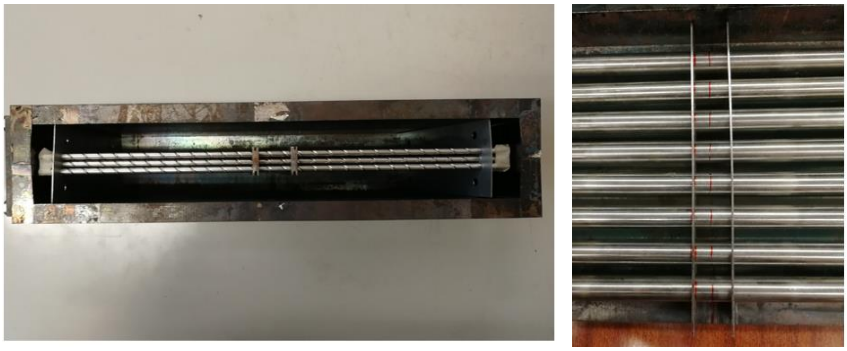

Figure 67 - (a) Moulding Box and (b) Heat Pipe positioning inside the moulding box.

It was necessary to ensure that during the casting process, the positioners placed on the new HPs prevent the aluminum casting from filling unwanted regions. A thermal silicone paste, capable of withstanding 1400°C, was applied to the HPs so as not to suffer any damage due to the high temperatures of the casting process. The openings between the positioners and the heat pipes were then sealed as shown in Figure 68b.

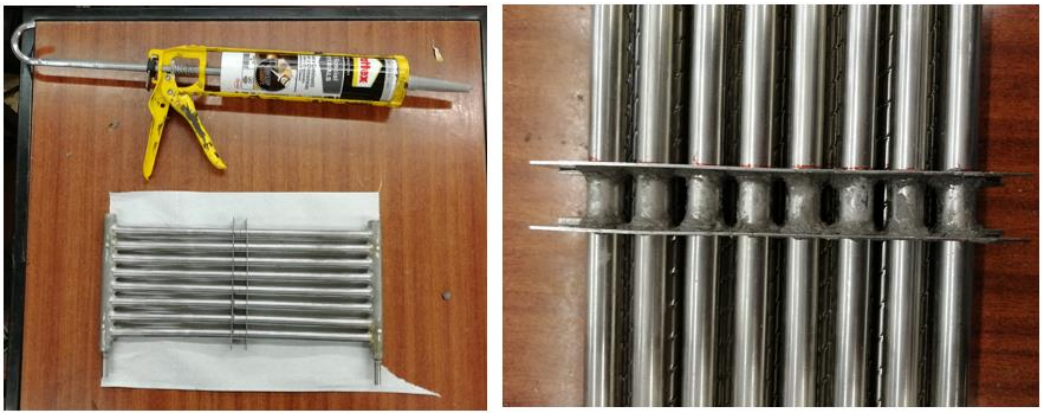

Figure 68 - (a) high temperature silicone and (b) after application on positioners.

Next, the corrugated tubes and the heat pipes were placed inside the moulding box. The design of this TCTG required the creation of three areas that could not be contaminated by aluminium: the area of discontinuity mentioned above, and the two ends of the corrugated tubes. Therefore, these areas were coated with fine silica sand. Figure 69a shows the closed moulding box with the three specified zones where the aluminium must not enter as well as the preparation of the special sand that was used. Next, Figure 69b shows the respective areas already covered with compressed sand. Finally, Figure 69c shows in detail the future discontinuity zone of the aluminium matrix.

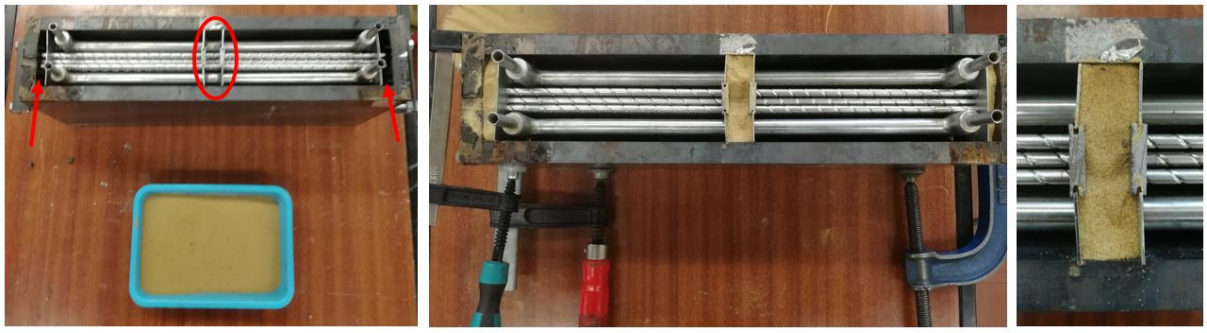

Figure 69 - Moulding Box (a) before and (b) after the sand application and (c) close up of the discontinuity zone

After the moulding box preparation was complete, the aluminium casting and casting process started. First, the moulding box containing the HPs and the corrugated tubes was placed in the muffle furnace. The purpose of this machine is to heat the box so that the aluminium does not cool down abruptly when it is cast. The moulding box was placed inside the muffle furnace at 350 °C for 1 hour. The muffle furnace used as well as its display are shown in Figure 70.

Figure 70 - (a) Muffle Furnace and (b) digital display.

At the same time as the moulding box was in the muffle furnace, the aluminium ingot was placed in the furnace to melt. The ingot used was an aluminium AlSi12 alloy, due to its high silicon content this alloy has a high fluidity, which will be important due regarding the small size of the cavities it has to fill when cast. Its thermal conductivity is around 120 W/m.K.

The ingot was cast inside the furnace at 720 °C and after 30 minutes of verification of complete melt the alloy was de-gazified for 20 minutes using argon gas. The alloy was then refined and modified with titanium-bor aluminium and strontium aluminium for 20 minutes. The furnace and the de-gasification process are presented in Figure 71.

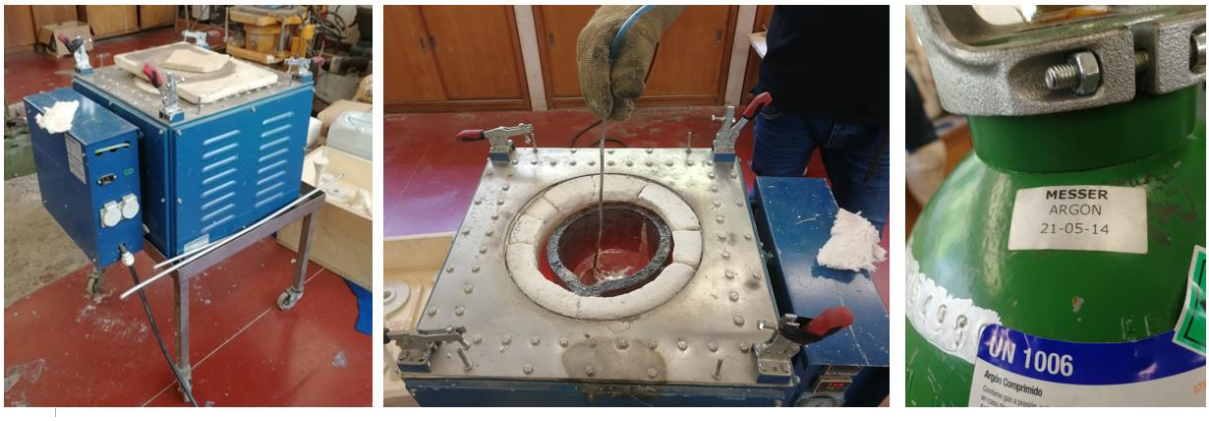

Figure 71 - (a) Melting Furnace, (b) de-gasification of the alloy using (c) Argon.

After the aluminium casting process in the furnace was completed and the pre-set time for preheating the moulding box in the muffle had elapsed, the moulding box cointaing the HPs and corrugated pipes was removed. Figure 72 shows the moulding box exiting the muffle.

Figure 72 - Moulding box exiting the Muffle Furnace.

The aluminium in the furnace was then cooled down to 700°C and cast under mechanical vibration to facilitate the casting process considering the geometrical complexity of the various cavities of the piece (see Figure 73).

Figure 73 - Moulding Box placement for aluminium cast.

After confirming that there were no apparent external leaks (see Figure 74), the alluminium casting process was deemed to have been successfully completed.

Figure 74 - (a), (c) side-view and (b) top-view of the moulding box after alluminium casting

Then the freshly cast HX and the moulding box were removed from the vibration machine for further cooling. At this moment it was possible to verify that the clamps that stabilized the piece interfered with the aluminium casting (see Figure 75) . Also, it is possible to see that the leakage level of the aluminium exceeded the level in which the supports were placed, causing a deformation in the aluminium. However, after an evaluation with those involved in the project, it was concluded that this deformation will not interfere with the heat transfer phenomena inherent to the operation of the prototype.

Figure 75 - Problems found after the casting.

After the cooling time had elapsed the moulding box was opened and the final result of the procedure was analysed. In Figure 76 it is possible to see the extraction of the moulding box.

Figure 76 - (a) Moulding Box extraction and cooling (b) inside and (c) outside.

The piece was cleaned and the silicon sand present in the compartments where the aluminium was not intended to leak was removed. Figure 77 displays the cleaning process of the previously casted TCTG.

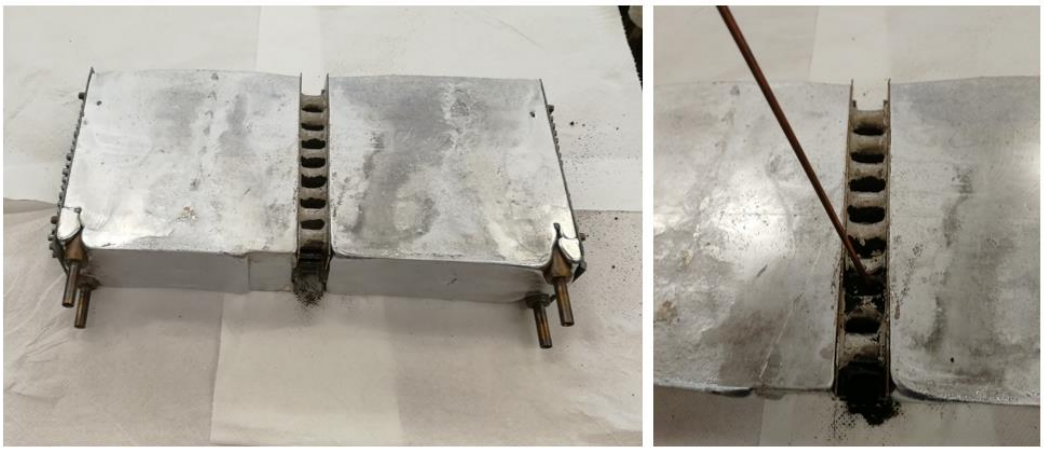

Figure 77 - (a) HX being cleaned and (b) sand being removed.

In order to remove any impurities that had lodged in during the casting process, the inside of the corrugated tubes and Heat Pipes was cleaned with a compressed air gun. Figure 78 shows the sides of the prototype where it can be seen that the ends of the corrugated tubes are intact as well as the screws that were introduced in the lateral positioners for posterior placement of the intake and exhaust gas manifolds/collectors (marked in red).

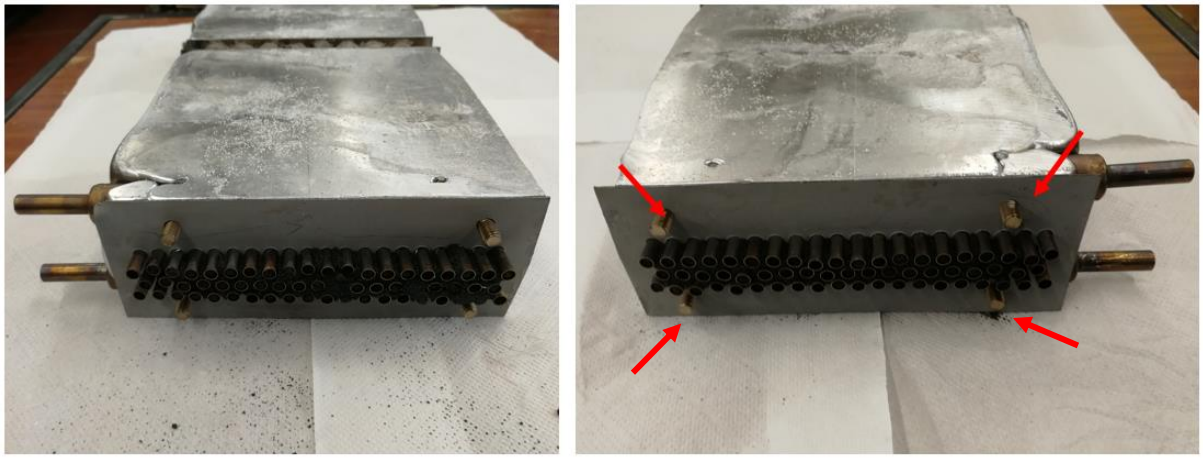

Figure 78 - Verification of the integrity of the end of the corrugated tubes and screws

At this point the casting process of the aluminium matrix, the rigid body of the TCTG was completed. The weight of the prototype with the aluminium matrix, the HPs and the corrugated tubes is 9.105 kg (see Figure 79).

Figure 79 - Weighted TCTG after casting

6.2.2 Machining Process

It was concluded that the aluminium upper and lower surfaces of the TCTG (where the TEGs will be placed) had a high and irregular roughness. This interferes with the contact resistance between the aluminium matrix and the TEG module, degrading its performance. Hence, to reduce the contact resistance between the TEG and the HX, theses surfaces were machined.

For this process a 6-pad milling cutter tool with a diameter of 80 mm (see Figure 80a) with a main spindle rotation speed of 1100 rpm was used. The formula to calculate the cut speed is as follows:

$$v_c = \frac{\pi \cdot D_1 \cdot n}{1000} \tag{36}$$

With the parameters used in the machining process, the cutting speed was 276.3 m/min.

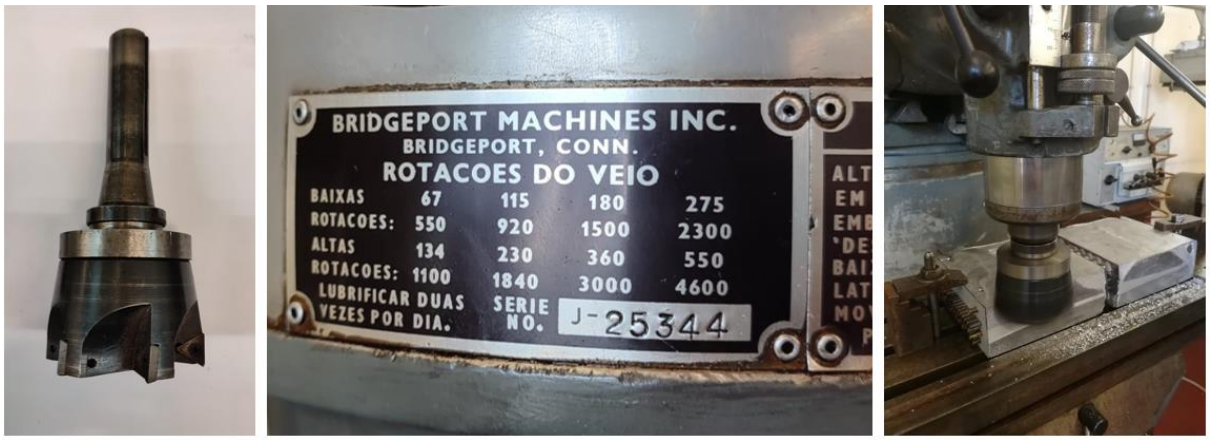

Figure 80 - (a) 6 pad milling cutter tool, (b) milling machine manufacture spindle rotation speeds and (c) machining process of the HX

To obtain a surface with the lowest possible roughness, the TCTG was then sanded using water-based abrasives with varying grain diameters, from larger to smaller.

The next step in the prototype built was the construction and implementation of the HPs outer path. This process was in charge of ENERGEST®, one of the partners in this project. The final design main challenge was to find a compromise between making the most compact prototype possible and finding components that would safely meet the pressure specifications. Figure 81 shows some preliminary models of the prototypes discussed with the company.

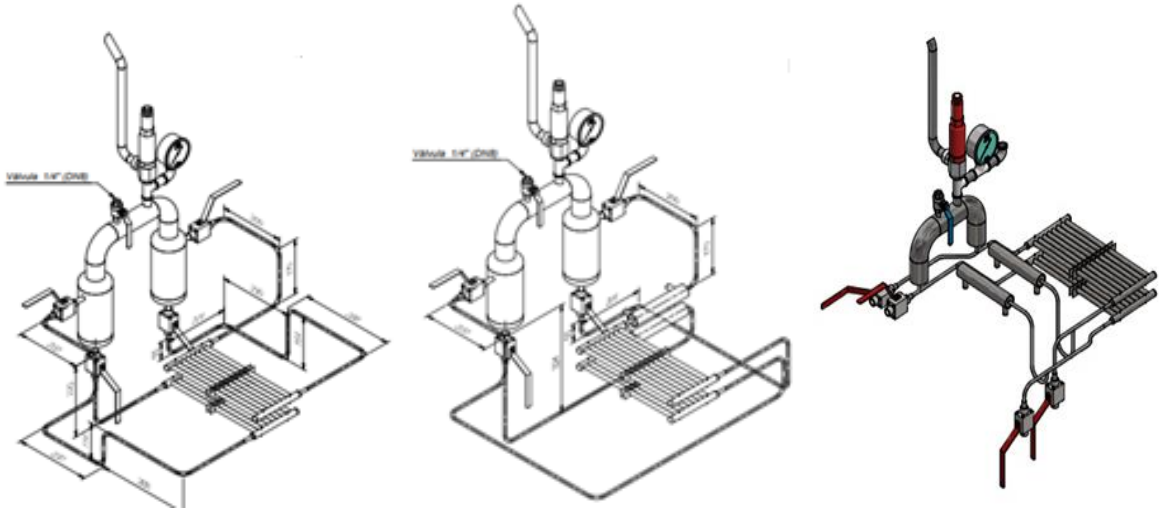

Figure 81 - Preliminary Models of the final prototype.

The design of what would be the final project began to compose itself and the final design of the work to be carried out by ENERGEST is presented in Figure 82. These components were dimensioned according to the pressure and temperature range of use.

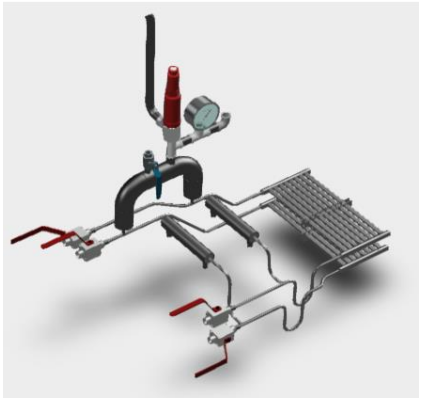

Figure 82 - Final design of the Prototype.

The final design of the prototype assembled and delivered by ENERGEST® can be seen in Figure 83.

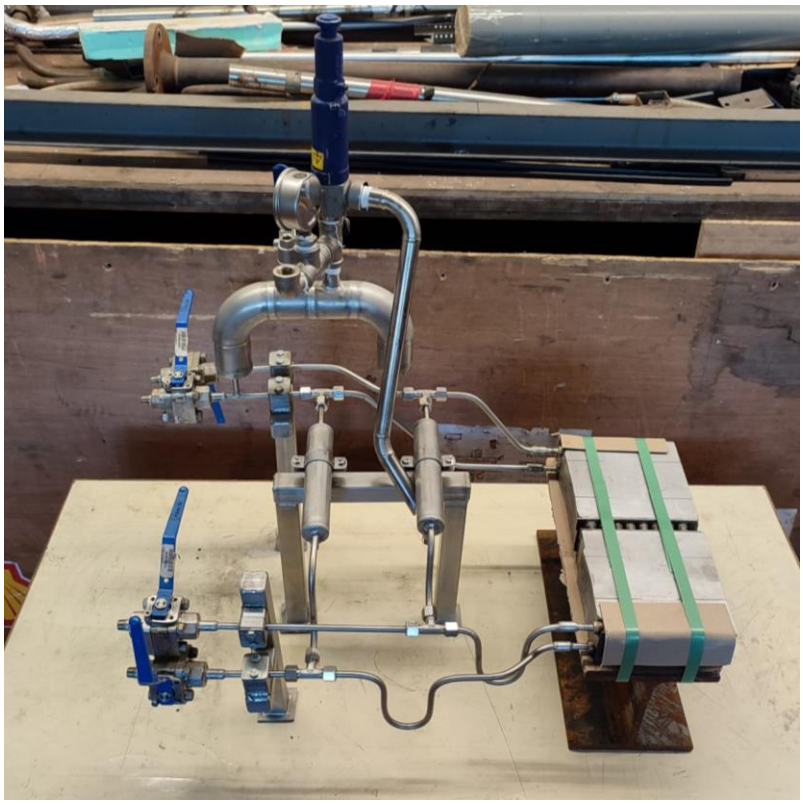

Figure 83 - Prototype delivered by ENERGEST.

6.2.3 Excess Vapour Condenser

The excess vapour condensers are intended to prevent the pressure build-up of the system due to excess vapour production. They guarantee that the temperature of the hot faces of the module never exceeds the maximum allowed temperature while promoting pressure stability inside the system.

These consist of a water-cooled sleeve that covers a part of the pipes that are an extension of the HPs inside the system. In case vapour pours out of the aluminium body, it will condense it and prevent excess vapour in the system.

The temperature difference between the outlet and inlet water cooling the excess condensers is measured so that it is possible to quantify the excess vapour condensed. Figure 84 shows the position of the excess condensers in the system, as well as a close-up view of the cooling water entrance and exit.

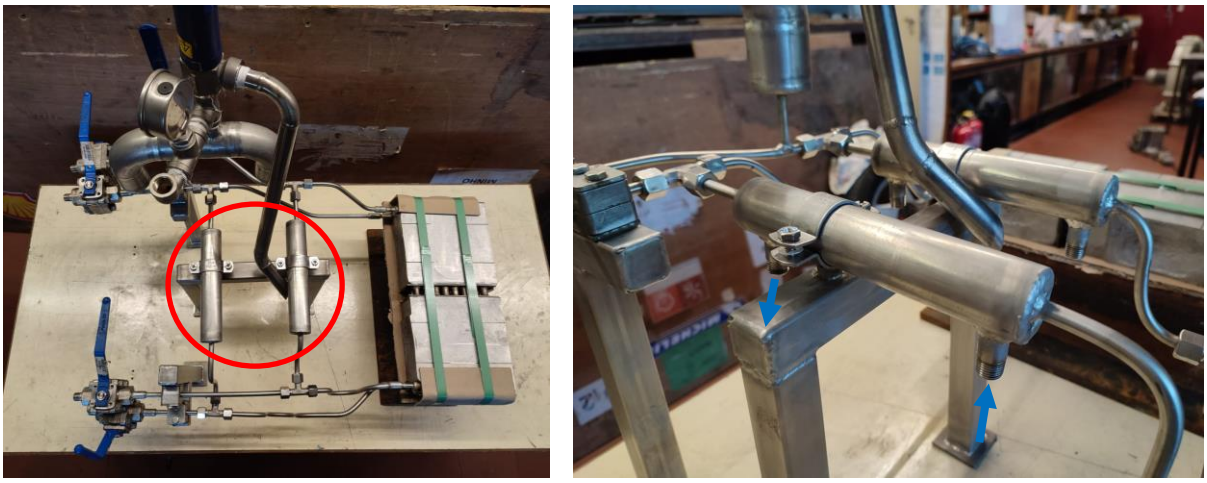

Figure 84 - (a) Excess condensers positioning and (b) close up view.

6.2.4 Relief Valve

For pressure control stability and safety reasons, a relief valve was added to the highest part of the prototype. Figure 85a shows the expansion valve placement in the TCTG above the expansion vessel. It was designed to be connected to both upper and bottom HP system and dimensioned to withstand the TCTG inner HP's pressure during high thermal load events. It is activated at 60 bar, preventing the system from exceeding pressures that may jeopardise its structural integrity. This valve is a SAFE-TCP 960 Series and can be seen in Figure 85b.

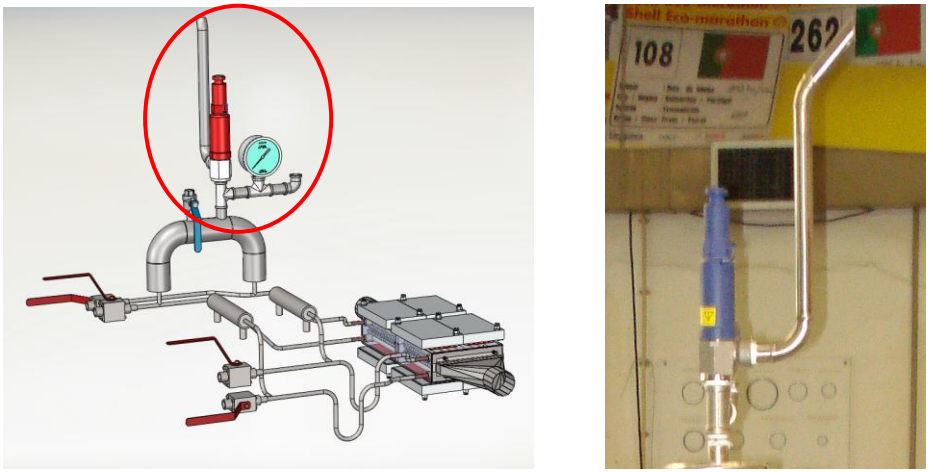

Figure 85 - Expansion Valve.

The relief valve manufacture datasheet can be found in Appendix 2 – Security Valve Datasheet.

6.2.5 TEGs and Cooling Plates placement

Next, the TEGs were prepared for placement in the HX (see Figure 86a). Since these are the same ones that were used in the first prototype, they were individually tested to ensure their proper functioning

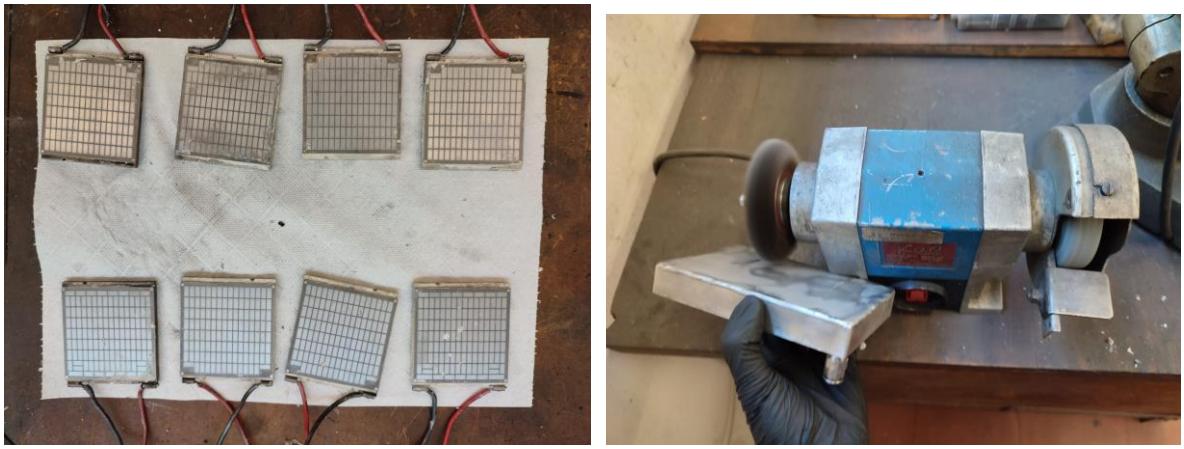

Figure 86 - (a) TEG preparation and (b) cooling plate cleaning.

The cooling plates were also cleaned and prepared for fitting to the new prototype. For that an electric bench polisher was used (see Figure 86). To minimize thermal contact resistances the HX was coated with the same thermal paste used in the first prototype (recall Figure 34a). The TEG modules were placed on top of this paste. Thin alumina sheets were also placed between the TEGs to provide electrical insulation with a low thermal resistance, the HX and the cooling plates. In Figure 87 it is possible to see the placement of the TEGs and in Figure 87b the alumina sheets.

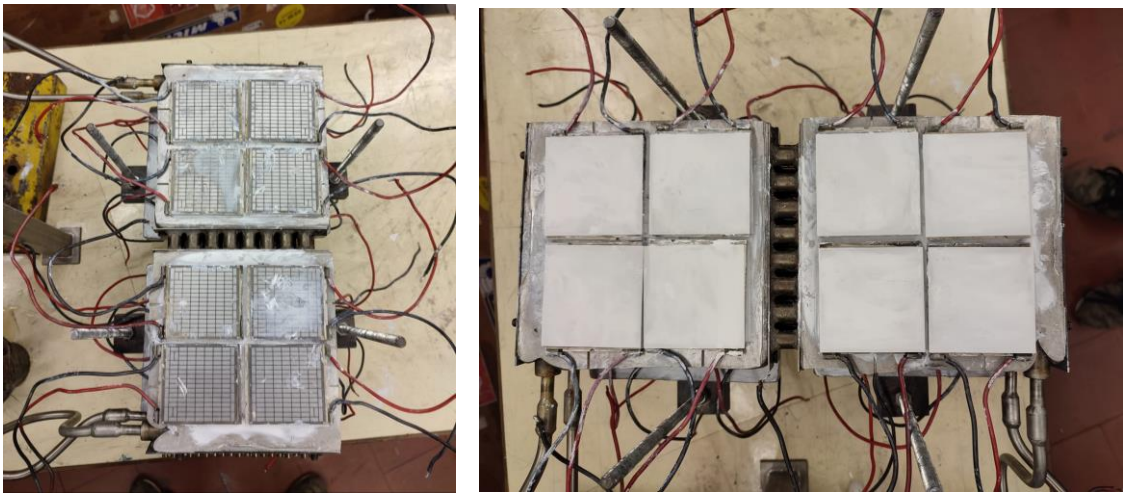

(a) (b)

Figure 87 - (a) TEG placement on the HX and (b) alumina sheets covering

The TCTG prototype after the assembly of the TEGs and the Cooling Plates can be seen in Figure 88.

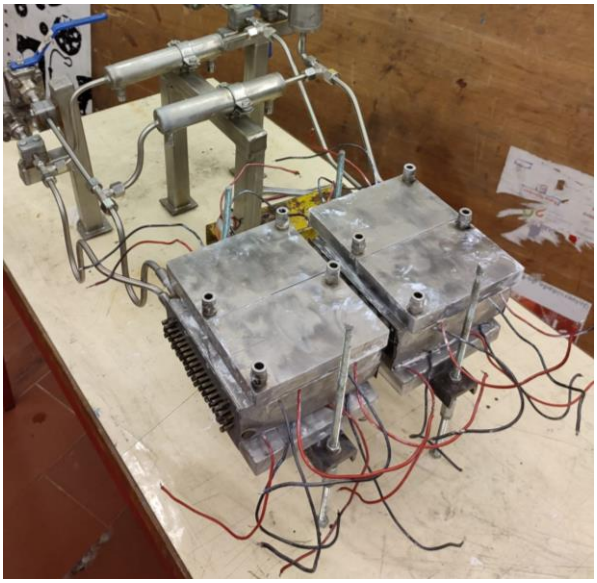

Figure 88 - Prototype after the assembly of the TEGs and the Cooling Plates

6.3 System Set-up

The main components of the system were built, lacking only the assembly of everything so that the system would be ready for testing.

All the connections between the TEGs and the load resistors were made and connected to the previously built “custom box” for connection with the data acquisition plug (see Figure 89).

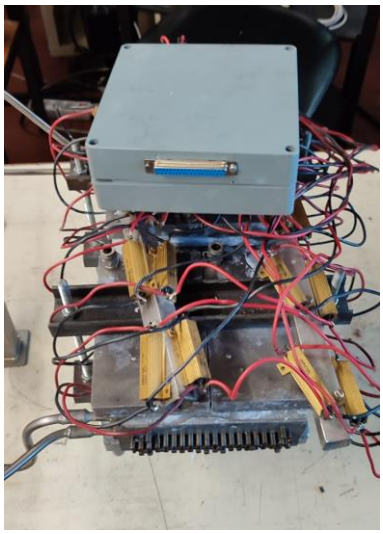

Figure 89 - Prototype after load resistance connected to the TEGs

The exhaust gas collectors were fitted to the prototype. Figure 90b shows that they were sealed with high-temperature silicone to prevent any exhaust gases leakage (highlighted in red).

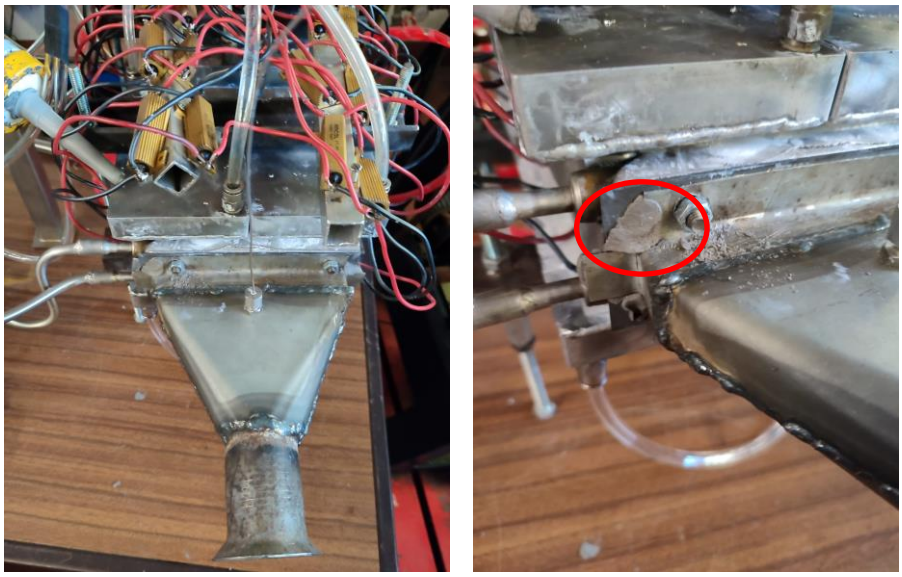

(a) (b)

Figure 90 - (a) Exhaust Gas Collector and (b) possible leakage sealing.

The water system pipes from the cooling plates (in red) as well as those of the new excess condensers (in black) were connected to the system (see Figure 91).

Figure 91 - Water supply system connections.

The exhaust pipe coming from the engine was connected and the exhaust manifolds, both inlet and outlet were covered with glass wool and a film of refractory tape to thermally insulate these parts (see Figure 92).

(a) (b)

Figure 92 - (a) Exhaust gas collector connected to exhaust pipe and (b) coated with glass wool.

All thermocouples, pressure sensors and load resistors were connected to the data acquisition system. This connection is described in detail in chapter 4.1.4.

6.3.1 Exhaust Collectors

The exhaust manifolds/collectors for the inlet and outlet of the HX were built. Stainless steel was used for this piece. It was firstly designed using *SolidWorks*® *SheetMetal* to obtain the necessary bends, to achieve the desired form. Then, it was cut and bent in order to obtain the final shape. Finally, it was MIG-welded. The CAD drawing and the built collector are displayed in Figure 93.

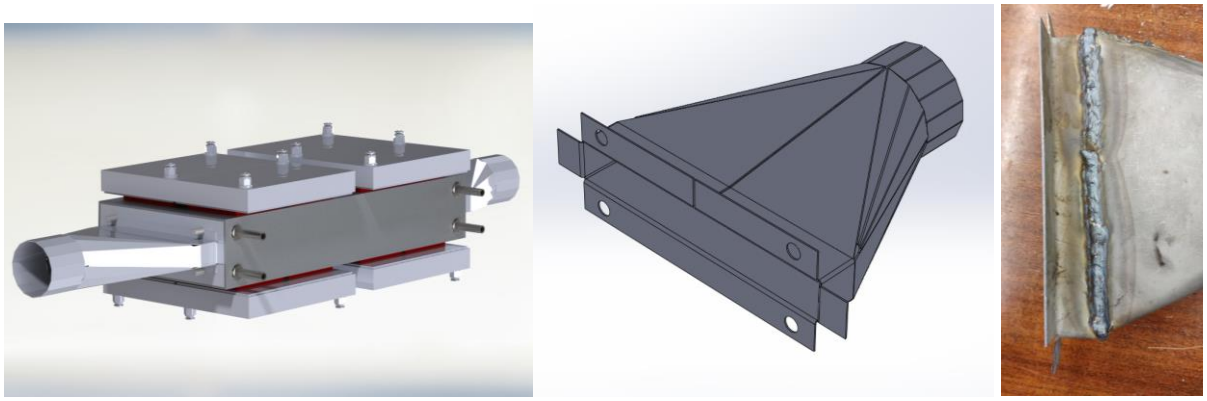

(a) (b) (c)

Figure 93 - (a)Exhaust Gas Collectors position in TCT;(b) Exhaust Collectors Sheet Metal Drawing, (b) MIG Welding on exhaust collectors and (c) junctions to connect the exhaust pipe.

6.4 Brake Dynamometer

In order for the engine to produce torque and generate the maximum possible heat it is necessary to simulate a mechanical load to the engine. The dynamometer brake consists of a rotor connected to the engine, a stator supported on bearings which is fixed by a load cell placed at a known distance to the axis of rotation (d), where the load cell measures a force which is being exerted to keep the stator stationary (f). The torque is obtained by multiplying f by d as shown in Figure 94.

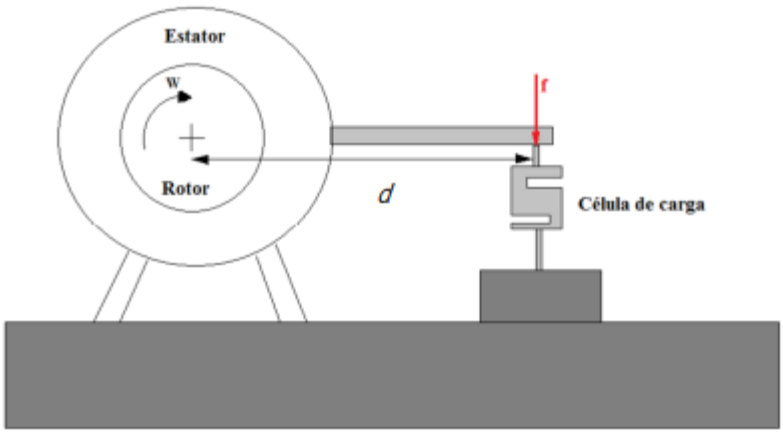

Figure 94 - Dynamometric brake Scheme [92].

The brake dynamometer available in the laboratory was used for this purpose. It is an electric dynamometer working on the Eddy currents principle. A throttle was used to control the engine load as the control variable. The dynamometer was linked to a digital readout system which contains the digital RPM meter. In Figure 95 it is possible to see the break dynamometer complete system.

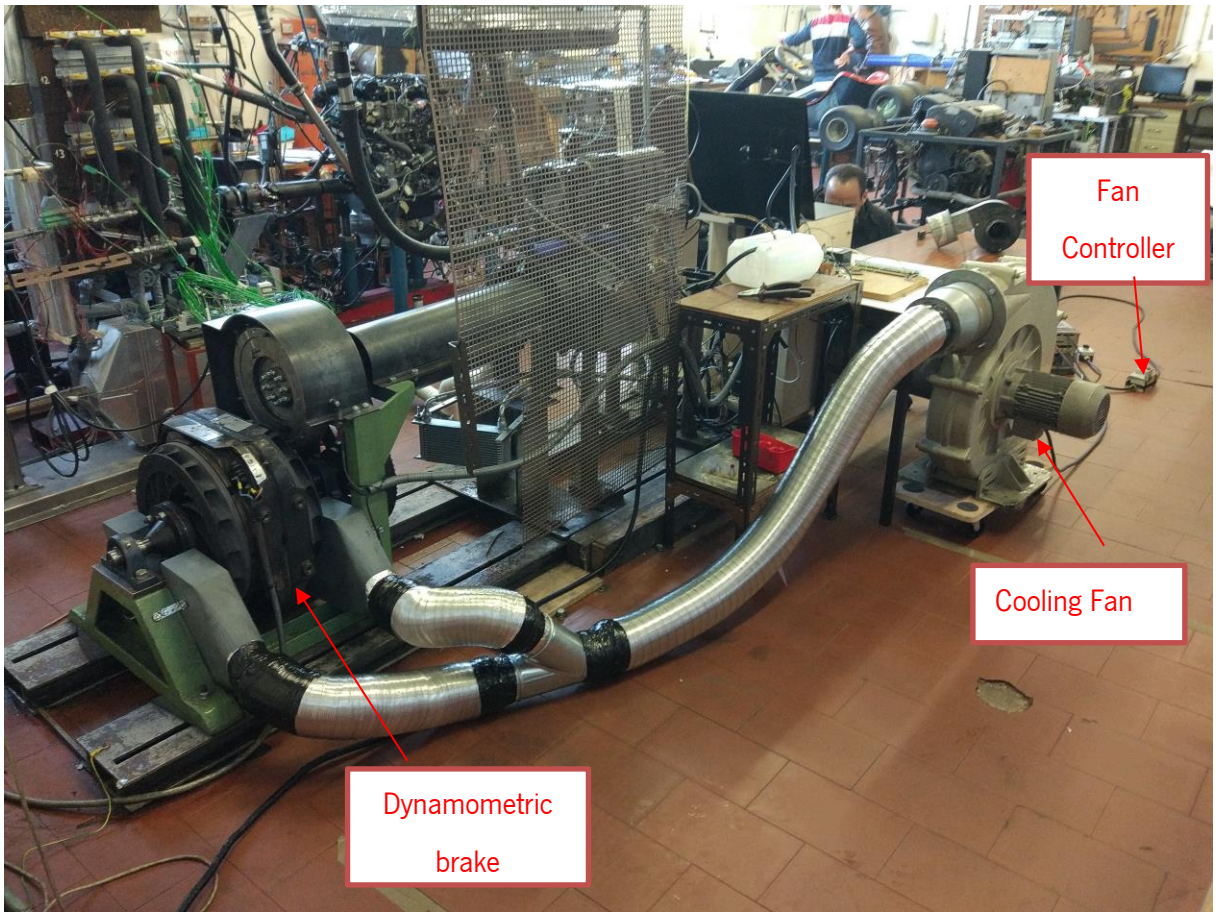

Figure 95 - Brake Dynamometer system.

The cooling fan has the role of reducing the temperature of the brake during its operation, preventing it from reaching temperatures that may damage its internal components. This system was not used in the first prototype because the electronic controller was missing. Thus, considering the importance of this feature, a controller was developed for the project. Figure 96 displays the controller.

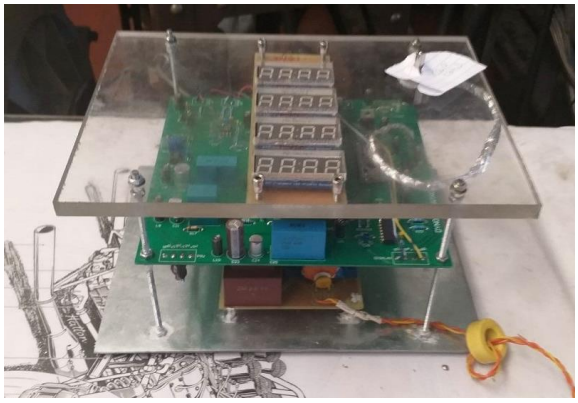

Figure 96 - Dynamometer Brake Controller.

This controller enables a set rpm to be defined for the engine so that, regardless of the position of the throttle, the brake locks the engine, maintaining the same engine speed, producing more or less torque. The controller is equipped with a display zone that allows the user to check the set rpm, the real rpm and the torque produced.

6.4.1 Calibration

A calibration of the brake was also necessary as the values shown by the display were not in conformity with reality. For that, several weights with known masses were placed on an arm centred on the brake rotation axis (see Figure 97). The values presented on the display were noted.

Figure 97 - Dynamometric Brake Calibration Procedure.

The moments of inertia of the arm were previously calculated to make a calibration curve that states the real torque value for each corresponding value that appeared on the display by the time of calibration (see Figure 98).

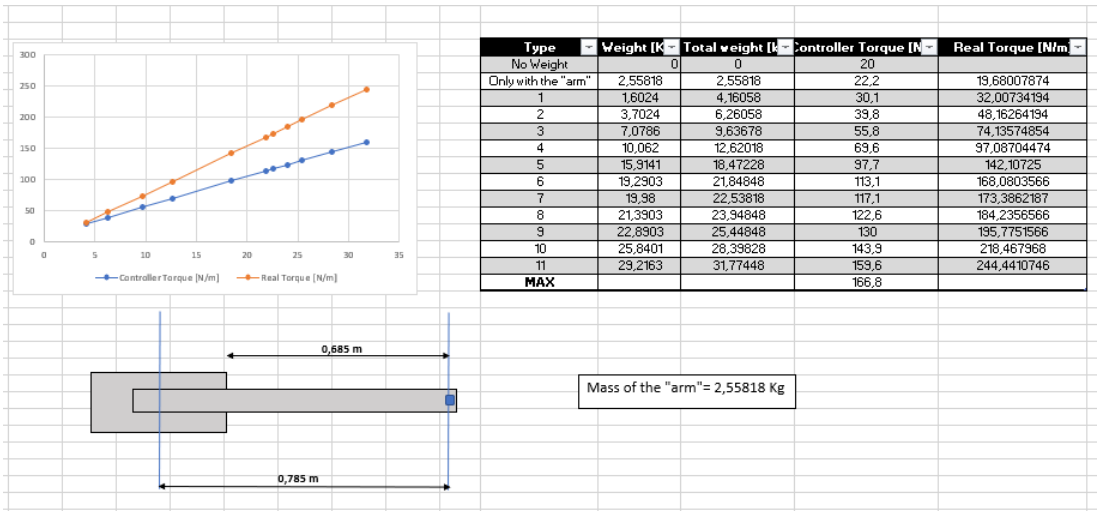

Type	Weight [K	Total weight [k	Controller Torque [N	Real Torque [N/m]
No Weight	0	0	20	
Only with the "arm"	2,55818	2,55818	22,2	19,68007874
1	1,6024	4,16058	30,1	32,00734194
2	3,7024	6,26058	39,8	48,16264194
3	7,0786	9,63678	55,8	74,13574854
4	10,062	12,62018	69,6	97,08704474
5	15,3141	18,47228	97,7	142,10725
6	19,2903	21,84848	113,1	168,0803566
7	19,98	22,53818	117,1	173,3862187
8	21,3903	23,94848	122,6	184,2356566
9	22,8903	25,44848	130	195,7751566
10	25,8401	28,39828	143,9	218,467968
11	29,2163	31,77448	159,6	244,4410746
MAX			166,8	

Figure 98 - Calibration Sheet for the Brake Dynamometer.

This calibration enabled to determine the real torque values produced by the engine during the test cycle of the experimental test performed.

.

7. RESULTS AND VALIDATION OF THE NEW PROTOTYPE

7.1 Engine

In Figure 99a, it is possible to see the evolution of engine speed (in RPM) throughout the final test, as recorded by the ECUMaster® software. The test consisted of one engine stage, in which the engine rpm was pre-set at 2200 rpm. In this final test, braking torque was applied to the engine using the brake dynamometer. The applied load values are visible in Figure 99b- 142.7N.m. As explained in chapter 6.4.1, the value shown on the display is different from the real binary applied. For this, using the calibration curve, it is known that the actual torque applied to the engine was around 215 N.m. To calculate the power produced by the engine at this speed the following formula can be applied:

$$P = T.S \tag{37}$$

$P - Power\ [W]$

$T - Torque\ [N.m]$

$S - Engine\ speed\ [rpm]$

Using the real applied torque value of 215 N.m and the engine speed of 2200 rpm the value for the engine power is 45 kW (or around 50 hp).

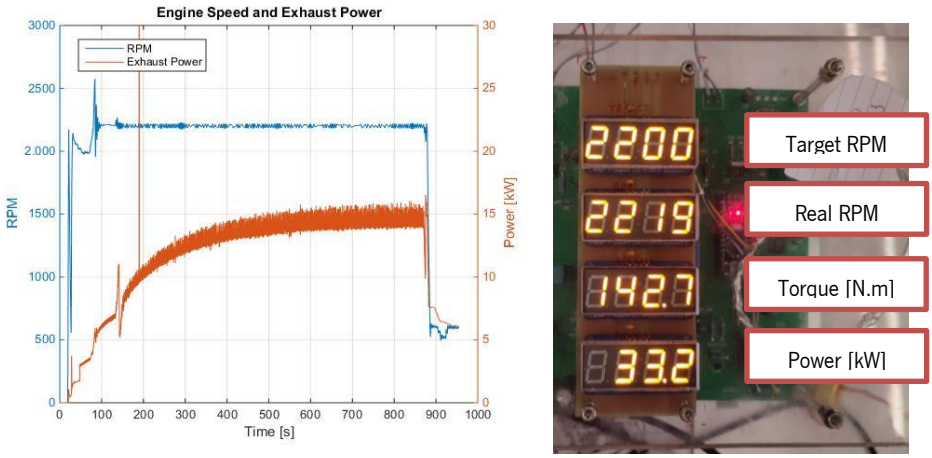

(a) (b)

Figure 99 - (a) Engine RPMs and Available Exhaust Thermal Power throughout the final test cycle and (b) Engine/dynamometer brake parameters.

7.1.1 Heat Exchanger Effectiveness

Figure 100 displays the exhaust gas temperature at the inlet and at the outlet of the system. It can be seen that the exhaust temperature topped at roughly 600 °C at the end of the test. There, one can also see that the temperature of the outlet exhaust gases is much lower than the temperature of the inlet exhaust gases. This temperature differential and the exhaust flow rate are the parameters that yield the heat absorbed by the system. The HX effectiveness, $\in$, can also be seen in this figure and is calculated from eq. (12) Once again it can be seen that the closer the outlet temperature is from the heat sink temperature (water inlet temperature), the closer from 100% will $\in$ be. Similar to what happened in the first test, the effectiveness starts high (this phenomenon is explained in chapter 5.1.2), eventually reaching a stable value around 600 seconds of about 60%.

These effectiveness values seem rather high, nonetheless, indicating a good heat absorbing capacity of the prototype without the risk of overheating. but lower than those found in the first prototype. This can be due to the different material of the heat pipes. In the first prototype the HP were made of copper while these are made of stainless steel.

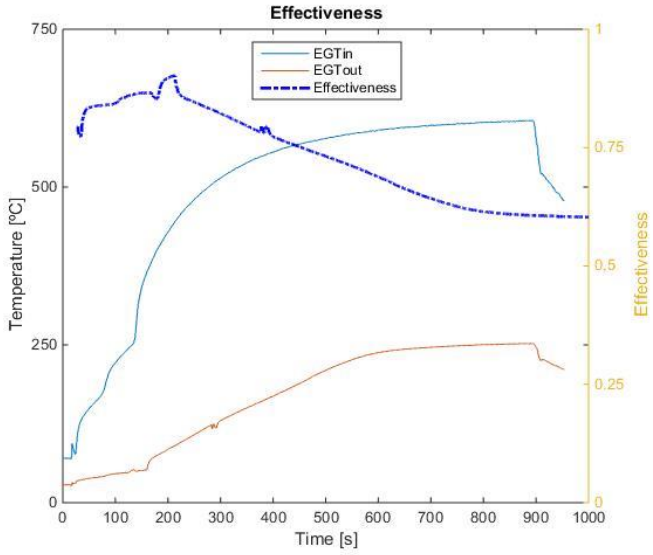

Figure 100 - Exhaust inlet and outlet gas temperature and HE Effectiveness (Final Test).

7.1.2 Temperature Analyses

Figure 101a illustrates the excess heat spreading feature. This figure displays the hot face temperatures of each row of TEGs, starting with Row 1, the first, more upstream row, and ending with Row 4, the last, more downstream row. Once again, it is noteworthy that the aluminium block has been divided in two separate blocks with an air gap between them. The effect of this division can be seen in Figure 26a. Only the corrugated pipes and HPs cross this air gap and are connecting both blocks. This way, Row 1 and 2 are attached to the upstream block, while Row 3 and 4 are attached to the downstream block.

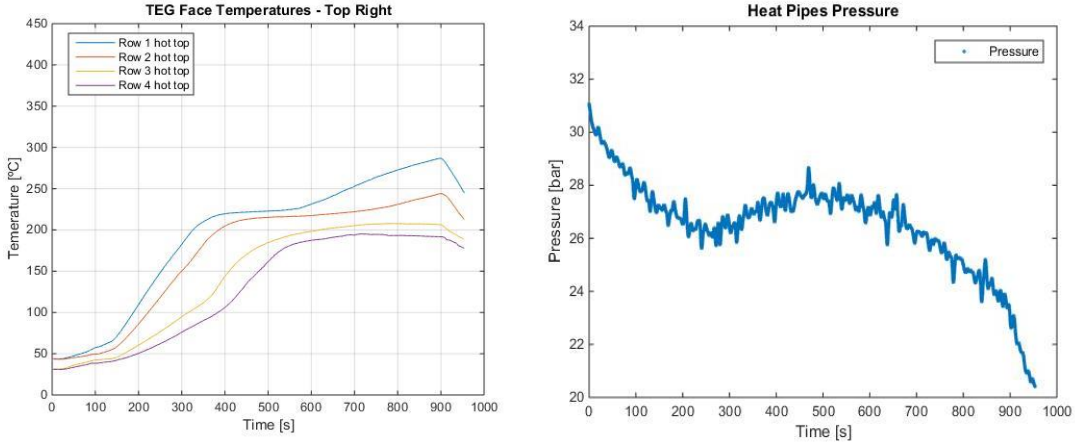

a) b)

Figure 101 - a) Hot face temperature at each row of TEGs (top) and (b) Heat Pipe inner pressure Evolution.

An important factor to highlight is that as soon as the system was pressurised, it was possible to notice that there was a problem with the safety valve, which was leaking. Although the leak was small, it was noticeable when analysing the pressure recorded by the digital pressure sensor connected to the system. This pressure drop can be seen in the Figure 101b. It is noticeable that when the test started the system was at 31 bar and ended up at 20 bar. Unfortunately, it was not possible to solve this problem and repeat the test due to time restrictions.

The important phenomenon that can be observed in Figure 101a is that once the temperature stabilizes, around 400 s, at the TEG rows attached to the upstream aluminium block (Row 1, Row 2), the temperature at the TEG rows attached to the downstream aluminium block (Row 3, Row 4) immediately start increasing, until all TEG rows reach a similar temperature stability level shortly after 600 s. Given that the two aluminium blocks have an air gap between them, this means that there is no relevant heat conduction between them. Therefore, the temperature rise that one block seems to cause on the other block should necessarily be caused by the excess heat spreading caused by the HPs, that is, the heat

absorbed by phase change at the upstream block is being effectively delivered to the downstream block promoting its quicker heating up and temperature uniformizing between 180°C and 230°C. Thus, not only the claim of temperature limitation, but also that of excess heat spreading are confirmed by the experimental results on the final prototype.

7.1.3 Electrical output and efficiency

For this analysis, and similarly to what happened in the first prototype, limitations related to the amount of input channels in the data acquisition system, led to the connection of the load resistances in series, therefore the measured voltage and power presented next as Row 1 refers to the four TEGs of that Row (two on the upper half and two on the bottom half). In Figure 102a it is possible to see the system total electrical power production which represents the sum of the electrical power output of all TEG modules.

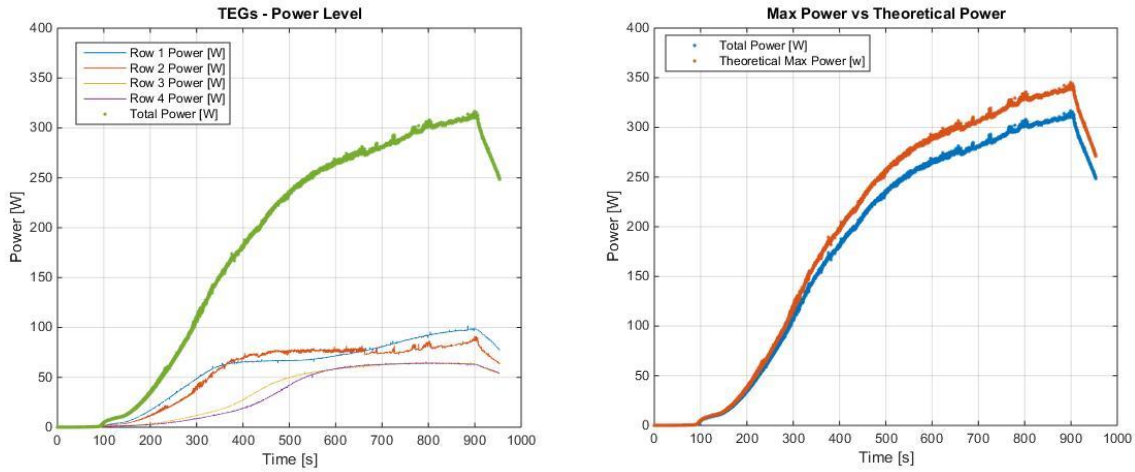

(a (b)

Figure 102 - (a) TEG Power Level by row and (b) Total Power vs Theoretical Max Power.

The maximum power achieved during this test was around 320W. The electrical efficiency expresses the ratio between the electric power generated and the thermal power absorbed by the system and by the TEG's. This parameter is as important as the electrical power output in limited thermal power applications, such as urban driving with a cold engine. The efficiency of the tested system is displayed on Figure 103.

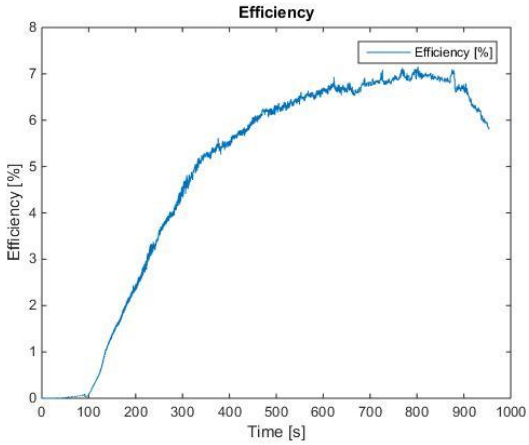

Figure 103 - TEG efficiency during the final Test Cycle.

During the test cycle the electrical efficiency increases as a result of the increase in the temperature differential between the TEG's faces. The maximum efficiency recorded was around 7%. This efficiency is higher than what could be expected from the *Hi-Z 14HV* TEGs. During the cycle under-study, the maximum operating temperature of the TEGs (~230 °C) was close to the maximum operating temperature of 250°C, where they are most efficient (~ 5%).

Actually, it has already been noted that the actual electric resistance of the modules supplied was lower than that advertised in the datasheet, so that is a first hint on why the actual performance of the modules might be better than advertised. This better-than-expected performance may also indicate that factors that normally reduce efficiency, such as cold side resistance and thermal contact resistances, have been minimized (densely finned water coolers, thermal grease was used), also indicate that the actual performance of TEGs may be better than the performance advertised by the manufacturer.

The carried-out analyses allowed to calculate some mean values for a given steady state of choice. For this test, an interval from 550 seconds to 600 seconds was chosen given to be moment when all the HPs in system were full and the Heat Exchanger was in full operation. Table 12 shows some of the calculated mean values.

Table 12 - Mean Values of Test in Full Operation (New Prototype)

Variable	Mean Value	Units
Exhaust Gas Temperature in	587	[°C]
Exhaust Gas Temperature out	232	[°C]
Cooling water Pressure drop	27.2	[mbar]
Exhaust mass flow rate	23.0	[g/s]
Fuel consumption	6.87	[l/h]
Power absorbed by exhaust heat exchanger	8.95	[kW]
Power produced by TEGs	265	[W]
Theoretical maximum power produced by TEGs	280	[W]

7.1.4 Power as a function of Temperature

As in the first test with the first prototype, under steady state operation, for the same temperature difference the TEGs should all produce the same power output. However, small differences appear depending on TEG position at the HX. These results were obtained under transient regime, so that thermal equilibrium has not yet been reached, and there are differences due to thermal inertia. This may mean that the temperature measured by the thermocouple is not always fully representative of the average temperature of the hot faces.

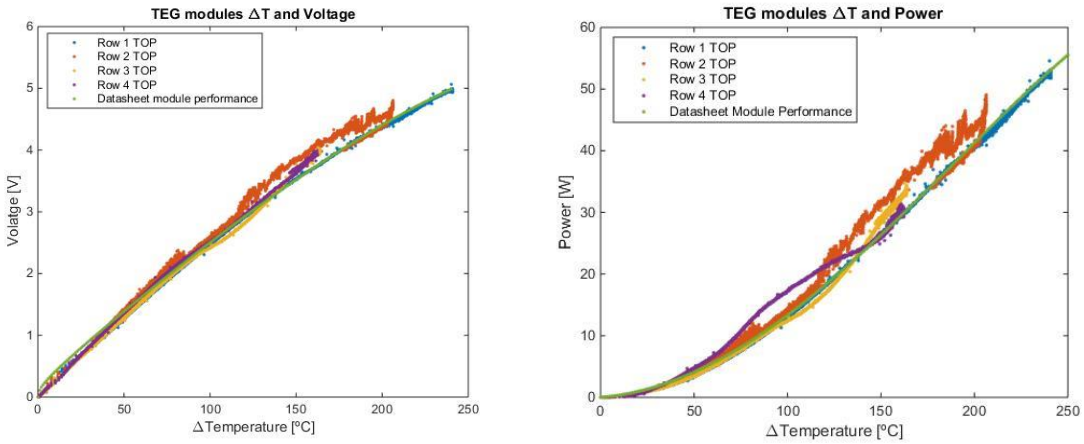

(a) (b)

Figure 104 - TEG (a) voltage and (b) power as a function of temperature differential.

Despite the undesirable noise, the graphics of Figure 104 present a comparison made between the TEG's performance in the experimental test cycle with the manufacture's performance datasheet. The same correction presented in Chapter 5.1.5 was made, where the value of the internal resistance of the module was brought close to the real one. In Figure 104a and Figure 104b the green line represents the performance of the TEGs based on the manufacturer datasheet. In conclusion, it can be stated that, on this experimental test, the performance of the modules is in accordance with what is announced by the manufacturer (after correction of the resistance).

7.2 Fuel and CO_2 Savings

Although the new prototype could not maintain pressure stability due to the expansion valve leakage problem, it was possible to test the system with a module hot face temperature close to 250°C (TEG module optimum/maximum allowed temperature). The same fuel savings and CO_2 emissions analyses presented in chapter 5.4 were made regarding the experimental results obtained with the new system. Table 13 presents the fuel and emissions savings for the case where the TCTG would be implemented for reducing the use of the alternator on the test cycle performed.

Table 13 - Vehicle and Alternator Fuel Power savings using new TCTG

Alternator and TEG chain of conversion	Value	Unit
Alternator Power	1.44	kW
Alternator Mechanical Power (η=55%)	2.62	kW
Alternator Fuel Power (η=18%)	14.5	kW
TEG Output	300	W
TEG Fuel Power (if produced by the Alternator)	3.03	kW
Parameter		
Vehicle Fuel Power	130.5	kW
Vehicle Total Fuel Power Consumption	29.0	g/s
Alternator Total Fuel Power Consumption	0.32	g/s
Alternator Fuel saving Using TEGs	0.067	g/s
Savings		
Alternator Fuel Power Savings using TEGs	**20.83%**	%
Vehicle Fuel Power Saving using TEGS	**2.3**	%

The new prototype can produce around 300 W (when fully operative) and replace the alternator in 20% of its load. It is noteworthy that this estimate is made considering alternator maximum load events. This is a significant increase when comparing with the previous prototype working at atmospheric pressure (only 4%). Although the value for the vehicle fuel power savings is small, the fact that the system is harvesting otherwise wasted energy and providing fuel power savings of 2.3% is breakthrough to this type of energy recover systems.

8. CONCLUSIONS AND FUTURE WORK

The present work dealt with the development, manufacture and full experimental validation of a novel Compact Temperature Controlled Thermoelectric Generator (TCTG) concept to recover the exhaust heat of engines. An original concept proposed by the team of the Engine Lab of the University of Minho (LaMoTA) had been previously proposed but had never been tested and the concept validated. This concept consists of a TCTG using high performance stainless steel corrugated pipes for the exhaust flow, which are embedded in a cast aluminium matrix, along with variable conductance heat pipes (VCHPs) that work as excess heat spreaders for temperature control under the variable thermal load found in real driving. When TEG modules temperature limit risks being exceeded at the hotter upstream regions of the HX, the VCHPs start absorbing heat by vaporization and spread the excess heat by condensation at the colder regions of the heat exchanger.

Firstly, an existing, limited pressure downsized prototype was instrumented and tested. Subsequently, an enhanced experimental downsized prototype was built and also tested.

Due to technical problems in the casting process of the aluminium matrix, the copper HPs of the existing prototype presented leaks, making it impossible to pressurize them above atmospheric pressure, thus the working fluid inside the HPs could only operate as excess heat spreader at 100°C, a temperature that is sub-optimal for the TEG generators. Nevertheless, this prototype could be used to validate the excess heat spreading and temperature control features claimed by the LAMoTA team in their patent submission and assessed numerically in previous publications. Therefore, the construction of the existing prototype was completed and it was instrumented. Namely, a water-cooling system was built including optimized finned cooling plates and pipelines as well as temperature, pressure and voltage data acquisition sensors that were incorporated into the prototype.

An experimental validation was carried out where the prototype was tested with a 1.6L petrol engine and the following results were obtained:

-TCTG heat exchanger effectiveness between 80-90% throughout the test cycle, indicating a good thermal design for the Heat Exchanger.

-The use of heat pipes proved to have a significant role in thermal control, allowing the system to operate at constant temperature even with excess heat, therefore avoiding thermal degradation of TEG modules under variable loads and providing a controlled thermal level to the TEGs. It was possible to observe the sequential (cascading) module activation during the heat spreading phase and the limitation in temperature.

-An average electrical power output of 60W was obtained when the HPs became fully activated, with a peak of 90W with fluid vaporization temperatures slightly over 100°C.

-The TEG´s recorded a maximum efficiency of 4%, which seems promising at this low temperature, as they are close to the manufacturer's maximum efficiency of 5% for a considerable higher temperature difference.

The engine exhaust data recorded in the experimental test was used as input for the existing numerical model. The results allowed to preliminarily validate the model of the concept:

- The prediction of the evolution of the total electric power produced was reasonably predicted, with the full HP operation occurring at 260s against the approximately 300 s recorded experimentally. The predictions of the power under full system operation were also relatively close to the value recorded experimentally (64W). Due to the lack of excess vapour condenser, the prototype continued to increase the output beyond the full system level.

After confirming the mathematical model validation, a simulation for the same driving cycle, this time with the vaporization temperature of 250°C was made, predicting that the system could achieve a maximum power output of 350W, which seems substantial, given that it is a downsized prototype (4 times smaller than future full-size prototypes).

-For the simulation of a fully sized prototype on a standard WTLC, using the working fluid vaporization temperature/modules maximum temperature of 250°C the system could produce more than 1.5kW. These figures seem to be highly promising for TEG systems in such small vehicles and are unparalleled in literature.

Also, a similar but more robust TCTG concept using stainless steel Heat Pipes instead of copper one's, aiming to overcome casting difficulties and therefore test the concept under saturation temperatures of 250°C and inner pressures in excess of 40 bar, was built and tested experimentally with a 1.6L petrol engine connected to a brake dynamometer. The following results were obtained:

- Minimum TCTG concept effectiveness between 55 and 65%, indicating a lower effectiveness than the previous prototype but at a much higher thermal load, still a convenient thermal design for the Heat Exchanger as it enabled the full operation of the VCHPs (maximum TEG power)

-The use of stainless-steel heat pipes proved to overcome the casting process difficulties and to have a significant role in thermal control while withstanding high pressure, allowing the system to operate at nearly constant temperature, therefore avoiding the thermal degradation of TEG modules under variable loads and spreading local excess heat instead of wasting this heat.

-Average electrical power output around 300W under the condition of HPs fully activated (optimal TEG temperature level, i.e., close to 250°C).
-The TEG´s maximum obtained efficiency of 7% suggests that the actual performance of TEGs might be better than the performance advertised by the manufacturer.

The prototype concept seems to validate previous thermal design optimization proposals done by the research group and provide a temperature controlled thermoelectric generator for vehicle application with no moving parts and little to no maintenance needs.
The experimental and numerical validation of the systems seems to indicate that it has a high potential for waste energy recovery applications on vehicles, because it seems able to maintain the TEG modules close to their optimal hot side temperature while avoiding overheating, **spreading excess heat instead of wasting it through by-pass systems,** and also avoiding thermal dilution in low heat load events because it is able to concentrate the limited amount of heat into fewer modules because the heat spreading only occurs when heat is excessive. In terms of thermal design, the use of corrugated pipes from Exhaust Gas Recirculation (EGR) cooler manufacturers and Heat Pipes to promote thermal control seems clearly an advantage, being the copper heat pipes problematic in terms of aluminium casting due to their thermal dilatation, and the stainless-steel ones more suitable to the manufacture process and to withstand system function in high pressure.
While being true that TEG modules still provide a low conversion efficiency from heat to electrical power at the present, typically below 5-7% for the temperature ranges of these applications, it is noteworthy that the studied concept allows a thermal optimization that will be even more valuable as higher figure of merit thermoelectric materials are steadily appearing in the market. Also, it is harvesting otherwise wasted energy that was not converted into useful work by the engine. Given its free availability and capability of conversion, it is only a question of evaluating its implementation viability in terms of economics, energy and environmental payback.

8.1 Future Work

In regards to the novel stainless steel HP prototype, future tests are required after valve repair to study in full the pressure evolution of the TCTG. Also, a wider engine speed range tests are required to fully study the excess condenser operation feature.

Regarding the *Exhaust2Energy* project, after the present validation of the thermal design and the mathematical model, the LaMoTA research group can confidently take the step of beginning the construction of a full-size prototype to experimentally validate the prediction of 1.5kW made by the mathematical model. Also, a full study of the HP behaviour under dynamic conditions, including adverse forces during breaking and accelerating, and a study of a by-pass valve implementation upstream of the HX is required. Note that this valve is designed to open once the thermoelectric generator achieves its full power (unlike competitive alternative designs) since under these conditions the heat exchanger cannot absorb more heat.

The system has still not been optimized in terms of mass, and form factor. This optimization could be done, along with the use of phase change fluids that could operate at lower pressures (i.e. DowTherm-A) to allow a lighter concept

VCHPs could be directly machined or formed into the body of the heat exchanger (as currently explored in project COOLSPOT), and laser textured surfaces used to improve phase-change

Suitable compact heat exchangers (i.e. wavy fins) combined with the use of these systems with heavy duty vehicles (as explored in a parallel dissertation) could also be further explored numerically and experimentally to make this concept further promising.

REFERENCES

[1] R. Muncrief and J. German, "Defeat devices under the U . S . and EU passenger vehicle emissions testing regulations," no. March, 2016.

[2] M. P. Tietge U, Sonsoles D, Zifei Y, "From laboratory to road international: A comparison of official and real-world fuel consumption and CO2 values for passenger cars in Europe, the United States, China, and Japan," *ICCT White Pap.*, no. November, p. 69, 2017, [Online]. Available: www.theicct.org.

[3] U. Tietge, P. Mock, V. Franco, and N. Zacharof, "From laboratory to road: Modeling the divergence between official and real-world fuel consumption and CO2 emission values in the German passenger car market for the years 2001–2014," *Energy Policy*, vol. 103, no. January, pp. 212–222, 2017, doi: 10.1016/j.enpol.2017.01.021.

[4] N. E. Ligterink and A. R. A. Eijk, "Update analysis of real-world fuel consumption of business passenger cars based on Travelcard Nederland fuelpass data," no. June, p. 25, 2014, doi: 10.13140/RG.2.1.3212.5040.

[5] D. F. Dominković, I. Bačeković, A. S. Pedersen, and G. Krajačić, "The future of transportation in sustainable energy systems: Opportunities and barriers in a clean energy transition," *Renew. Sustain. Energy Rev.*, vol. 82, no. June 2017, pp. 1823–1838, 2018, doi: 10.1016/j.rser.2017.06.117.

[6] "European Commission, 'Delivering the European Green Deal | Climate Action,'" 2021.

[7] European Commission, "Reducing CO2 emissions from heavy-duty vehicles | Climate Action," 2019. .

[8] W.-R. Chang, J.-J. Hwang, and W. Wu, "Environmental impact and sustainability study on biofuels for transportation applications," *Renew. Sustain. Energy Rev.*, vol. 67, pp. 277–288, Jan. 2017, doi: 10.1016/J.RSER.2016.09.020.

[9] A. Alagumalai, "Internal combustion engines: Progress and prospects," *Renew. Sustain. Energy Rev.*, vol. 38, pp. 561–571, Oct. 2014, doi: 10.1016/J.RSER.2014.06.014.

[10] W. Chen, J. Liang, Z. Yang, and G. Li, "A Review of Lithium-Ion Battery for Electric Vehicle Applications and Beyond," *Energy Procedia*, vol. 158, pp. 4363–4368, Feb. 2019, doi: 10.1016/J.EGYPRO.2019.01.783.

[11] P. Letmathe and M. Suares, "A consumer-oriented total cost of ownership model for different vehicle types in Germany," *Transp. Res. Part D Transp. Environ.*, vol. 57, pp. 314–335, 2017, doi: 10.1016/j.trd.2017.09.007.

[12] E. E. Agency, "Sharp decrease in CO2 emissions of new cars in 2020 — European Environment Agency," 2021. .

[13] T. Hoffman, "Alternative Fuels and Advanced Vehicle Technologies for Improved Environmental Performance: Towards Zero Carbon Transportation," *Woodhead Publ. Energy*, vol. 57, pp. 565–581, 2014.

[14] J. Martins and F. P. Brito, "Alternative fuels for internal combustion engines," *Energies*, vol. 13, p. 4086, Aug. 2020, doi: 10.3390/en13164086.

[15] F. P. Brito, J. Martins, F. Lopes, C. Castro, L. Martins, and A. L. N. Moreira, "Development and assessment of an over-expanded engine to be used as an efficiency-oriented range extender for electric vehicles," *Energies*, vol. 13, no. 2, 2020, doi: 10.3390/en13020430.

[16] F. Zhang, X. Hu, R. Langari, and D. Cao, "Energy management strategies of connected HEVs and PHEVs: Recent progress and outlook," *Prog. Energy Combust. Sci.*, vol. 73, pp. 235–256, Jul. 2019, doi: 10.1016/J.PECS.2019.04.002.

[17] J. Martins, *Motores de Combustão Interna*, 5ª Edição. Engebook, 2016.
[18] S. N. Hossain and S. Bari, "Waste heat recovery from the exhaust of a diesel generator using Rankine Cycle," *Energy Convers. Manag.*, vol. 75, pp. 141–151, Nov. 2013, doi: 10.1016/j.enconman.2013.06.009.
[19] C. RE and C. D, "Combined cycle for hybrid vehicles," *SAE*, 2015.
[20] E. Massaguer, A. Massaguer, T. Pujol, M. Comamala, L. Montoro, and J. R. Gonzalez, "Fuel economy analysis under a WLTP cycle on a mid-size vehicle equipped with a thermoelectric energy recovery system," *Energy*, vol. 179, pp. 306–314, 2019, doi: 10.1016/j.energy.2019.05.004.
[21] T. Wang, Y. Zhang, Z. Peng, and G. Shu, "A review of researchs on thermal exhaust heat recovery with Rankine cycle," *Renew. Sustain. Energy Rev*, vol. 15, 2011.
[22] Z. Peng, T. Wang, Y. He, and L. Lu, "Analysis of environmental and economic benefits of integrated Exhaust Energy Recovery (EER) for vehicles," *Appl. Energy*, pp. 238–243, 2013.
[23] T. Wang, Y. Zhang, J. Zhang, G. Shu, and Z. Peng, "Analysis of recoverable exhaust energy from a light-duty gasoline engine," *Appl. Therm. Eng.*, vol. 53, no. 2, pp. 414–419, 2013, doi: 10.1016/j.applthermaleng.2012.03.025.
[24] D. Rowe and C. Bhandari, *CRC Handbook of Thermoelectrics*. 1995.
[25] F. P. Brito *et al.*, "Analysis of thermoelectric generator incorporating n-magnesium silicide and p-tetrahedrite materials," *Energy Convers. Manag.*, vol. 236, p. 114003, May 2021, doi: 10.1016/J.ENCONMAN.2021.114003.
[26] L. M. Goncalves, J. Martins, J. Antunes, R. Rocha, and B. F., "Heat-Pipe Assisted Thermoelectric Generators for Exhaust Gas Applications," vol. 5, 2010.
[27] F. P. Brito, J. Martins, L. M. Goncalves, and R. Sousa, "Temperature controlled exhaust heat thermoelectric generation," *SAE Tech. Pap.*, no. January 2016, 2012, doi: 10.4271/2012-01-1214.
[28] F. P. Brito, J. Martins, L. M. Gonçalves, and R. Sousa, "Temperature Controlled Exhaust Heat Thermoelectric Generation," *SAE Int. J. Passeng. Cars - Electron. Electr. Syst*, vol. 5, pp. 561–571, 2017.
[29] and J. A. J. Martins, F. P. Brito, L. M. Goncalves, "Thermoelectric Exhaust Energy Recovery with Temperature Control through Heat Pipes," 2011.
[30] F. P. Brito, J. Martins, L. M. Goncalves, and R. Sousa, "Temperature controlled exhaust heat thermoelectric generation," *SAE Tech. Pap.*, 2012, doi: 10.4271/2012-01-1214.
[31] F. P. Brito, L. M. Goncalves, J. Martins, N. Antunes, and D. Sousa, "Influence of heat pipe operating temperature on exhaust heat thermoelectric generation," *SAE Int. J. Passeng. Cars - Mech. Syst.*, vol. 6, no. 2, 2013, doi: 10.4271/2013-01-0559.
[32] F. P. Brito, J. Martins, E. Hançer, N. Antunes, and L. M. Gonçalves, "Thermoelectric Exhaust Heat Recovery with Heat Pipe-Based Thermal Control," *J. Electron. Mater.*, vol. 44, no. 6, pp. 1984–1997, Jun. 2015, doi: 10.1007/s11664-015-3638-3.
[33] F. P. Brito *et al.*, "Analysis of the Effect of Module Thickness Reduction on Thermoelectric Generator Output," *J. Electron. Mater.*, vol. 45, no. 3, pp. 1711–1729, 2016, doi: 10.1007/s11664-015-4182-x.
[34] F. P. Brito *et al.*, "Analysis of a Temperature-Controlled Exhaust Thermoelectric Generator During a Driving Cycle," *J. Electron. Mater.*, vol. 45, no. 3, pp. 1846–1870, 2016, doi: 10.1007/s11664-015-4258-7.
[35] F. P. Brito *et al.*, "Efficiency improvement of vehicles using temperature controlled exhaust thermoelectric generators," *Energy Convers. Manag.*, vol. 203, no. November 2019, p. 112255, 2020, doi: 10.1016/j.enconman.2019.112255.
[36] N. Pacheco, F. Brito, R. Vieira, J. Martins, H. Barbosa, and L. M. Goncalves, "Compact automotive thermoelectric generator with embedded heat pipes for thermal control," *Energy*, vol. 197, p.

117154, Feb. 2020, doi: 10.1016/j.energy.2020.117154.
[37] and R. V. F. P. Brito, J. Martins, L. M. Goncalves, J. Teixeira, N. Pacheco, "System for efficient heat recovery and method thereof," 2018.
[38] N. Pacheco, F. P. Brito, R. Vieira, J. Martins, H. Barbosa, and L. M. Goncalves, "Compact automotive thermoelectric generator with embedded heat pipes for thermal control," *Energy*, vol. 197, 2020, doi: 10.1016/j.energy.2020.117154.
[39] N. Pacheco, F. P. Brito, R. Vieira, J. Martins, H. Barbosa, and L. M. Goncalves, "Compact automotive thermoelectric generator with embedded heat pipes for thermal control," *Energy*, vol. 197, p. 117154, 2020, doi: 10.1016/j.energy.2020.117154.
[40] F. P. Brito, J. Martins, L. M. Goncalves, J. Teixeira, N. Pacheco, and R. Vieira, "System for efficient heat recovery and method thereof," US Patent application, Attorney Docket number 10224/008071/US0, submitted August 8th 2019, originally filed in Portugal in August 8th. 2018 (application number 111106), 2019.
[41] a Thesis, "Modeling of an Automotive Exhaust," no. June, 2005.
[42] H. Julian Goldsmid, *Introduction to Thermoelectricicty*. 2010.
[43] "Figura Seebeck," 2008. https://searchnetworking.techtarget.com/definition/Seebeck-effect.
[44] R. M. Sousa, "Gerador Termoelétrico para Escape do Automóvel com Controlo de Temperatura," 2011.
[45] D. Ji *et al.*, "Thermoelectric generation for waste heat recovery: Application of a system level design optimization approach via Taguchi method," *Energy Convers. Manag.*, vol. 172, no. April, pp. 507–516, 2018, doi: 10.1016/j.enconman.2018.06.016.
[46] S. Siouane, S. Jovanovic, and P. Poure, "A Novel Identification Method of Thermal Resistances of Thermoelectric Modules Combining Electrical Characterization Under Constant Temperature and Heat Flow Conditions," *Trans. Environ. Electr. Eng.*, vol. 1, no. 4, p. 44, 2016, doi: 10.22149/teee.v1i4.72.
[47] T. M. Tritt, X. Tang, Q. Zhang, and W. Xie, "Solar thermoelectrics: Direct solar thermal energy conversion," *Fundam. Mater. Energy Environ. Sustain.*, vol. 33, no. January, pp. 289–294, 2011, doi: 10.1017/CBO9780511718786.026.
[48] S. S. Siouane, S. Jovanovic, and P. Poure, *Influence of contact thermal resistances on the Open Circuit Voltage MPPT method for Thermoelectric Generators*. 2016.
[49] R. Bjørk, "The Universal Influence of Contact Resistance on the Efficiency of a Thermoelectric Generator," *J. Electron. Mater.*, vol. 44, no. 8, pp. 2869–2876, 2015, doi: 10.1007/s11664-015-3731-7.
[50] T. P. Hogan *et al.*, "Nanostructured thermoelectric materials and high-efficiency power-generation modules," *J. Electron. Mater.*, vol. 36, no. 7, pp. 704–710, 2007, doi: 10.1007/s11664-007-0174-9.
[51] A. Polozine, S. Sirotinskaya, and L. Schaeffer, "History of development of thermoelectric materials for electric power generation and criteria of their quality," *Mater. Res.*, vol. 17, no. 5, pp. 1260–1267, 2014, doi: 10.1590/1516-1439.272214.
[52] J. Yang *et al.*, "On the tuning of electrical and thermal transport in thermoelectrics: An integrated theory-experiment perspective," *npj Comput. Mater.*, vol. 2, no. October 2015, 2016, doi: 10.1038/npjcompumats.2015.15.
[53] Y. A. Çengel, J. M. Cimbala, and R. H. Turner, *Fundamentals of fluid-thermal sciences*, vol. 2, no. 27. 2017.
[54] W. K. J. and R. D. E., *Termodinámica*, 6th ed. Madrid: McGraw-Hill, 2001.
[55] C. (Claus) Borgnakke and R. E. Sonntag, "Fundamentos da termodinámica," 2018.
[56] J. Lizarraga and A. Perez, *Exergy Analysis and Thermoeconomics of Buildings*. 2020.
[57] M. S. Veto and P. R. Christensen, "Mathematical Theory of Thermal Inertia Revisited 1: Improving

Our Understanding of Martian Thermophysical Properties Through Analogous Examples of Periodic Diffusive Inertias," *46th Lunar Planet. Sci. Conf.*, vol. 24, pp. 1–2, 2015, [Online]. Available: http://www.hou.usra.edu/meetings/lpsc2015/pdf/2914.pdf.

[58] G. Y. Eastman, "The Heat Pipe," vol. 218, no. 5, pp. 38–46, 1968.

[59] A. Faghri, *Heat Pipe Science and Technology*, Second. Global Digital Press, 2016.

[60] A. Faghri, "Review and Advances in Heat Pipe Science and Technology," *J. Heat Transfer*, vol. 134, no. 12, Oct. 2012, doi: 10.1115/1.4007407.

[61] A. Faghri, "Heat Pipes: Review, Opportunities and Challenges," *Front. Heat Pipes*, vol. 5, no. 1, 2014, doi: 10.5098/fhp.5.1.

[62] H. Shabgard, M. J. Allen, N. Sharifi, S. P. Benn, A. Faghri, and T. L. Bergman, "Heat pipe heat exchangers and heat sinks: Opportunities, challenges, applications, analysis, and state of the art," *Int. J. Heat Mass Transf.*, vol. 89, pp. 138–158, Oct. 2015, doi: 10.1016/J.IJHEATMASSTRANSFER.2015.05.020.

[63] C. Tarau, W. G. Anderson, and C. J. Peters, "Thermal management system for long-lived venus landers," *9th Annu. Int. Energy Convers. Eng. Conf. IECEC 2011*, no. July, 2011, doi: 10.2514/6.2011-5643.

[64] R. R. H. and R. W. U, "Thermoelectricity: Science and Engineering," *Intersci. Publ.*, 1961.

[65] I. B. C. and E. Miller, "Thermoelectric Materials and Devices," *Mater. Technol. Ser. Reinhold Publ. Coop.*, 1960.

[66] P. H. Egli, "Thermoelectricity," *John Wiley Sons*, 1960.

[67] N. Jr., "Portable thermoelectric generators," *Soc. Automot. Eng. New York, SAE-645A*, 1963.

[68] U. S. and K. V. Birkholz, U., Grob, "Conversion of Waste Exhaust Heat in Automobile using FeSi2 Thermoelements," *Int. Conf. Thermoelectr. Energy Conversion.*, 1988.

[69] R. J. C. and N. B. E. Bass, J.C., "Thermoelectric Generator for Diesel Trucks," 1991.

[70] I. J. C. Bass, N. B. Elsner and F. A. Leavitt Hi-Z Technology, "Performance of the 1 kW Thermoelectric Generator for Diesel Engines* J. C. Bass, N. B. Elsner and F. A. Leavitt Hi-Z Technology, Inc.," 1994.

[71] J. Fairbanks, "Thermoelectric Applications in Vehicles Status 2008," *6th Eur. Conf. Thermoelectr.*, pp. 1–7, 2008.

[72] J. C. Bass, "Design and Test of Prototype 1kW Generator for Diesel Engines," 1997.

[73] John C. Bass, K. A. S., and N. B. Elsner, "Thermoelectric Generator (TEG) for Heavy Diesel Trucks," 1995.

[74] J. C. Bass, D. Krommenhoek J., A. S. Kushch, and S. Ghamaty, "Development of an Underarmor 10-kW Thermoelectric Generator Waste Heat Recovery System for Military Vehicles," 2004.

[75] K. Ikoma, M. Munekiyo, K. Furuya, M. Kobayashi, T. Izumi, and K. Shinohara, "Thermoelectric module and generator for gasoline engine vehicles," in *Seventeenth International Conference on Thermoelectrics. Proceedings ICT98 (Cat. No.98TH8365)*, 1998, pp. 464–467, doi: 10.1109/ICT.1998.740419.

[76] K. Ikoma, M. Munekiyo, K. Furuya, M. Kobayashi, H. Komatsu, and K. Shinohara, "Thermoelectric generator for gasoline engine vehicles using Bi2Te3 modules," *Nippon Kinzoku Gakkaishi/Journal Japan Inst. Met.*, vol. 63, no. 11, pp. 1475–1478, 1999, doi: 10.2320/jinstmet1952.63.11_1475.

[77] S. S. Mohamed, "Design an Exhaut Thermoeletric Generator (ETEG) for Heavy Duty Hybrid Trucks," 2014.

[78] A. Kushch, M. Karri, B. Helenbrook, and C. Rickter, "The Effects of an Exhaust Thermoelectric Generator of a GM Sierra Pickup Truck," *DEER Conf.*, 2004, [Online]. Available: http://www1.eere.energy.gov/vehiclesandfuels/pdfs/deer_2004/session4/2004_deer_kushch.pdf.

[79] E. F. Thacher, B. T. Helenbrook, M. A. Karri, and C. J. Richter, "Testing of an automobile exhaust thermoelectric generator in a light truck," *Proc. Inst. Mech. Eng. Part D J. Automob. Eng.*, vol. 221, no. 1, pp. 95–107, 2007, doi: 10.1243/09544070JAUTO51.
[80] J. Lagrandeur and D. T. Crane, "Vehicle Fuel Economy Improvement through Thermoelectric Waste Heat Recovery," *North*, 2005.
[81] J. Dourado Oliveira, "Development of a Thermoelectric Generator for the Exhaust of a Vehicle," 2015.
[82] "GMZ Energy Announces 1,000 Watt High-Temperature Thermoelectric Generator for U.S. Military," 2014. https://www.businesswire.com/news/home/20141203005186/en/GMZ-Energy-Announces-1000-Watt-High-Temperature-Thermoelectric-Generator-for-U.S.-Military (accessed Aug. 30, 2021).
[83] "Evident Thermoelectrics acquires GMZ Energy," 2015. https://www.greencarcongress.com/2015/05/20150519-evident.html (accessed Aug. 30, 2021).
[84] T. Hogan *et al.*, "Nanostructured Thermoelectric Materials and High-Efficiency Power-Generation Modules," *J. Electron. Mater.*, vol. 36, pp. 704–710, Jan. 2007, doi: 10.1007/s11664-007-0174-9.
[85] F. Andrade, A. S. Moita, A. Nikulin, A. L. N. Moreira, and H. Santos, "Experimental investigation on heat transfer and pressure drop of internal flow in corrugated tubes," *Int. J. Heat Mass Transf.*, vol. 140, pp. 940–955, 2019, doi: 10.1016/j.ijheatmasstransfer.2019.06.025.
[86] J. Martins, L. M. L. M. Goncalves, J. Antunes, F. P. F. P. F. P. Brito, L. M. L. M. Goncalves, and J. Antunes, "Thermoelectric Exhaust Energy Recovery with Temperature Control through Heat Pipes," in *SAE 2011 World Congress and Exhibition*, 2011, pp. 1–23, doi: 10.4271/2011-01-0315.
[87] "HI-Z 14HV TEG module datasheet." https://hi-z.com/wp-content/uploads/2017/05/Data-Sheet-HZ-14.pdf.
[88] "Thermocouple base materials acc to IEC 584." THERMO ELECTRIC, Netherlands, p. 1.
[89] L. A. S. B. Martins, B. J. O. Araujo, J. J. G. Martins, and F. C. P. Brito, "Methodology for the energy characterization of type-approval and realworld driving cycles for passenger vehicles," *ASME Int. Mech. Eng. Congr. Expo. Proc.*, vol. 6A-2015, no. November, 2015, doi: 10.1115/IMECE2015-53669.
[90] M. Bradfield, "Improving Alternator Efficiency Measurably Reduces Fuel Costs," 2008.
[91] S. S. Torres, "Organização da produção no fabrico e corte de tubo," 2018.
[92] Sérgio Paulo Ferreira Marques, "Desenvolvimento de Bancadas para Testes de Motores e Veículos," 2014.
[93] Sigma Aldrich, "Materials for Advanced Thermoelectrics." https://www.sigmaaldrich.com/PT/en/technical-documents/technical-article/materials-science-and-engineering/microelectronics-and-nanoelectronics/thermoelectrics.
[94] N. B. Elsner, J. C. Bass, S. Ghamaty, D. Krommenhoek, and A. Kushch, "Program Diesel Truck Thermoelectric Generator," 2005.
[95] J. Fairbanks, "Vehicular Applications of Thermoelectrics," 2008.
[96] J. LaGrandeur, "Automotive Waste Heat Conversion to Electric Power using Skutterudites, TAGS, PbTe and Bi 2 Te 3 Discussion Outline Discussion Outline Background program information and system architecture System modeling (bumper to bumper vehicle model inclusive of ther," pp. 1–27, 2006.

APPENDICES

Appendix 1 – Hi-Z 14HV TEG Modules Datasheet

Appendix 2 – Security Valve Datasheet

Appendix 3 – Scientific contribution

Hi-Z TECHNOLOGY, INC.
Thermoelectric
Materials • Devices • Systems

14 watt module High Voltage Data Sheet

FEATURES

- **Produce more than 14 watts of power** (Th=250°C, Tc=50°C)
- **Intermittent Operation beyond 350°C**
- **Intermittent Power up to 25 watts**
- **Rugged Construction** (no ceramic, no solders, fiber reinforced construction makes module tolerant to abuse)
- **Long life** (> 10 years when properly used)
- **126 couples** $(Bi,Sb)_2(Te,Se)_3$
- **Produce 10mW @ ΔT=5°C**
- **Notches for easy alignment**

DESCRIPTION

This module is designed specifically for the generation of power and is able to tolerant intermittent temperatures exceeding 350°C but for maximum life expectancy it should not exceed 250°C. These high temperature properties are made possible by the bonded metal conductors that eliminate the presence of all solders.

While the module is optimized for waste heat recovery its reversible properties make it suitable as a thermoelectric cooler, especially for high temperature applications where sensitive electronic equipment must be cooled to below the ambient temperatures.

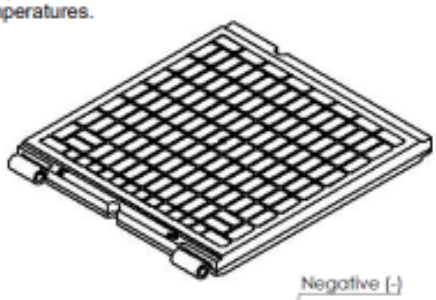

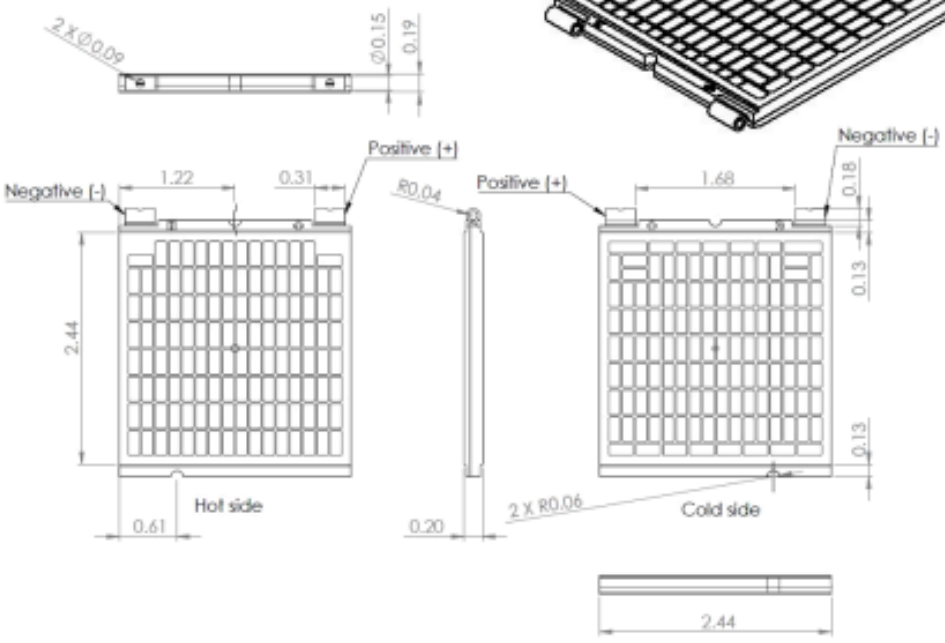

Suite 7400, 7606 Miramar Road, San Diego, CA 92126, Tel 858.695.6660, info@hi-z.com, www.hi-z.com

14 watt module
Data Sheet

Thermal and Electrical Characteristics					
Parameter	**Conditions**	**min**	**typ**	**max**	**units**
Power	Th=250°C, Tc=50°C @matched load	14.0	15.5	17.0	Watts
Open Circuit Voltage	Th=250°C, Tc=50°C	7.6	8.0	8.4	Volts
Matched load Voltage	Th=250°C, Tc=50°C	3.8	4.0	4.2	Volts
Internal Resistance	Th=250°C, Tc=50°C	0.9	1.0	1.1	Ω
	T = 25°C	0.55	0.6	0.65	Ω
Current	Th=250°C, Tc=50°C @matched load	3.8	4.0	4.2	Amps
	Th=250°C, Tc=50°C @short circuit	7.6	8.0	8.4	Amps
Heat Flux	Th=250°C, Tc=50°C @matched load	410	430	450	Watts
	Th=250°C, Tc=50°C open circuit	200	210	220	Watts
Heat Flux Density	Th=250°C, Tc=50°C @matched load	12	13	14	W/cm^2
Mass		64	65	66	grams

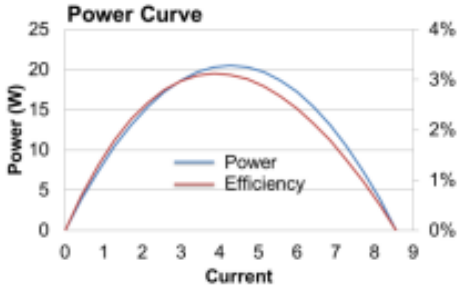

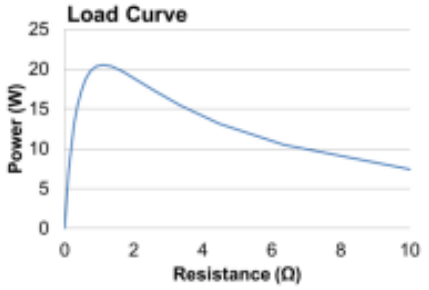

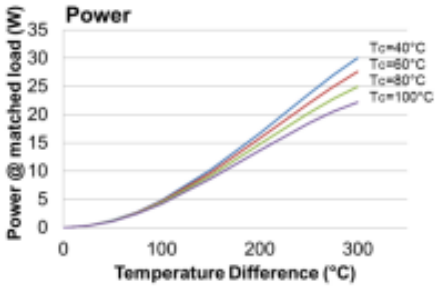

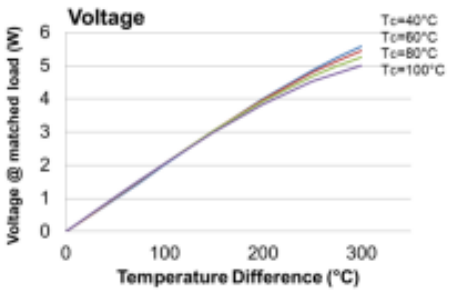

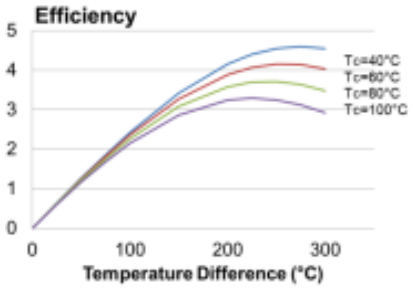

Stated temperatures are assumed to be on the module surface and not the heat exchangers.

Module surfaces are conductive and require the use of an insulator when used against metal heat exchangers. Ceramic wafers with thermal grease provide optimum performance.

Recommended mounting pressure is 100 to 200 psi uniformly distributed over the module surface.

Suite 7400, 7606 Miramar Road, San Diego, CA 92126, Tel 858.695.6660, info@hi-z.com, www.hi-z.com

APPENDIX 2 – SECURITY VALVE DATASHEET

ARMATUREN

ARI-SAFE-TCP 961 / 962 / 963
Technical data

ARI-SAFE-TCP - Standard safety valve D/G/F

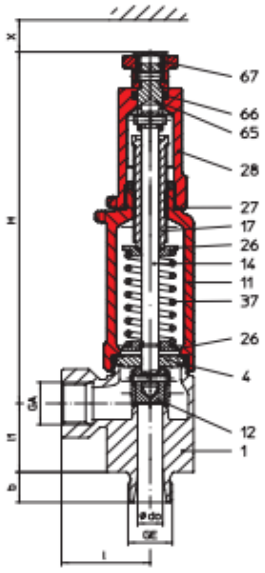

Fig. ... .961
closed lifting device

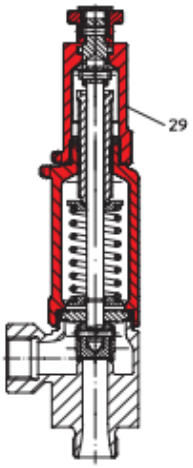

Fig. ... .962
open lifting device

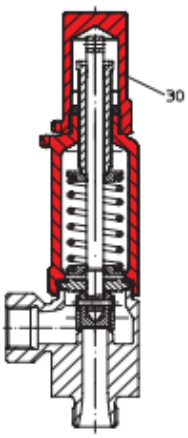

Fig. ... .963
gastight cap

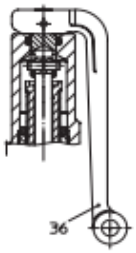

Fig. ... .961 / Fig. ... .962
optional with lever

Figure	Nominal pressure	Material	Nominal diameter	Temperature range	Thread
67.961 / 962 / 963	PN100	1.4581/EN-JS1049	DN15 - 25	-10°C to +300°C (up to +400°C on request)	DIN ISO 228 Part 1
57.961 / 963	PN100	1.4581	DN15 - 25	-60°C to +300°C (up to +400°C on request)	DIN ISO 228 Part 1

Construction		
Safety valve, spring loaded, direct loaded		
Requirement		
Acc. to EN ISO 4126-1, VdTÜV-leaflet 100, AD2000-A2		
Type-test approval		
Standard safety valve:	Fig. 961/962/963	TÜV · SV · . . -1041 · D/G
Standard safety valve:	Fig. 961/963	TÜV · SV · . . -1041 · F

Sizing	
for steam, air and water refer to capacity tables, calculations acc. to EN ISO 4126-1, TRD 421 and AD2000-A2	
Details required	
Medium gasform:	Mass flow (kg/h), molar mass (kg/kmol), Isotropic exponent, temperature (°C), set pressure (barg), back pressure (barg)
Medium liquid:	Mass flow (kg/h), density (kg/m³), viscosity, temperature (°C), set pressure (barg), back pressure (barg)
Order data:	
ARI-SAFE-TCP - Safety valve, Figure ....., DN ... / ..., PN .. / .., Material ....., Set pressure .... bar	

	standard: without metal bellow
Superimposed back pressure	no backpressure allowed
Built up back pressure	max. 10% from set pressure (higher on request)

Capacity saturated steam / Air / Water (incl. 10% overpressure)

DN			15	20	25	15	20	25	15	20	25
Connections		(inch)	G1/2 x 1/2	G3/4 x 1/2	G1 x 1	G1/2 x 1/2	G3/4 x 1/2	G1 x 1	G1/2 x 1/2	G3/4 x 1/2	G1 x 1
		(inch)	G1/2 x 3/4	G3/4 x 3/4		G1/2 x 3/4	G3/4 x 3/4		G1/2 x 3/4	G3/4 x 3/4	
		(inch)		G3/4 x 1			G3/4 x 1			G3/4 x 1	
do		(mm)	12			12			12		
Set pressure			Saturated steam (kg/h)			Air 0°C and 1.013 bara (Nm^3/h)			Water 20°C (t/h)		
↓ max. set pressure stainless steel version	0,2	(barg)	14	14	14	16	16	16	0,62	0,62	0,62
	0,5	(barg)	24	24	24	29	29	29	0,98	0,98	0,98
	1	(barg)	35	35	35	44	44	44	1,39	1,39	1,39
	2	(barg)	56	56	56	71	71	71	1,97	1,97	1,97
	3	(barg)	75	75	75	96	96	96	2,41	2,41	2,41
	4	(barg)	96	96	96	125	125	125	2,78	2,78	2,78
	5	(barg)	116	116	116	150	150	150	3,11	3,11	3,11
	6	(barg)	135	135	135	176	176	176	3,41	3,41	3,41
	7	(barg)	153	153	153	201	201	201	3,68	3,68	3,68
	8	(barg)	172	172	172	227	227	227	3,93	3,93	3,93
	9	(barg)	191	191	191	252	252	252	4,17	4,17	4,17
	10	(barg)	210	210	210	277	277	277	4,40	4,40	4,40
	11	(barg)	229	229	229	303	303	303	4,61	4,61	4,61
	12	(barg)	248	248	248	328	328	328	4,82	4,82	4,82
	13	(barg)	267	267	267	354	354	354	5,01	5,01	5,01
	14	(barg)	286	286	286	379	379	379	5,20	5,20	5,20
	15	(barg)	304	304	304	405	405	405	5,39	5,39	5,39
	16	(barg)	323	323	323	430	430	430	5,56	5,56	5,56
	17	(barg)	342	342	342	455	455	455	5,73	5,73	5,73
	18	(barg)	361	361	361	481	481	481	5,90	5,90	5,90
	19	(barg)	380	380	380	506	506	506	6,06	6,06	6,06
	20	(barg)	399	399	399	532	532	532	6,22	6,22	6,22
	25	(barg)	494	494	494	659	659	659	6,95	6,95	6,95
	30	(barg)	590	590	590	786	786	786	7,62	7,62	7,62
	35	(barg)	686	686	686	913	913	913	8,23	8,23	8,23
	40	(barg)	784	784	784	1040	1040	1040	8,79	8,79	8,79
	45	(barg)	883	883	883	1165	1165	1165	9,33	9,33	9,33
	50	(barg)	983	983	983	1295	1295	1295	9,83	9,83	9,83
	55	(barg)	1085	1085	1085	1420	1420	1420	10,31	10,31	10,31
	60	(barg)	1185	1185	1185	1550	1550	1550	10,77	10,77	10,77
	65	(barg)	1290	1290	1290	1675	1675	1675	11,21	11,21	11,21
	70	(barg)	1400	1400	1400	1800	1800	1800	11,63	11,63	11,63
	75	(barg)	1500	1500	1500	1930	1930	1930	12,04	12,04	12,04
	80	(barg)				2055	2055	2055	12,44	12,44	12,44
	85	(barg)				2185	2185	2185	12,82	12,82	12,82
	90	(barg)				2310	2310	2310	13,19	13,19	13,19
	95	(barg)				2438	2438	2438	13,5	13,5	13,5
	100	(barg)				2565	2565	2565	13,76	13,76	13,76

APPENDIX 3 – SCIENTIFIC CONTRIBUTION

Journal Article

"Experimental Validation of a Temperature Control Strategy for Maximizing Automotive Thermoelectric Generator Output under Variable Operating Conditions ",

Energy Conversion and Management Journal - Submitted

Conference Article

"Experimental Validation of a Thermoelectric Generator with Temperature Control Output design to operate under Variable Operating Conditions ",

International Conference of Energy & Environment - Submitted

International Conference Presentation

"Experimental Validation of a Temperature-controlled Thermoelectric Generator Concept Developed for Recovering the Exhaust Heat of a Vehicle",

2021 Virtual Conference of Thermoelectrics, Book of Abstracts - 19 July 2021

ANNEX 1 – DYNAMOMETRIC BRAKE CALIBRATION CURVE

Type	Weight [Kg]	Total weight [kg]	Controller Torque [N/m]	Real Torque [N/m]
No Weight	0	0	20	
Just the Arm	2,55818	2,55818	22,2	19,68007874
Weight	1,6024	4,16058	30,1	32,00734194
Weight	3,7024	6,26058	39,8	48,16264194
Weight	7,0786	9,63678	55,8	74,13574854
Weight	10,062	12,62018	69,6	97,08704474
Weight	15,9141	18,47228	97,7	142,10725
Weight	19,2903	21,84848	113,1	168,0803566
Weight	19,98	22,53818	117,1	173,3862187
Weight	21,3903	23,94848	122,6	184,2356566
Weight	22,8903	25,44848	130	195,7751566
Weight	25,8401	28,39828	143,9	218,467968
Weight	29,2163	31,77448	159,6	244,4410746
MAX			166,8	

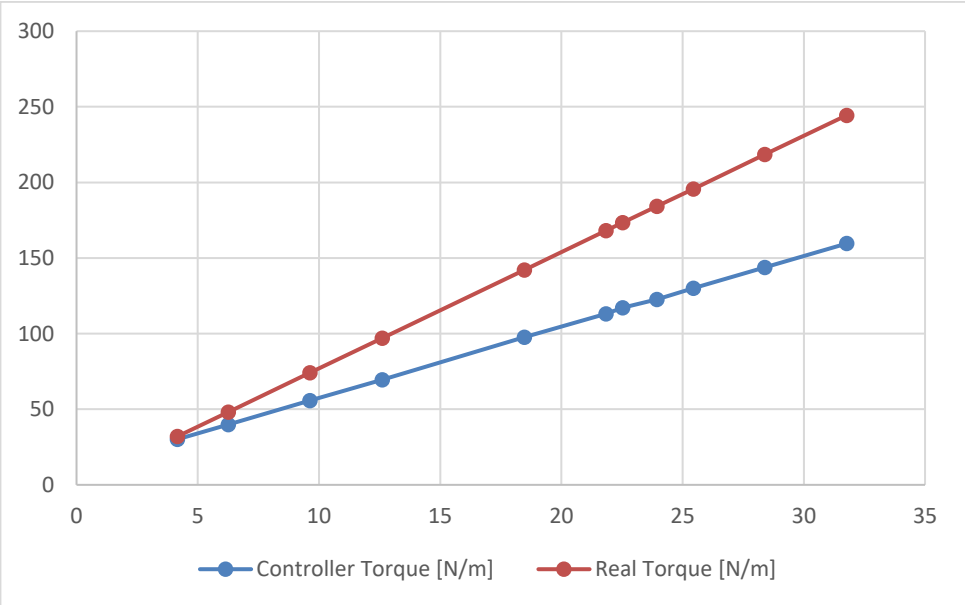

ANNEX 2 – FUEL AND CO2 EMISSION SAVINGS SPREADSHEET

Imput	Value	Units
Alternator´s Eficciency	0,55	
Volts	12	V
Amps	120	A
Engine's Efficiency	0,35	
Cp Petrol	45000000	J/kg
Exhaust gas mass flow	0,0029	Kg/s
TEGs Output	300	W

At 60 Km/h

Vehicle total fuel Power	130500	W
Potencia do Alternador [W]	1440	W
Mechanical Power do altternador [W]	2618,18182	W
Alternator Fuel Power consuption[W]	7480,51948	W
TEGs Fuel power if produced by alternator [W]	1558,44156	W
Vehicle Fuel Consuption	0,0029	Kg/s
Alternator Total Fuel Consuption	0,00016623	kg/s
Alternator Fuel Saving With TEGS [Kg/s]	6,6667E-06	kg/s
Alternator Fuel Saving With TEGS [l/h]	0,018	L/h
%Alternator Fuel Power savingsUsing TEGs	20,8333333	%
% Vehicle Fuel Power Savings using TEGs	1,19420809	%
Fuel Savings [L/100km]	0,03	L/100Km

Calculations:

i. $Vehicle\ total\ fuel\ Power = Cp\ Petrol \cdot Exhaust\ gas\ mass\ flow\ rate$

ii. $Alternator\ Power = U \cdot I$

iii. $Alternator\ Mechanical\ Power = Alternator\ Power \cdot Alternator´s\ Eficciency$

iv. $Alternator\ Fuel\ Power = Alternator\ Mechanical\ Power \cdot Engine\ Eficciency$

v. $TEGs\ Fuel\ power\ if\ produced\ by\ alternator\ [W] = TEGoutput/\ (Alernator\ efficiency \cdot Engine\ Eficciency)$

vi. $Vehicle\ total\ fuel\ Power = Cp\ Petrol \cdot Exhaust\ gas\ mass\ flow\ rate$

vii. $Vehicle\ Fuel\ Consuption = Vehicle\ total\ fuel\ Power/Cp\ Petrol$

viii. $Vehicle\ Fuel\ Consuption = Alternator\ Fuel\ Power\ consuption\ /\ Cp\ Petrol$

ix. $Alternator\ Fuel\ Saving\ With\ TEGS = Alternator\ Fuel\ Power\ consuption\ /\ Cp\ Petrol$

x. $Alternator\ Fuel\ Saving\ With\ TEGS = (TEGs\ Fuel\ power\ if\ produced\ by\ alternator/\ Fuel\ Power\ consuption) \cdot\ 100$

xi. $Alternator\ Fuel\ Saving\ With\ TEGS = (TEGs\ Fuel\ power\ if\ produced\ by\ alternator/\ Vehicle\ total\ fuel\ Power) \cdot\ 100$